

Washington University in St. Louis
Washington University Open Scholarship

Engineering and Applied Science Theses &
Dissertations

McKelvey School of Engineering

Winter 12-15-2017

System Characterizations and Optimized Reconstruction Methods for Novel X-ray Imaging

Huifeng Guan

Washington University in St. Louis

Follow this and additional works at: https://openscholarship.wustl.edu/eng_etds



Part of the [Biomedical Engineering and Bioengineering Commons](#), and the [Other Physics Commons](#)

Recommended Citation

Guan, Huifeng, "System Characterizations and Optimized Reconstruction Methods for Novel X-ray Imaging" (2017). *Engineering and Applied Science Theses & Dissertations*. 283.

https://openscholarship.wustl.edu/eng_etds/283

This Dissertation is brought to you for free and open access by the McKelvey School of Engineering at Washington University Open Scholarship. It has been accepted for inclusion in Engineering and Applied Science Theses & Dissertations by an authorized administrator of Washington University Open Scholarship. For more information, please contact digital@wumail.wustl.edu.

Washington University in St. Louis
School of Engineering and Applied Science
Department of Biomedical Engineering

Dissertation Examination Committee:
Mark Anastasio, Chair
Hua Li
Deshan Yang
Tiezhi Zhang
Quing Zhu

System Characterizations and Optimized Reconstruction Methods for Novel X-ray Imaging
Modalities

by
Huifeng Guan

A dissertation presented to
The Graduate School
of Washington University in
partial fulfillment of the
requirements for the degree
of Doctor of Philosophy

Dec 2017
Saint Louis, Missouri

copyright by
Huifeng Guan
2017

Contents

List of Tables	v
List of Figures	vi
Acknowledgments	x
Abstract	xii
1 Introduction	1
1.1 Background and Motivation	2
1.2 Overview of the Dissertation	6
2 Investigation of the boundary enhancement in propagation-based X-ray phase contrast tomosynthesis	8
2.1 INTRODUCTION	9
2.2 BACKGROUND	10
2.2.1 PB XPC imaging model	10
2.2.2 Data function	12
2.2.3 Interpretation of boundary-enhanced image	13
2.2.4 Fourier slice interpretation of tomographic depth resolution	14
2.3 MATERIALS and METHODS	15
2.3.1 Reconstruction algorithm	15
2.3.2 Simulation Studies	17
2.3.3 Experimental Studies	19
2.4 RESULTS	22
2.4.1 Simulation Studies	22
2.4.2 Experimental Studies	26
2.5 CONCLUSION AND DISCUSSION	28
3 A subspace-based resolution enhancing image reconstruction method for few-view differential phase-contrast tomography	31
3.1 Introduction	32
3.2 Background	35
3.2.1 D-XPCT imaging model in semi-discrete form	35
3.2.2 Null-space properties of finite-view Radon transform	37

3.3	Motivation for subspace-based image reconstruction	39
3.3.1	Revisiting the FBP algorithm	39
3.3.2	The recovery of the object's high-frequency contents	42
3.4	Subspace-based image reconstruction method	44
3.4.1	General forms of the discrete imaging model	44
3.4.2	Proposed iterative reconstruction method	45
3.5	Results	47
3.5.1	Computer-simulation studies	47
3.5.2	Experimental studies	53
3.6	Conclusion	58
4	A total-projection-length constrained method for stabilized quantitative projection-based dual-energy material decomposition	60
4.1	Introduction	61
4.2	Methods	64
4.2.1	Calibration method	64
4.2.2	Decomposition method	65
4.2.3	The total-projection-length constraint	67
4.3	Descriptions of numerical simulations	68
4.4	Simulation study results	70
4.4.1	The effect of total-projection-length constraint	70
4.4.2	The water-bath implementation of total-projection-length constraint	72
4.4.3	The scout-scan implementation of total-projection-length constraint	74
4.5	Conclusions and Discussions	77
5	Image reconstruction algorithms for tetrahedron beam computed tomography using CUDA-enabled GPUs	80
5.1	Introduction	81
5.1.1	Descriptions of TBCT imaging system	81
5.1.2	TBCT reconstruction algorithms	84
5.2	Background	87
5.2.1	Discrete imaging model for TBCT	87
5.2.2	PWLS-TV iterative image reconstruction	88
5.2.3	Ordered subsets acceleration strategy	90
5.2.4	Simultaneous algebraic reconstruction technique	92
5.3	GPU-accelerated TBCT reconstruction algorithms	96
5.3.1	Measurement geometry	96
5.3.2	Implementation of the FDK algorithm	97
5.3.3	Implementation of the forward / backprojection operator	103
5.3.4	Multi-GPU implementation of the reconstruction algorithms	116
5.4	Computer simulation studies	121
5.4.1	Numerical phantom and system geometries	121

5.4.2	Hardware specifications	122
5.4.3	Computational accuracy for full-view datasets	122
5.4.4	Computational accuracy for few-view datasets	126
5.4.5	Computational efficiency for GPU implementation	128
5.5	Experimental studies	132
5.6	Conclusion	135
6	Summary	137
Appendix A	The derivation of the high-frequency subspace	139
Appendix B	Conversion of linear attenuation coefficient to the combination of two basis materials	142
References	144
Vita	161

List of Tables

3.1	Quantitative evaluation of the reconstructed images in MSE and SSIM . . .	58
5.1	The flowchart of the standard FISTA-TV algorithm	89
5.2	The flowchart of the OS-SART-FISTA-TV algorithm	95
5.3	The flowchart of the FDK algorithm(on kernel)	102
5.4	The flowchart of the algorithm for ray-driven forward operator (on kernel) .	108
5.5	The flowchart of the algorithm for voxel-wise backprojection operator (on kernel)	111
5.6	The flowchart of the algorithm for pixel-wise backprojection operator (on kernel)	115

List of Figures

2.1	A schematic of the PB XPC imaging geometry is shown in which the object is fixed in a reference coordinate system (x, y, z) . The source (not shown) and detector rotate about the y -axis.	11
2.2	A parallel-beam projection along a direction θ in spatial domain corresponds to a plane acquired along θ in the frequency domain. This figure illustrates the reduced spatial resolution in the z -direction of reconstructed tomosynthesis images.	13
2.3	The phantom and the spectrum employed in the computer simulation. (a) A central slice through the numerical soft tissue phantom employed in the tomosynthesis simulations is shown in the left panel (viewed from above along the positive y -axis). The larger enclosing sphere is 4mm in diameter and is composed of healthy breast tissue. Diameters of internal spheres range from $80\mu m$ to $160\mu m$ and are composed of adipose tissue (grey) and calcium sulfate (white). (b) The right panel shows the polychromatic x-ray spectrum assumed in the tomosynthesis simulations. The y -axis gives the normalized weight for each energy bin.	17
2.4	The reconstructed horizontal slices (in-depth images) are shown for AB (a) and PB-XPC (b) tomosynthesis scans of the numerical phantom displayed in figure 2.3(a). The grayscale window represents attenuation coefficient (m^{-1}). Two vertical lines in the top panels are extracted, and the corresponding scaled profiles are shown and compared in the bottom panels: (c) for the profile at $x=210$, and (d) for the profile at $x=256$	21
2.5	An overhead view of the numerical phantom is shown to indicate two depth positions ($z=256$, $z=354$) where the corresponding in-plane images (x - y plane) are to be extracted for the investigation of depth position determination (see figure 2.6 and 2.7).	23
2.6	The comparisons of reconstructed in-plane images at depth position $z=256$ (<i>top row</i>) and associated profiles (<i>bottom row</i>) are shown here. (a) The line profiles from AB tomosynthesis result show similar signals from all internal spheres. (b) The PB-XPC tomosynthesis result reveals edge-enhancement for some of the internal spheres. (c) The true in-plane phantom structure shows that only the edge-enhanced spheres in (b) are actually located at that z -position of the reconstructed slice.	24

2.7	A comparison of reconstructed in-plane images at an off-center depth position $z=354$ (<i>top row</i>) and associated profiles (<i>bottom row</i>) is presented. The interpretation is similar to that in figure 2.6.	25
2.8	One typical projection image of an <i>ex-vivo</i> mouse lung sample acquired with different propagation distances. (a) $R_1=R_2=13\text{cm}$ for the AB tomosynthesis scan; (b) $R_1=R_2=74\text{cm}$ for the PB-XPC tomosynthesis scan. Due to the high phase-contrast sensitivity during acquisition, the PB-XPC projection presents more features of weakly absorbing microstructure than the AB projection.	28
2.9	A comparison of reconstructed in-plane images for an <i>ex-vivo</i> mouse lung is shown. The grayscale window represents attenuation coefficient (m^{-1}). The top and bottom rows correspond to in-plane slices located at $z=4.2\text{mm}$ and $z=4.3\text{mm}$, respectively, of the reconstructed 3D volume from AB tomosynthesis (a,d), PB-XPC tomosynthesis (b,e), and full-view CT (c,f) data sets. Two airways are seen in the tomosynthesis results and their line profiles are delineated as the arrows indicate. For each row, edge-enhancement in the PB-XPC reconstructions is able to provide a method to identify structures that are truly located at the particular z -position, which is verified by the corresponding CT result.	29
3.1	(a) The null-space functions of the finite-view Radon transform are contained exclusively outside a disk Ω in the Fourier domain, shown as the gray region. (b) If a to-be-imaged object has all the frequency contents confined to Ω without overlapping the null-space region, it means the object could be reliably reconstructed.	38
3.2	The illustration of the reconstruction over the support r and with a virtual mask W . FBP algorithm ensures that the reconstruction of ROI within r' is not affected by the masked region.	41
3.3	(a) The complete phantom. (b) A zoomed-in region of the phantom with adjusted gray-value window. The dashed circle indicates the designated ROI where the capability of reconstructing high-frequency structures is expected. (c) The extracted profile of the phantom across the center.	48
3.4	The comparison of reconstructed images inside the designated ROI. (a) Phantom; (b)-(e) The PLS-TV method with increasing TV regularization parameter values; (f) FBP method; (g)-(j) The proposed SuB-PLS-TV method with progressively increasing TV regularization parameter values.	50
3.5	The comparison of reconstructed images outside the designated ROI. (a) Phantom; (b)-(e) The PLS-TV reconstruction results with increasing TV regularization parameter values; (f) FBP method; (g)-(j) The proposed SuB-PLS-TV reconstruction results with progressively increasing TV regularization parameter values.	51

3.6	The profiles extracted from the conventional PLS-TV reconstructed images with increasing regularization parameter values (blue) and the corresponding ground truth (red).	52
3.7	The profiles extracted from the SuB-PLS-TV reconstructed images with increasing regularization parameter values (blue) and the corresponding ground truth (red).	52
3.8	(a) The reference image of the object produced by use of the FBP algorithm and the complete data. (b) A zoomed-in region of the designated ROI. . . .	54
3.9	The comparison of the reconstructed ROI ② by use of FBP, PLS-TV and SuB-PLS-TV methods.	54
3.10	The comparison of the reconstructed ROI ③ by use of FBP, PLS-TV and SuB-PLS-TV methods.	56
3.11	The comparison of the reconstructed ROI ④ by use of FBP, PLS-TV and SuB-PLS-TV methods.	56
3.12	The comparison of the reconstructed region ⑤ outside the designated ROI by use of FBP, PLS-TV and SuB-PLS-TV methods.	57
4.1	(a) The numerical breast phantom. (b) A schematic view of the arrangement of calibration phantoms. (c) The two spectra employed in the numerical studies.	69
4.2	The decomposition results obtained by use of the conventional method (1% noise)	70
4.3	The decomposition results obtained by use of total-projection-length constrained method (1% noise)	71
4.4	The decomposition results obtained by use of total-projection-length constrained method (10% noise)	72
4.5	The total-projection-length constrained decomposition results using “water-bath” method (1% noise)	74
4.6	(a) The 3D numerical breast phantom. (b) The acquisition geometry of the scout scan. (c) A typical simulated projection image.	75
4.7	(a) The central vertical slice of the reconstructed image from 30-view data set. (b) The total-projection-length along the X-ray beam direction extracted from the reconstructed image.	75
4.8	The total-projection-length constrained decomposition results using “scout-scan” method (5% noise)	76
5.1	Diagram of TBCT geometry.	82
5.2	Side view of TBCT.	82
5.3	(a) A possible configuration of dual-source, dual-detector TBCT system mounted on a regular LINAC gantry. (b) Dimensions of a commercial LINAC with kV-CBCT installed.	84
5.4	A schematic of the TBCT imaging geometry	96

5.5	The illustrations of backprojection processes for CBCT (left) and TBCT (right).	98
5.6	Reconstruction performance of the TBCT-FDK previously reported. (left) the central vertical plane of the phantom; (right) the corresponding reconstructed image; (right) the profile comparison along the central vertical line.	100
5.7	Reconstruction performance of the TBCT-FDK developed by the author. Each column corresponds to different weight strategy for handling “data redundancy” issue.	100
5.8	The schematics for (a)voxel-driven backprojection, (b) ray-driven (Siddon’s method) projection, (c) ray-driven (interpolation method) projection, (d) distance-driven forward/backprojection.	105
5.9	A 2D illustration of Siddon’s ray-tracing strategy in which intersections of the ray with lines are considered.	107
5.10	An illustration of the “shadow formation” which is used to determine the range of pixels for backprojection with respect to a given voxel.	110
5.11	A prediction can be made to exclude those sources not involved in the back-projections for a specific voxel.	112
5.12	An illustration of the pixel-wise implementation of the backprojection. A similar ray-tracing process is conducted to update all the voxels along the ray.	114
5.13	A schematic of 4-GPU implementation for OS-SART-FISTA-TV algorithm.	118
5.14	Four different TBCT system designs with $N_s = 1, 2, 8$ and 64 , respectively.	123
5.15	The central vertical slices of the reconstructed images for full-view dataset $N_v = 360$	124
5.16	The central vertical slices of the reconstructed images for few-view dataset $N_v = 360, 180, 90$ and 45	127
5.17	single-GPU FDK reconstruction times. $N = 512^3$; $M = 1024^2 \times 360$	129
5.18	single-GPU forward and backprojection times (per iteration)	130
5.19	Multi-GPU reconstruction times for iterative algorithm (per iteration). $N = 512^3$; $M = 1024^2 \times 360$	131
5.20	Multi-GPU reconstruction times for iterative algorithm (per iteration). $N = 256^3$; $M = 512^2 \times 360$	131
5.21	Relative error as a function of iteration numbers for OS-SART-FISTA-TV algorithm	132
5.22	A picture of the bench-top TBCT system.	133
5.23	A diagram of the bench-top TBCT system illustrating the geometry and electrical connection.	133
5.24	Reconstructed pig-head images for an experimental dataset.	134

Acknowledgments

Foremost, I would like to express my sincere gratitude to my advisor Prof. Mark A. Anastasio, for his advice, encouragement and mentorship throughout all these years. I am deeply impressed by his immense knowledge, insightful thoughts and high research standard from which I gained great benefits during my research experience. Dr. Anastasio is always enthusiastic, energetic and open to discussion with his students. It has been my great honor to work under his supervision, learning to be a serious imaging scientist, as well as the importance of an open and curious mind, a positive attitude, and great self-discipline in scientific endeavors.

Besides my advisor, I would like to thank all the other members of my thesis committee: Dr. Hua Li, Dr. Deshan Yang, Dr. Tiezhi Zhang and Dr. Quing Zhu, for their insightful comments and helpful discussions. Many thanks go to our collaborator Prof. Alessandro Olivo in UCL and his team who contributed a lot of nice experimental data sets.

I would also like to thank some former senior labmates who have graduated or completed their research roles in Anastasio's group, Dr. Qiaofeng Xu, Dr. Alfred Garson, Dr. Kun Wang and Dr. Chao Huang, who trained and guided me early in my research life. Their ingenuity and hard work have been a constant inspiration and encouragement to me. I have

also received generous help and enormous support from my current labmates, Thommas Matthews, Yang Lou, Yujia Chen, Joe Poudel, and Weimin Zhou. This dissertation would not have been possible without their supports.

Last but not the least, I owe special thanks to my family for their unconditional love, trust and encouragement, which have made this dissertation possible and the whole process rewarding.

Huifeng Guan

Washington University in Saint Louis

Dec 2017

ABSTRACT OF THE DISSERTATION

System Characterizations and Optimized Reconstruction Methods for Novel X-ray Imaging
Modalities

by

Huifeng Guan

Doctor of Philosophy in Biomedical Engineering

Washington University in St. Louis, Dec 2017

Research Advisor: Professor Mark A. Anastasio

In the past decade there have been many new emerging X-ray based imaging technologies developed for different diagnostic purposes or imaging tasks. However, there exist one or more specific problems that prevent them from being effectively or efficiently employed. In this dissertation, four different novel X-ray based imaging technologies are discussed, including propagation-based phase-contrast (PB-XPC) tomosynthesis, differential X-ray phase-contrast tomography (D-XPCT), projection-based dual-energy computed radiography (DECR), and tetrahedron beam computed tomography (TBCT). System characteristics are analyzed or optimized reconstruction methods are proposed for these imaging modalities. In the first part, we investigated the unique properties of propagation-based phase-contrast imaging technique when combined with the X-ray tomosynthesis. Fourier slice theorem implies that the high frequency components collected in the tomosynthesis data can be more reliably reconstructed. It is observed that the fringes or boundary enhancement introduced by the phase-contrast effects can serve as an accurate indicator of the

true depth position in the tomosynthesis in-plane image. In the second part, we derived a sub-space framework to reconstruct images from few-view D-XPCT data set. By introducing a proper mask, the high frequency contents of the image can be theoretically preserved in a certain region of interest. A two-step reconstruction strategy is developed to mitigate the risk of subtle structures being oversmoothed when the commonly used total-variation regularization is employed in the conventional iterative framework. In the third part, we proposed a practical method to improve the quantitative accuracy of the projection-based dual-energy material decomposition. It is demonstrated that applying a total-projection-length constraint along with the dual-energy measurements can achieve a stabilized numerical solution of the decomposition problem, thus overcoming the disadvantages of the conventional approach that was extremely sensitive to noise corruption. In the final part, we described the modified filtered backprojection and iterative image reconstruction algorithms specifically developed for TBCT. Special parallelization strategies are designed to facilitate the use of GPU computing, showing demonstrated capability of producing high quality reconstructed volumetric images with a super fast computational speed. For all the investigations mentioned above, both simulation and experimental studies have been conducted to demonstrate the feasibility and effectiveness of the proposed methodologies.

Chapter 1

Introduction

In the past decade there have been many new emerging X-ray based imaging technologies developed for different diagnostic purposes or imaging tasks. However, there exist one or more specific problems that prevent them from being effectively or efficiently employed. In this dissertation, four different novel X-ray based imaging technologies are discussed, including propagation-based phase-contrast (PB-XPC) tomosynthesis, differential X-ray phase-contrast tomography (D-XPCT), projection-based dual-energy computed radiography (DECR), and tetrahedron beam computed tomography (TBCT). System characteristics are analyzed or optimized reconstruction methods are proposed for these imaging modalities. The goal and purpose of this dissertation is to investigate the advantages of these technologies or to improve the current imaging performance by developing new methodologies or strategies, promoting wider uses of these technologies in clinical or biological applications. We will briefly review these imaging modalities and their specific problems in this chapter.

1.1 Background and Motivation

Although conventional absorption-based (AB) tomosynthesis techniques have been extensively studied and implemented for numerous imaging applications [114, 157, 61], only a small number of studies have explored migrating X-ray phase-contrast (XPC) techniques to tomosynthesis and its potential advantages. X-ray phase-contrast imaging (XPCI) has proved to hold promise for a variety of biomedical applications [106, 92, 195]. Propagation-based XPC (PB-XPC) imaging, also known as in-line XPC imaging, is the simplest form to implement on the benchtop. To date, relatively few publications have specifically focused on propagation-based X-ray phase-contrast tomosynthesis [190, 151]. While previous studies [66, 167] showed PB-XPC tomosynthesis is able to produce boundary-enhanced in-plane images that better reveal tissue interfaces than conventional AB tomosynthesis, there remains a lack of reported experiments and analyses that discuss the resolving abilities of PB-XPC tomosynthesis in the depth direction. In this dissertation we will present numerical and experimental investigations that compare the ability of AB and PB-XPC tomosynthesis to distinguish between in-plane and out-of-plane structures. The results reveal that, in PB-XPC tomosynthesis, the phase-contrast-induced fringes can help discriminate in-plane structures from out-of-plane structures, thus providing better depth-position characterization than AB tomosynthesis.

Besides the propagation-based XPC imaging, there are a few other implementations of XPCI techniques that are generally referred to as differential phase-contrast imaging (D-XPCI) methods. They typically yield estimates of the one-dimensional (1D) derivative of the projected real-valued component of the refractive index distribution of an object. In this work, a tomographic implementation of differential XPCI is considered, referred to as differential X-ray phase-contrast tomography (D-XPCT). The goal of D-XPCT is to produce an estimate

of the real-valued component of the refractive index distribution, which describes the spatially variant refractive properties of an object. When the data are acquired at a sufficiently large number of tomographic views [145], image reconstruction in D-XPCT can be readily accomplished by use of a modified filtered backprojection (FBP) algorithm [47, 69, 127]. However, in current implementations of D-XPCT, it may not be desirable to acquire data at a large number of tomographic view angles. This is because D-XPCT methods are currently limited by relatively long data-acquisition times and radiation exposures, which has hindered the widespread application of the method to *in vivo* applications. Since current implementations typically utilize a 'step-and-shoot' data-acquisition protocol, one way to mitigate this problem is to acquire tomographic measurements at a reduced number of view angles. The associated image reconstruction problem is generally referred to as a 'few-view' image reconstruction problem [140, 15]. Modern few-view image reconstruction methods are optimization-based and typically utilize an iterative method to find a finite-dimensional estimate of the object function that approximately minimizes an objective function subject to constraints. Because few-view image reconstruction corresponds to an ill-conditioned inverse problem, a regularized solution must be computed; however the design of an effective regularization strategy is influenced by many factors, including the characteristics of the refractive index distribution to be estimated. It remains challenging to design a regularization strategy that faithfully preserves fine object features in the reconstructed image when only few-view tomographic data are utilized. In this work, a new method for few-view image reconstruction in D-XPCT is proposed and investigated. A distinctive feature of the method is that the sought-after object function is decomposed into two components that reside in distinct subspaces. In this way, the higher-frequency components and lower-frequency components of the object function are separated and reconstructed respectively, recovering a resolution-enhanced region of interest (ROI) from few-view measurements.

Dual-energy computed radiography (DECR)[24, 121] is a planar imaging technique in which two (or two sets of) projections using two different incident beam spectra are acquired of the same object. X-ray attenuation for the range of energies employed in diagnostic radiography consists of contributions from photoelectric absorption and Compton scattering. The probabilities for the two types of interactions are relatively independent of energy and material composition. Two X-ray projections of an object, one acquired with a high energy beam and the other with a low energy beam, will have differences in detected intensities between the two radiographs which depend on the composition of the object. For an object composed of two materials, these intensity changes can be exploited to form two basis material images[5, 23]. This procedure is often referred to as material decomposition. The decomposed information can facilitate material segmentation or identification of an abnormality[131, 159]. Though projection-based decomposition is essentially free of the beam hardening problem[131], DECR seeks the solution of a highly nonlinear and ill-posed inverse problem which is quite sensitive to noise[11, 22]. This is because the exact dual-energy imaging model should incorporate a polychromatic X-ray source spectrum that introduces transcendental functions. This limitation has prevented its widespread implementation in medical imaging applications. To mitigate this problem, we propose to introduce a constraint of total projection length, which can effectively stabilize the conventional projection-based material decomposition. We also develop two feasible “water-bath” and “scout-scan” ideas that can be used to practically implement the desired constraint. Numerical studies show that our method is capable of accurate two-material decomposition and shows robustness against data noise.

Tetrahedron beam computed tomography (TBCT) is a novel volumetric imaging system with a modified geometrical design compared to the commonly used cone-beam computed tomography (CBCT)[178]. In TBCT, a linear array of sources are stacked vertically, forming

a series of quasi-fan beams directed towards a linear CT detector array that is positioned orthogonally to the source array. During the scan, the X-ray source sequentially operates along the z -direction and the corresponding projection images are continuously recorded at every angular position. While the gantry rotates around the object, the collected data can be used for volumetric image reconstruction. TBCT holds great promise of mitigating scatters. The source collimator is adjusted to make sure that all fan beams are well aligned with the the central row of the detector, so most scattered photons are deflected out of the fan beam paths and therefore go undetected. TBCT also features flexible geometrical settings and can be further modified to incorporate dual-source arrays and dual-detector arrays to increase FOV and to facilitate imaging guided radiation therapy (IGRT)[83]. Though a few preliminary image reconstruction results came along with the invention of TBCT, however, a careful investigation of the reconstruction algorithms specific to the TBCT geometries has not been found. In this dissertation, we derived a reliable analytical reconstruction method from the conventional FDK algorithm by introducing a proper weighting function in the TBCT image domain. An advanced optimization-based iterative algorithm is also developed that features fast convergence rate and robustness against data noise and data incompleteness. In order to efficiently exploit the parallelism in GPU computing, the reconstruction algorithms were further optimized with special computational strategies. The reconstructed results from numerical and experimental data sets have demonstrated the good performances of the proposed reconstruction algorithms in terms of both the image quality and computational efficiency.

1.2 Overview of the Dissertation

In the following chapters, the dissertation will discuss four topics regarding the system characterization or optimized reconstruction methods for the novel X-ray imaging modalities that have been introduced above.

Chapter 2 investigates the unique properties of propagation-based phase-contrast imaging technique when combined with the X-ray tomosynthesis. The Fourier slice theorem implies that the high frequency components collected in the tomosynthesis data can be more reliably reconstructed. It is revealed that the fringes or boundary enhancement introduced by the phase-contrast effects can behave as an accurate indicator of the true depth position in the tomosynthesis in-plane image.

Chapter 3 derives a sub-space framework to reconstruct images from a few-view differential phase-contrast tomography (DPCT) data set. By introducing a proper mask and designing a novel two-step reconstruction strategy, the high frequency information of the image can be largely preserved in a certain region of interest. It mitigates the concerns that subtle structures might be oversmoothed when the commonly used total-variation regularization is incorporated in the conventional iterative framework.

Chapter 4 proposes a practical method to improve the quantitative accuracy of the projection-based dual-energy material decomposition. It is discovered in this work that applying a total-projection-length constraint along with the dual-energy measurements can achieve a stabilized numerical solution of the decomposition problem, thus overcoming the disadvantages of the conventional approach that was extremely sensitive to noise corruption.

Chapter 5 describes the modified filtered backprojection and iterative image reconstruction algorithms specifically developed for tetrahedron beam computed tomography (TBCT). Special parallelization strategies are designed to facilitate the use of GPU computing, showing demonstrated capability of producing high quality reconstructed volumetric images with a super fast computational speed.

A summary of the dissertation and closing remarks are presented in Chapter 6.

Chapter 2

Investigation of the boundary enhancement in propagation-based X-ray phase contrast tomosynthesis

Propagation-based X-ray phase-contrast (PB XPC) tomosynthesis combines the concepts of tomosynthesis and XPC imaging to realize the advantages of both for biological imaging applications. Tomosynthesis permits reductions in acquisition times compared with full-view tomography, while XPC imaging provides the opportunity to resolve weakly absorbing structures. In this Note, an investigation of the depth resolving properties of PB XPC tomography is conducted. The results demonstrate that in-plane structures display strong boundary-enhancement while out-of-plane structures do not. This effect can facilitate the identification of in-plane structures in PB XPC tomography that could normally not be distinguished from out-of-plane structures in absorption-based tomography.

2.1 INTRODUCTION

X-ray phase-contrast (XPC) imaging holds promise for a variety of biomedical applications [106, 92, 195]. There exist several implementations of XPC imaging that include crystal-based diffraction enhanced imaging approach [38], grating-based method that uses a Talbot interferometry [163] and a more recently developed coded aperture variety [120]. Propagation-based XPC (PB XPC) imaging, also known as in-line XPC imaging, is the simplest form to implement on the benchtop. It requires only a microfocus X-ray source, a high resolution detector, and an appropriately defined imaging geometry [166, 170, 62]. In practice, these requirements lead to longer imaging times than typically encountered in conventional absorption-based (AB) radiography. This can be problematic in tomographic implementations of PB XPC imaging, which can result in imaging times of several hours or longer. While volumetric XPC imaging can potentially benefit a variety of pre-clinical and clinical applications [198, 21], long imaging times currently prevent its widespread use. One approach to circumvent lengthy scan durations is to apply tomosynthesis methods [43, 44] that seek to reconstruct volumetric images from a relatively small number of projections spanning a limited angular range ($< 180^\circ$). Such images have anisotropic spatial resolution properties; the resolution is generally high in a particular transverse plane and poor in the direction perpendicular to that plane [132]. In this work, this direction will be referred to as the depth direction.

Although conventional AB tomosynthesis techniques have been extensively studied and implemented for numerous imaging applications [114, 157, 61], only a small number of studies have explored phase-contrast tomosynthesis and its potential advantages for various modalities that include diffraction enhanced, grating-based interferometric and edge illumination XPC imaging [101, 79, 191, 136, 152]. To date, relatively few publications have specifically

focused on propagation-based imaging methods [190, 151]. While previous studies [66, 167] showed PB-XPC tomosynthesis is able to produce boundary-enhanced in-plane images that better reveal tissue interfaces than conventional AB tomosynthesis, there remains a lack of reported experiments and analyses that discuss the resolving abilities of PB XPC tomosynthesis in the depth direction. In this Note, numerical and experimental investigations are presented that compare the ability of AB and PB-XPC tomosynthesis to distinguish between in-plane and out-of-plane structures. The results reveal that, in PB-XPC tomosynthesis, the phase-contrast-induced fringes can help discriminate in-plane structures from out-of-plane structures, thus providing better depth-position characterization than AB tomosynthesis.

2.2 BACKGROUND

2.2.1 PB XPC imaging model

A PB-XPC tomographic imaging geometry is depicted in figure 2.1. A reference coordinate system (x, y, z) is related to a rotating coordinate system (x_r, y, z_r) by $x_r = x\cos\theta + z\sin\theta$ and $z_r = z\cos\theta - x\sin\theta$, where the tomographic view angle θ is measured with respect to the positive x -axis. The y -axis defines the axis of tomographic scanning (isocenter). An X-ray source is located at $z_r = -R_1$; for simplicity, we assume for now that this is a monochromatic point source with wavelength λ .

The object can be characterized by its complex-valued refractive index distribution

$$n(\mathbf{r}) = 1 - \delta(\mathbf{r}) + j\beta(\mathbf{r}), \quad (2.1)$$

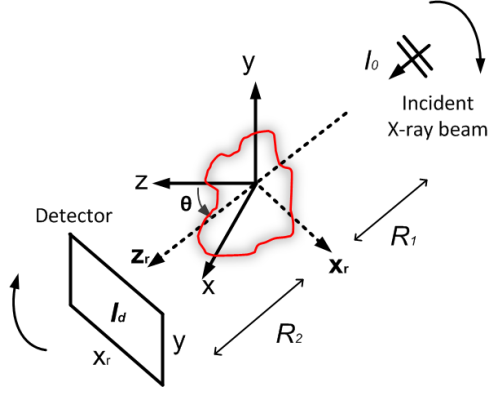


Figure 2.1: A schematic of the PB XPC imaging geometry is shown in which the object is fixed in a reference coordinate system (x, y, z) . The source (not shown) and detector rotate about the y -axis.

where $\mathbf{r} = (x, y, z)$. The projected attenuation coefficient $\mu_p(x_r, y, \theta)$ and the total phase shift $\phi_p(x_r, y, \theta)$ are respectively defined as

$$\mu_p(x_r, y, \theta) = 2k \int dz_r \beta(\mathbf{r}) \quad (2.2)$$

and

$$\phi_p(x_r, y, \theta) = -k \int dz_r \delta(\mathbf{r}), \quad (2.3)$$

where $k = 2\pi/\lambda$. The integrals are computed along the X-ray beam path, which is approximately the z_r -direction when paraxial conditions are assumed, as are throughout this work. The total attenuation experienced by the wavefield as it traverses the object is defined as

$$A(x_r, y, \theta) = \exp(-\mu_p(x_r, y, \theta)/2). \quad (2.4)$$

Assuming the phase varies moderately over a small distance and the near field approximation holds, the measured intensity approximately satisfies [170]

$$I_d(x_r, y, \theta) = I_0(x_r, y, \theta) \left\{ A^2(x_r, y, \theta) - \frac{2\lambda R_2}{\pi M} \nabla_{x_r, y}^2 [A^2(x_r, y, \theta) \phi_p(x_r, y, \theta)] \right\}, \quad (2.5)$$

where $M = (R_1 + R_2)/R_1$ and $\nabla_{x_r, y}^2$ is the 2D Laplacian operator acting on the (x_r, y) plane. The quantity $I_0(x_r, y, \theta)$ represents the wavefield intensity on the plane $z_r = 0$, i.e., the wavefield intensity incident on the object.

2.2.2 Data function

Consider the data function

$$g_{\text{xpc}}(x_r, y, \theta) \equiv -\log \left\{ \frac{I_d(x_r, y, \theta)}{I_0(x_r, y, \theta)} \right\}, \quad (2.6)$$

which can be formed from the known quantities $I_d(x_r, y, \theta)$ and $I_0(x_r, y, \theta)$. Under the assumptions required to establish equation (2.5) and additionally assuming weak absorption, this data function approximately satisfies [26]

$$g_{\text{xpc}}(x_r, y, \theta) = \mu_p(x_r, y, \theta) + \frac{2\lambda R_2}{\pi M} \nabla_{x_r, y}^2 \phi_p(x_r, y, \theta). \quad (2.7)$$

In the special case when $R_2 = 0$, equation (2.7) yields a data function for conventional AB tomosynthesis given by

$$g_{\text{abs}}(x_r, y, \theta) = \mu_p(x_r, y, \theta), \quad (2.8)$$

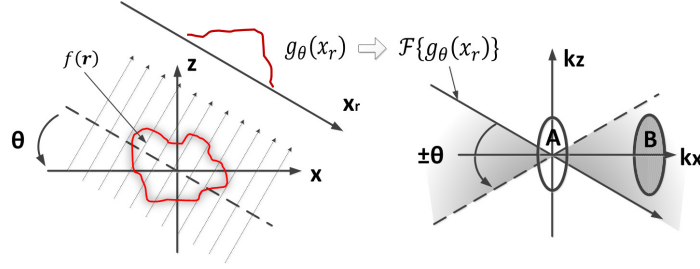


Figure 2.2: A parallel-beam projection along a direction θ in spatial domain corresponds to a plane acquired along θ in the frequency domain. This figure illustrates the reduced spatial resolution in the z -direction of reconstructed tomosynthesis images.

and therefore equation (2.7) can be expressed as

$$g_{\text{xpc}}(x_r, y, \theta) = g_{\text{abs}}(x_r, y, \theta) + \frac{2\lambda R_2}{\pi M} \nabla_{x_r, y}^2 \phi_p(x_r, y, \theta). \quad (2.9)$$

2.2.3 Interpretation of boundary-enhanced image

Given the assumed paraxial conditions, it has been demonstrated that the application of the Feldkamp-Davis-Kress inversion formula \mathcal{R}^{-1} to the PB XPC data function yields [26]

$$f(\mathbf{r}) \equiv \mathcal{R}^{-1}\{g_{\text{xpc}}\} = 2k\beta(\mathbf{r}) + \frac{R_2}{M} \nabla_{xyz}^2 \delta(\mathbf{r}), \quad (2.10)$$

where ∇_{xyz}^2 denotes the 3D Laplacian operator. Equation (2.10) defines the object function for boundary-enhanced PB XPC tomography (XPCT). The second term in equation 2.10 explains why this implementation of PB-XPCT produces boundary-enhanced images [164, 7, 139]. In this work, we seek to estimate $f(\mathbf{r})$ by use of PB XPC tomosynthesis methods.

2.2.4 Fourier slice interpretation of tomographic depth resolution

The well-known Fourier slice theorem states that a parallel-beam projection along a direction θ in space corresponds to a plane acquired along θ in the frequency domain. Let (k_x, k_y, k_z) denote the spatial frequency coordinates that are conjugate to (x, y, z) . Figure 2.2 illustrates the Fourier slice theorem and displays the (k_x, k_z) plane with a shaded region corresponding to the frequency component information contained in the measured data from a generic tomosynthesis scan covering the angular range $\pm\theta$ [132]. This figure can be utilized to explain why tomosynthesis produces limited depth resolution: the acquired information along the k_z -direction in region A is incomplete due to the limited angular range of the scan, especially at low frequencies near the origin. It also illustrates why depth resolution in tomosynthesis depends on object size; namely, small objects typically possess better resolution in the depth-direction than do larger objects [132, 3]. This is because for higher frequencies of k_x (corresponding to smaller feature sizes), there exists an increasing coverage in k_z (region B).

The result above is a characteristic of tomosynthesis methods in general. A similar analysis can be applied to interpreting the specific frequency domain characteristics of PB-XPC tomosynthesis signals. According to the PB-XPC imaging model described in equation (2.9), for a certain angle view, the Fourier transform of a PB-XPC projection satisfies

$$\mathcal{F}(g_{\text{xpc}}(x_r, y)) = \mathcal{F}(g_{\text{abs}}(x_r, y)) + \frac{\lambda R_2}{2\pi} (\mathbf{k}_{x_r}^2 + \mathbf{k}_y^2) \mathcal{F}(\phi_p(x_r, y)), \quad (2.11)$$

where \mathcal{F} represents the 2D Fourier transform operator acting on the (x_r, y) plane; \mathbf{k}_{x_r} and \mathbf{k}_y are the frequency variables conjugate to x_r and y . Due to the factor $(\mathbf{k}_{x_r}^2 + \mathbf{k}_y^2)$, the frequency components of the second term on the right-hand side of equation (2.11) will be amplified, with increasing amplification for increasing frequency. However, the frequency components

contained in the first term (attenuation term) will be unaltered. This indicates that the PB-XPC tomosynthesis data function g_{xpc} contains enhanced high-frequency components as compared to the conventional AB tomosynthesis data function g_{abs} . The interpretation of figure 2.2 indicates that there is a wider coverage of k_z in high-frequency data space, which implies PB-XPC tomosynthesis is able to preserve a significant amount of information content in k_z , allowing for improved ability of depth position characterization. This analysis can be extended readily to the polychromatic case, where the general conclusions remain unaltered. Computer-simulations and experimental studies that are based on a benchtop polychromatic X-ray source are described next.

2.3 MATERIALS and METHODS

2.3.1 Reconstruction algorithm

There are several reconstruction methods available for conventional tomosynthesis that can be applied to reconstruct boundary-enhanced images in PB-XPC tomosynthesis [53]. The most frequently employed reconstruction algorithm is commonly referred to as shift and add (SAA) [86]. However, SAA is essentially an unfiltered backprojection algorithm and will result in image blurring. Filtered backprojection (FBP) algorithms [90, 104] also have an inherent deficiency as they are based on the analytical inverse of the Radon transform, with the assumption that the complete data space has been densely sampled.

Iterative reconstruction algorithms have proven to be well suited to the tomosynthesis problem [168, 193]. Iterative algorithms are flexible in regard to the measurement geometry and

can mitigate data incompleteness. In this work, the vector $\mathbf{g}_{M \times 1}$ denotes the measured projection data that have been lexicographically ordered. The vector $\mathbf{f}_{N \times 1}$ is used to represent the 3D discrete object using voxels. The value of N corresponds to the number of voxels used to represent \mathbf{f} . The relationship between the acquired data \mathbf{g} and the discrete object \mathbf{f} can be described as

$$\mathbf{g} = \mathbf{H}\mathbf{f}, \quad (2.12)$$

where \mathbf{H} is an $M \times N$ system matrix that can be interpreted as a discrete operator representing a cone-beam projection transformation.

In this work, the estimates of \mathbf{f} were determined by solving the following total-variation (TV) regularized least square optimization problem [143, 175]:

$$\hat{\mathbf{f}} = \underset{\mathbf{f}}{\operatorname{argmin}} \{ \|\mathbf{g} - \mathbf{H}\mathbf{f}\|_2^2 + 2\zeta \|\mathbf{f}\|_{TV} \}, \quad (2.13)$$

where $\|\cdot\|_{TV}$ denotes the discrete TV (semi)-norm that can remove noise from the sought-after solution and ζ is a regularization parameter that balances the denoising effect and how well the solution fits the data. Equation (2.13) states that the sought-after solution $\hat{\mathbf{f}}$ corresponds to the vector \mathbf{f} that minimizes the value of the penalized least-squares cost function enclosed by the brackets.

A modified version of the fast iterative shrinkage/thresholding algorithm (FISTA) was employed to solve equation (2.13). The basic FISTA structure includes a gradient-based image update to obtain an intermediate solution and then a proximal map problem solved by fast gradient projection (FGP) algorithm. A detailed description of the standard FISTA in the 2D case can be found elsewhere [13]. We developed an advanced algorithm that extended the FGP algorithm to the 3D case and incorporated the concept of ordered subsets (OS) with

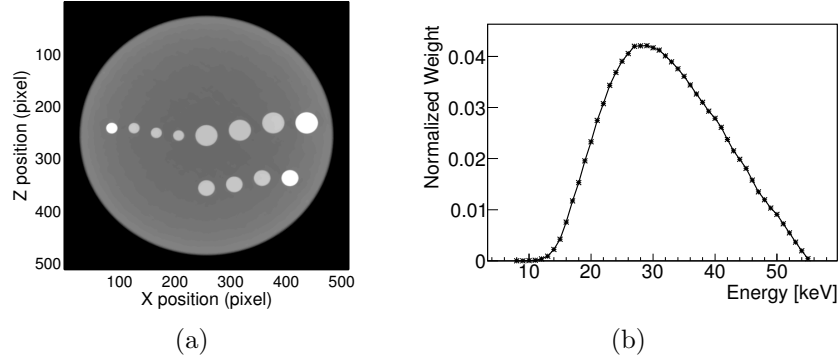


Figure 2.3: The phantom and the spectrum employed in the computer simulation. (a) A central slice through the numerical soft tissue phantom employed in the tomosynthesis simulations is shown in the left panel (viewed from above along the positive y -axis). The larger enclosing sphere is 4mm in diameter and is composed of healthy breast tissue. Diameters of internal spheres range from $80\mu\text{m}$ to $160\mu\text{m}$ and are composed of adipose tissue (grey) and calcium sulfate (white). (b) The right panel shows the polychromatic x-ray spectrum assumed in the tomosynthesis simulations. The y -axis gives the normalized weight for each energy bin.

SART (Simultaneous Algebraic Iterative Reconstructive Technique) to dramatically increase the convergence speed [172, 173].

2.3.2 Simulation Studies

Phantom design: Figure 2.3(a) shows a central slice of the numerical phantom employed to investigate the depth resolution properties of PB-XPC tomosynthesis. An x - z slice through the phantom is displayed. Eight spheres were placed in a row along the x -direction with the z -coordinate of their center positions slightly offset from one another. Four additional spheres were located in a row off-center from the axis of rotation with a similar arrangement of their central locations. These spherical volumes were assigned realistic tissue properties (large sphere: breast tissue; internal spheres: adipose and calcium sulfate) to mimic healthy soft tissue and calcifications. The refractive index values were analytically calculated [179]

based on their respective element composition¹ and atomic scattering factors². Three sizes of internal sphere were employed (diameters: 80 μm , 120 μm and 160 μm) and the diameter of the phantom was 4mm. To avoid numerical difficulties in applying the Laplacian operator in the imaging model (equation (2.10)), a 3D Gaussian blurring kernel (FWHM=10 μm) was applied to the numerical phantom model, which ensured that the boundaries between different tissues were differentiable.

Imaging system: The geometry of the simulated tomosynthesis imaging system is illustrated in figure 2.1. The source and flat-panel detector simultaneously rotate in full isocentric motion with a specified angular step (2°) and scan range ($\pm 20^\circ$). The input energy spectrum of the simulated X-ray beam (figure 2.3(b)) was provided by an on-line toolbox that modeled a polychromatic source with a solid tungsten anode operated at 55 kVp³. The simulated polychromatic projections were calculated as the weighted sum of the detected intensity associated with each energy component of the spectrum. The X-ray detector was modeled with 8-micron pixel pitch in a 1024×1024 pixel² flat panel array. The source-to-isocenter distance R_1 was set to be 50cm.

Simulated data: According to the paraxial Fresnel diffraction theory, both AB and PB-XPC tomosynthesis measurement data were numerically generated by convolving the X-ray wave function right through the object (at $z=R_1$) with the Fresnel-Kirchhoff kernel [129]. Different propagation distances $R_2=0$ cm and $R_2=50$ cm were chosen for AB and PB-XPC scenarios, respectively. As depicted in figure 2.1, the projection at $\theta=0$ corresponded to the incident beam traveling in the $+z$ direction. Realistic blurring factors were considered (e.g. the finite source spot size, and the limited detector resolving power) by applying an additional 2D

¹<http://physics.nist.gov/PhysRefData/XrayMassCoef/tab2.html>

²<http://physics.nist.gov/PhysRefData/FFast/html/form.html>

³<https://w9.siemens.com/cms/oemproducts/Home/X-rayToolbox/spektrum/Pages/radIn.aspx>

Gaussian blurring kernel (FWHM=40 μm) to the simulated intensity data. For simplicity, 1% (with respect to the noiseless pixel value) uncorrelated Gaussian noise was added to the projection data. This noise model is consistent with the experimental studies described below, in which a large number of photons were detected.

Image reconstruction: The iterative algorithm described in Section 2.3.1 was employed to reconstruct AB and PB-XPC tomosynthesis images from the simulated measurements. The voxel size of the reconstructed images was 8 μm^3 . The regularization parameter ζ was empirically set at 0.5 for all studies. By convention, reconstructed x - y slices are referred to as *in-plane* images throughout this paper; reconstructed x - z slices are correspondingly referred to as *in-depth* images.

2.3.3 Experimental Studies

Imaging system: Experimental AB and PB-XPC projection data were acquired. The imaging system employed in the experimental studies contained a Kevex PSX10-65W microfocus source with a tungsten anode (Thermofisher) and a super-cooled Si-based CCD camera with 15 micron pixel pitch, 36 cm^2 detection area (Quad-RO, Princeton Instruments). A detailed description of the imaging system can be found elsewhere [51]. In contrast to the system configuration employed in the simulations in which the source/detector rotates about a fixed object, the experimental system is configured with a fixed source/detector and rotating object. Both configurations represent complete isocentric motion and are in all respects equivalent except for the frame of reference. The data for the experimental component of the study were acquired with the X-ray source operated at 45kV and a spot size of 9 μm .

Data acquisition: The object in the experimental study was a formalin-fixed mouse lung placed in a 1 cm³ centrifuge tube. As that in the PB-XPC simulations, the sample was positioned midway between the source and detector, indicating that $R_1=R_2$. The relative amount of phase-contrast effects present in projection images was modified by selecting short (13 cm) and long (74 cm) propagation distances (i.e. R_2 in equation 2.7) to record “AB-like” and XPC projection data, respectively. It should be noted that we employed a cone beam geometry and maintained a constant geometric magnification factor ($M = 2$) for both AB and XPC cases so that effective pixel size ($= 15\mu\text{m}/M$) would be constant and not affect comparison of AB and XPC results. The Pb shielding for our X-ray source results in a minimum R_1 of 13cm. Accordingly, we utilized $R_2 = 13$ cm to acquire “AB-like” images that had the same geometric magnification ($M = 2$). The exposure times were 0.7 s and 80 s, respectively. The imaging dose was not held constant but this does not affect our conclusions in any way. The experimental tomosynthesis data sets contained 21 equally spaced projections where the sample was rotated from -20° to $+20^\circ$. A complete CT data set was also acquired ($R_2=13\text{cm}$, 100 projections with an angular step of 2°) to generate a reference image for comparison. All images were reconstructed by use of the iterative algorithm with a voxel size of $30 \mu\text{m}^3$. The reconstructed AB and PB-XPC tomosynthesis images were analyzed to compare and contrast their respective depth-position-characterization features.

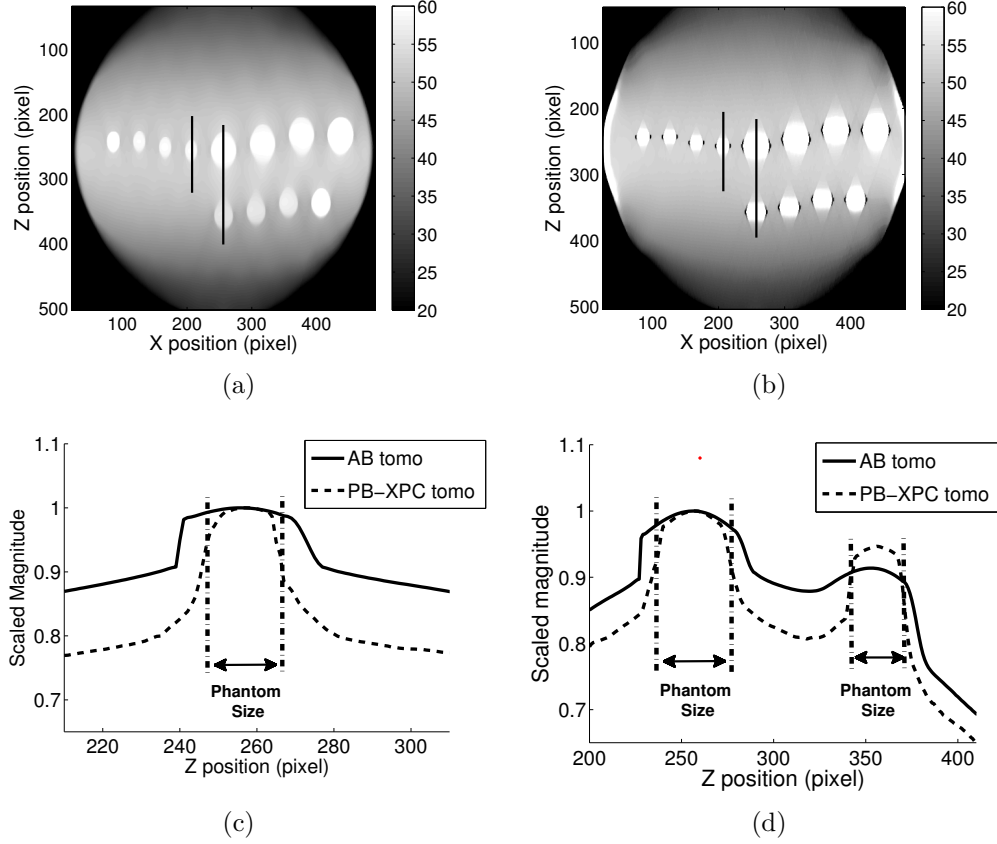


Figure 2.4: The reconstructed horizontal slices (in-depth images) are shown for AB (a) and PB-XPC (b) tomosynthesis scans of the numerical phantom displayed in figure 2.3(a). The grayscale window represents attenuation coefficient (m^{-1}). Two vertical lines in the top panels are extracted, and the corresponding scaled profiles are shown and compared in the bottom panels: (c) for the profile at $x=210$, and (d) for the profile at $x=256$.

2.4 RESULTS

2.4.1 Simulation Studies

In-depth images (x - z plane, $y=256$) reconstructed from the simulated AB and PB-XPC tomosynthesis data are shown in figure 2.4(a) and 2.4(b), respectively. In both figures, the reconstructed objects are no longer sphere-like but are distorted along the z -direction. To better compare the results, profiles along z -direction at $x=210$ and $x=256$ were extracted and plotted in figure 2.4(c) and 2.4(d). Each profile was normalized to its maximum magnitude. The horizontal double-arrow lines indicate the true size of the phantom's internal spheres in this plane. This comparison shows the PB-XPC tomosynthesis profile more accurately represents the structure of the phantom than does the AB tomosynthesis profile. In addition, the PB-XPC profiles presents a higher signal-background contrast, and ultimately performs better than AB tomosynthesis in terms of reproducing the size of the spherical objects inside the phantom. Similar findings were observed (not shown) in the profiles of other spheres corresponding to calcifications. It is also notable that both profiles are more closely aligned with the true structure of the smaller sphere than the larger sphere, as predicted through the Fourier slice interpretation discussed in Section 2.2.4.

Another feature to note in the reconstructed PB-XPC images is the spatial distribution of the edge-enhanced features displayed in figure 2.4(b). It is observed that the fringes in the in-depth XPC image are prominent near the true z -position of the spherical inclusions and are not present away from this position. In this simple computer-simulation where the object inclusions are modeled as uniform spheres, the center of masses of the blurred spheres in the AB image could also be employed to estimate the locations of their centers. However, in the more general situation where the inclusions do not possess symmetry, this

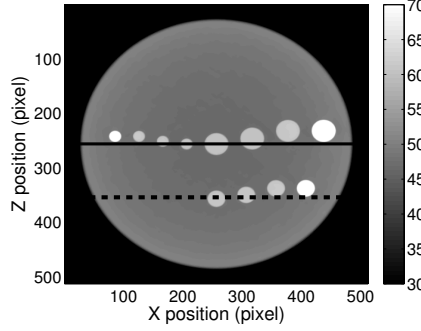


Figure 2.5: An overhead view of the numerical phantom is shown to indicate two depth positions ($z=256$, $z=354$) where the corresponding in-plane images (x - y plane) are to be extracted for the investigation of depth position determination (see figure 2.6 and 2.7).

would not always be the case. These observations suggest that the edge-enhanced features in PB-XPC tomosynthesis can potentially allow for improved depth-position determination of reconstructed in-plane structures compared to that from AB tomosynthesis.

In order to investigate this further, reconstructed in-plane images (x - y plane) from two different z -positions were extracted for comparison between AB and PB-XPC results. As shown in figure 2.5, one slice was selected from a depth position corresponding to the middle of the phantom (i.e. the isocenter, $z=256$ *solid line*) and the other slice was chosen from an off-center plane ($z=354$, *dashed line*).

In figure 2.6, the top row shows the reconstructed in-plane images (corresponding to the beam direction $\theta=0$) at the central depth position ($z=256$); the associated line profiles for $y=256$ are shown in the bottom row. For the AB tomosynthesis result (*left column*), all eight of the spheres appear in this reconstructed slice and it is not possible to determine which spheres are actually located at this z -position. Some criteria, like the magnitude or the visual size of the reconstructed object, might be misleading when used to determine the presence of the spheres. For PB-XPC tomosynthesis (*middle column*), all spheres are also present in the

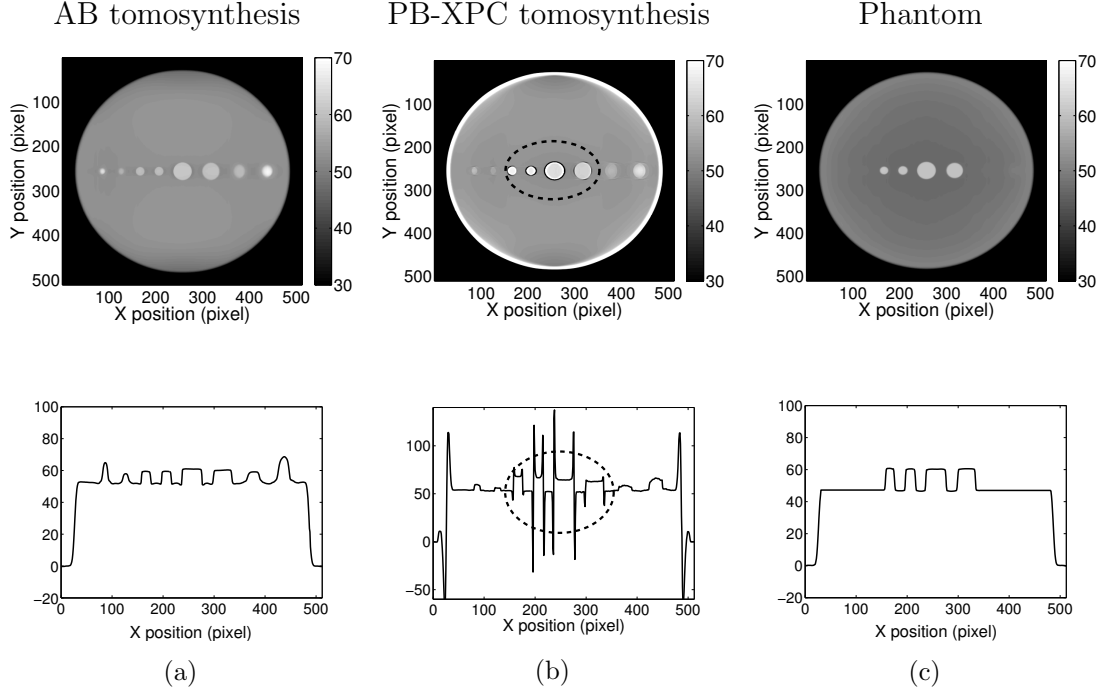


Figure 2.6: The comparisons of reconstructed in-plane images at depth position $z=256$ (*top row*) and associated profiles (*bottom row*) are shown here. (a) The line profiles from AB tomosynthesis result show similar signals from all internal spheres. (b) The PB-XPC tomosynthesis result reveals edge-enhancement for some of the internal spheres. (c) The true in-plane phantom structure shows that only the edge-enhanced spheres in (b) are actually located at that z -position of the reconstructed slice.

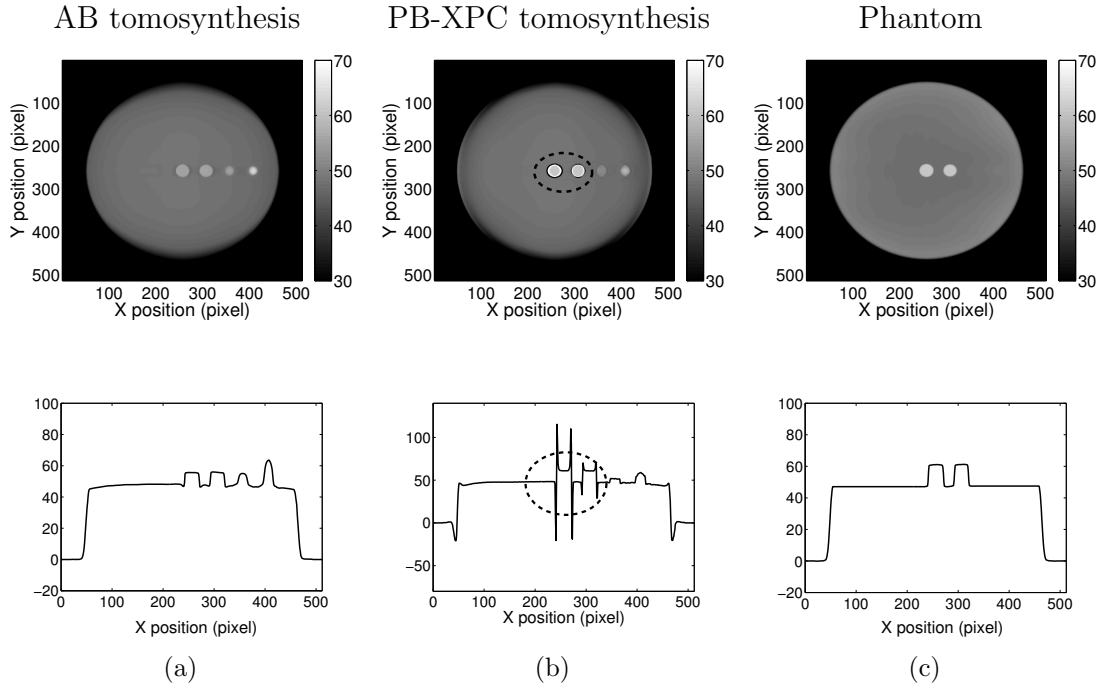


Figure 2.7: A comparison of reconstructed in-plane images at an off-center depth position $z=354$ (*top row*) and associated profiles (*bottom row*) is presented. The interpretation is similar to that in figure 2.6.

reconstructed image, however, only four of them exhibit fringes (*enclosed in ellipse*) while the others do not. Based on the previous observation, it is reasonable to suspect that these four spheres are truly located at this z -position, and the other image features are stretched artifacts from spheres located outside this particular plane. The corresponding slice of the numerical phantom (*right column*) verifies this interpretation and demonstrates that only the structures with fringes in the XPC reconstructed image are located in this plane. The reader should note the different y -axis range of panel (b) compared to panels (a) and (c), which was expanded to display the full extent of edge-enhanced features.

In figure 2.7, a similar comparison is displayed for the reconstructed in-plane image located at an off-center x - y plane ($z=384$). There are four spheres appearing in the resulting slice, but again, the AB tomosynthesis reconstruction (*left column*) does not provide enough information to distinguish the structures truly located at this plane. Through the presence of edge-enhanced features, the PB-XPC tomosynthesis image allows for estimation of which spheres are veritably present (*enclosed in ellipse*). This can be verified by examining the corresponding plane of the numerical phantom (*right column*). These results again demonstrate that boundary-enhancement in PB-XPC tomosynthesis provides capabilities to discriminate between in-plane structures and out-of-plane contamination. In addition, this capability proves to persist for depth positions away from the center of rotation.

2.4.2 Experimental Studies

An additional investigation of depth position characterization in PB-XPC tomosynthesis was conducted through imaging experiments. An extracted mouse lung was imaged with both AB and PC-XPC tomosynthesis configurations as well as with conventional CT. Figure 2.8 shows

a typical projection acquired from the two tomosynthesis setups. The PB-XPC projection (*right panel*) contains regions that exhibit significant intensity variation with a speckled appearance [84, 150] while the AB projection (*left panel*) does not. Two diverging airways and numerous smaller structures can be identified from the reconstructed in-plane images displayed in figure 2.9. Results for AB tomosynthesis (*left column*), PB-XPC tomosynthesis (*middle column*) and conventional x-ray CT (*right column*) are presented along with profiles for selected lines across each of the large airways (arrow indicators). The top and bottom rows in figure 2.9 correspond to reconstructed slices at two different z -positions of 4.2mm and 4.3mm (Depth 1 and Depth 2). The physical dimensions of ROIs are $3.5 \times 3.5 \text{mm}^2$, and the width of the large airway is $250 \mu\text{m}$.

Through examination of the AB tomosynthesis result at Depth 1 in figure 2.9(a), it is difficult to conclude if either airway is actually located at this depth position. However, XPC imaging methods proved itself able to fulfill this objective, because the left airway branch in the PB-XPC tomosynthesis result shown in figure 2.9(b) exhibits strong edge-enhancement along the tissue-air boundary (*enclosed in ellipse*) while the right airway does not. This edge-enhancement is readily observed in the extracted profiles. The full-view CT result in figure 2.9(c) serves as the reference and confirms that only the left branch is located in the corresponding plane.

The bottom row of figure 2.9 corresponds to a second plane located a distance of $100 \mu\text{m}$ in the positive z -direction from the slice at Depth 1. At Depth 2, the AB tomosynthesis image in figure 2.9(d) shows little difference between the appearances of the two airways; while the PB-XPC tomosynthesis image in figure 2.9(e) displays strong edge-enhancement at the boundaries of the airway on the right. In this in-plane, the XPC result successfully identifies

the right airway as the real structures but not the left one, which proves to be consistent with the corresponding slice of CT result in figure 2.9(f).

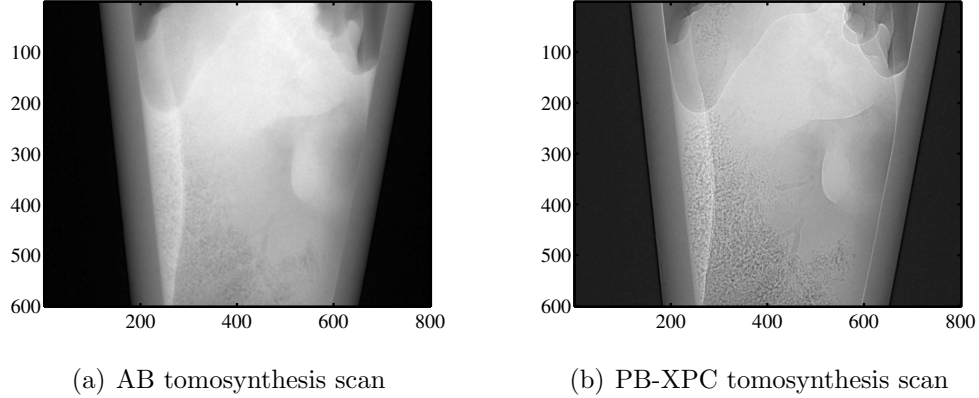


Figure 2.8: One typical projection image of an *ex-vivo* mouse lung sample acquired with different propagation distances. (a) $R_1=R_2=13\text{cm}$ for the AB tomosynthesis scan; (b) $R_1=R_2=74\text{cm}$ for the PB-XPC tomosynthesis scan. Due to the high phase-contrast sensitivity during acquisition, the PB-XPC projection presents more features of weakly absorbing microstructure than the AB projection.

2.5 CONCLUSION AND DISCUSSION

Conventional AB tomosynthesis has previously been applied in both research studies and diagnostic breast/chest imaging applications. Although tomosynthesis methods are able to add a third dimension of information to that provided by conventional 2D radiographs, discerning real structures from those contaminated from other depth positions remains one of the challenges in interpreting the images. PB-XPC tomosynthesis combines desirable aspects of XPC imaging and tomosynthesis. It can provide volumetric information describing weakly absorbing structures and reduce imaging times and doses as compared to XPC CT. The results presented here demonstrate that PB-XPC tomosynthesis can also provide

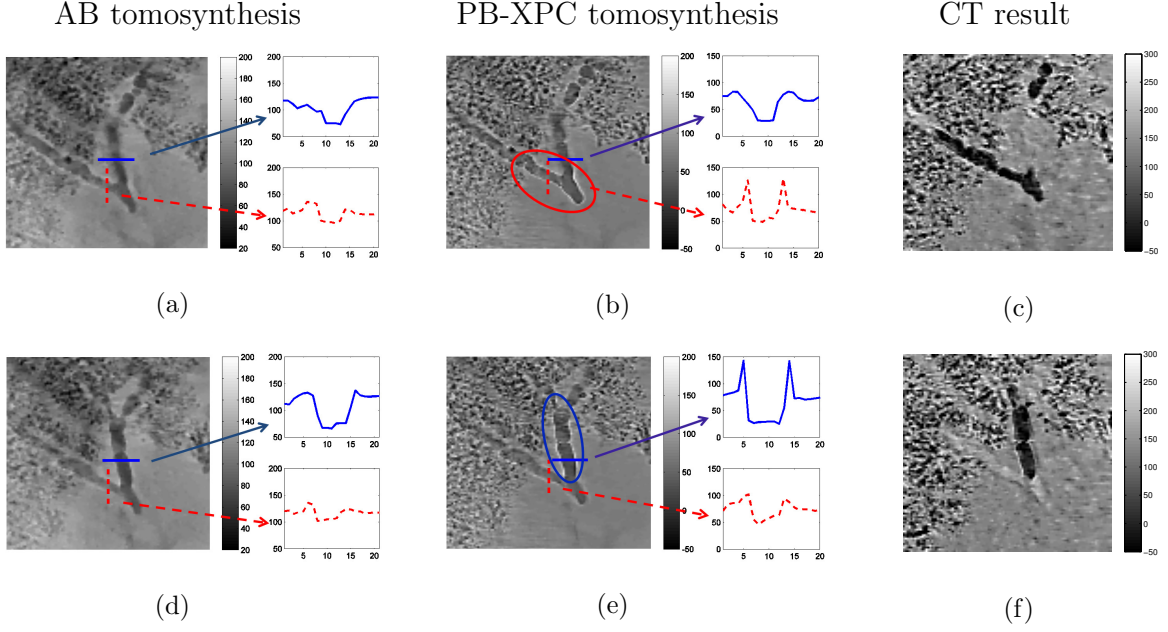


Figure 2.9: A comparison of reconstructed in-plane images for an *ex-vivo* mouse lung is shown. The grayscale window represents attenuation coefficient (m^{-1}). The top and bottom rows correspond to in-plane slices located at $z=4.2\text{mm}$ and $z=4.3\text{mm}$, respectively, of the reconstructed 3D volume from AB tomosynthesis (a,d), PB-XPC tomosynthesis (b,e), and full-view CT (c,f) data sets. Two airways are seen in the tomosynthesis results and their line profiles are delineated as the arrows indicate. For each row, edge-enhancement in the PB-XPC reconstructions is able to provide a method to identify structures that are truly located at the particular z -position, which is verified by the corresponding CT result.

improved depth position characterization compared with conventional AB tomosynthesis. More specifically, the simulation results and experiment studies show that structures truly located in a specific plane may display strong boundary-enhancement in PB-XPC tomosynthesis reconstructions while out-of-plane structures do not. This effect can facilitate the identification of in-plane structures.

As demonstrated in our studies, the presence of boundary-enhancement in PB-XPC tomosynthesis is shown to be a signature of the true presence of in-plane structures; however, one should note that the lack of such evidence is not necessarily an absolute indicator of an out-of-plane artifact. Our results show the prominent fringes employed for depth position characterization come from the tissue boundaries associated with high k_x or high k_y frequencies, therefore edge-enhancement do not cover the entire perimeter of the object (e.g. those boundaries mainly along x -direction); there could be in-plane structures without edge-enhancement that also correspond to truly existing objects. The spatial distribution of fringes depends on the scan angular range of tomosynthesis acquisition. In addition, although boundary-enhancement is useful for depth position determination, the detection of fringes is essentially a binary decision task that is not always straightforward to accomplish, especially for those cases where the edge-enhancement is not significant and/or the images contain a high noise level. A few studies related to edge detection have been reported in the previous research [87, 182]. Finally, alternative tomosynthesis scanning configurations exist with different relative motion between source, object and detector. It is uncertain if the results presented here for complete isocentric motion can be translated directly to other scanning setups. A natural next step in the course of this work is to further investigate these issues as well as other factors affecting PB-XPC sensitivity such as lateral coherence and propagation distance.

Chapter 3

A subspace-based resolution enhancing image reconstruction method for few-view differential phase-contrast tomography

It is well-known that properly designed image reconstruction methods can facilitate reductions in imaging doses and data-acquisition times in tomographic imaging. The ability to do so is particularly important for emerging modalities such as differential X-ray phase-contrast tomography (D-XPCT)[127], which are currently limited by these factors. An important application of D-XPCT is high-resolution imaging of biomedical samples. However, reconstructing high-resolution images from few-view tomographic measurements remains a challenging task due to the high-frequency information loss caused by data incompleteness. In this work, a subspace-based (SuB) reconstruction strategy is proposed and investigated for use in few-view D-XPCT image reconstruction. By adopting a two-step approach, the proposed method can simultaneously recover high-frequency details within a certain region

of interest (ROI) while suppressing noise and/or artifacts globally. The proposed method is investigated by use of few-view experimental data acquired by edge-illumination D-XPCT scanner.

3.1 Introduction

X-ray phase-contrast imaging (XPCI) methods continue to be actively developed and investigated for characterizing soft tissue or biological samples that present limited X-ray absorption contrast[38, 128, 92, 103, 9, 60, 20]. A variety of XPCI methods have been proposed, which include propagation-based imaging[170, 62], crystal analyzer-based imaging[30, 165], grating-based imaging based on the Talbot or Talbot-Lau effect[163, 128] and edge-illumination imaging[65, 64, 32]. Conventional implementations of the crystal analyzer-, grating-, and edge-illumination-based methods are generally referred to as differential XPCI methods, since they typically yield estimates of the one-dimensional (1D) derivative of the projected real-valued component of the refractive index distribution of an object. In this work, a tomographic implementation of differential XPCI is considered, referred to as differential X-ray phase-contrast tomography (D-XPCT). The goal of D-XPCT is to produce an estimate of the real-valued component of the refractive index distribution, which describes the spatially variant refractive properties of an object.

It will be assumed that the tomographic data function, from which an estimate of the refractive index distribution is reconstructed, corresponds to 1D derivative with respect to the detector row coordinate of the two-dimensional (2D) Radon transform of the refractive index distribution. This tomographic data function can be established by application of a phase-retrieval method [128, 165, 34, 117, 42] to the measured intensity data. When the data

function is known at a sufficiently large number of tomographic views [145], image reconstruction in D-XPCT can be readily accomplished by use of a modified filtered backprojection (FBP) algorithm [47, 69, 127].

However, in current implementations of D-XPCT, it may not be desirable to acquire data at a large number of tomographic view angles. This is because D-XPCT methods are currently limited by relatively long data-acquisition times and radiation exposures, which has hindered the widespread application of the method to *in vivo* applications. Since current implementations typically utilize a 'step-and-shoot' data-acquisition protocol, as opposed to the continuously rotating X-ray source and detector pair utilized in a clinical CT scanner, one way to mitigate this problem is to acquire tomographic measurements at a reduced number of view angles. The associated image reconstruction problem is generally referred to as a 'few-view' image reconstruction problem [140, 15]. It might be worth mentioning that recently a phase CT has been developed with a lab source using continuous rotation in a few minutes, but the limitation in that case is the approximation in the phase retrieval.

There exists a vast literature related to few-view image reconstruction [140, 192, 187, 141, 184]. Modern few-view image reconstruction methods are optimization-based and typically utilize an iterative method to find a finite-dimensional estimate of the object function that approximately minimizes an objective function subject to constraints. In the case of D-XPCT, the object function corresponds to the refractive index distribution. While existing few-view reconstruction methods can be adapted for use in D-XPCT [175, 85, 116, 115], there remains a need for improved methods for reconstructing high-resolution D-XPCT images from few-view measurements. Because few-view image reconstruction corresponds to an ill-conditioned inverse problem, a regularized solution must be computed; however the design of

an effective regularization strategy is influenced by many factors, including the characteristics of the refractive index distribution to be estimated.

Regularization methods that promote object sparsity [140, 27] are ubiquitous in the modern image reconstruction literature. Although total variation (TV) regularization has been employed widely, its effectiveness is degraded when the object’s gradient map is not sparse [174, 175]. To mitigate this problem, object sparsity can be promoted in a different transform domain in which the object is sparsely represented [146]. Analytical sparsifying transforms such as wavelets, curvelets, and finite differences can be employed. Alternatively, the sparsifying transform can be adaptively learned from a set of training data [177, 130]. Moreover, multiple penalty functions can be employed in the objective function in order to obtain a balanced regularization[196], or more complicated strategies can be employed that achieve local TV regularization effects in the image domain[153]. However, it remains challenging to design a regularization strategy that faithfully preserves fine object features in the reconstructed image when only few-view tomographic data are utilized.

In this work, a new method for few-view image reconstruction in D-XPCT is proposed and investigated. A distinctive feature of the method is that the sought-after object function is decomposed into two components that reside in distinct subspaces. One component corresponds to the high frequency components of the object function that reside within a certain region of interest (ROI). The radius of the ROI is determined by the spatial frequency content of the object function and the number of tomographic view considered. This object component can be stably recovered from the few-view measurement data using a Penalized Least-Squares (PLS) estimator. The second component corresponds to the lower frequency components of the object function, over the entire support of the object. This object component, which is slowly varying, can be accurately estimated by use of a TV-regularized

PLS estimator (PLS-TV). In this way, the high frequency components of the object function within the ROI can be faithfully preserved, while outside of the ROI lower-frequency components of the object can be accurately recovered and streak artifacts can be suppressed. The proposed subspace-based method is applied to few-view experimental data acquired by use of a benchtop edge-illumination D-XPCT system and its performance is compared to the conventional FBP and PLS-TV methods.

3.2 Background

3.2.1 D-XPCT imaging model in semi-discrete form

It will be assumed that all functions below are compactly supported and belong to weighted \mathbb{L}^2 -spaces. For a function $f(\mathbf{r})$ that is compactly supported on a disk $D \subset \mathbb{R}^2$, the two-dimensional (2D) Radon transform of the function is defined as

$$(\mathcal{R}_c f)(s, \phi) = \int_{-r}^r f(\mathbf{r}) \delta(s - \mathbf{r} \cdot \mathbf{n}) d\mathbf{r}, \quad (3.1)$$

where $s \in (-r, r)$ denotes the detector row coordinate, $\phi \in (0, \pi)$ denotes the tomographic view angle, and $\mathbf{n} = \{\cos\phi, \sin\phi\}$ is a unit vector making angle ϕ to the x -axis.

Considering the case of few-view measurement data where only a finite number of views are available, the corresponding finite-view Radon transform can be defined by discretizing \mathcal{R}_c with respect to the tomographic view angle:

$$(\mathcal{R}f)(s, \phi_i) = \int_{-r}^r f(\mathbf{r}) \delta(s - \mathbf{r} \cdot \mathbf{n}_i) d\mathbf{r}, \quad (3.2)$$

where $\mathbf{n}_i = \{\cos\phi_i, \sin\phi_i\}$ and ϕ_i belongs to a set S that contains discrete tomographic view angles indexed with $i = 1, 2, \dots, M$. Therefore, \mathcal{R} is a compact operator from $\mathbb{L}_2(D)$ into $\mathbb{L}_2(Z)$, where $Z = [-r, r] \times S$.

The D-XPCT imaging model can be described as a finite-view differential Radon transform $\mathcal{H} = \mathcal{D}\mathcal{R}$, where \mathcal{D} is a one-dimensional first-order derivative operator:

$$g(s, \phi_i) = \mathcal{H}f(\mathbf{r}) \equiv \mathcal{D}\mathcal{R}f(\mathbf{r}) = \frac{\partial}{\partial s} \int_{-r}^r f(\mathbf{r}) \delta(s - \mathbf{r} \cdot \mathbf{n}_i) d\mathbf{r}. \quad (3.3)$$

Here, $g(s, \phi_i)$ is a tomographic data function that is established by use of a phase retrieval method[88, 109, 108, 183].

The image reconstruction task in D-XPCT is to determine an estimate of $f(\mathbf{r})$, which represents the refractive index distribution, from knowledge of $g(s, \phi_i)$. When the data function $g(s, \phi_i)$ is determined at a large number of view angles, this can be accomplished by use of analytical image reconstruction algorithms[50]. For example, images can be reconstructed by use of a modified FBP method as[127]

$$\hat{f}_{\text{FBP}} = \mathcal{R}^\dagger C_h g, \quad (3.4)$$

where \dagger indicates the adjoint operator, and C_h is a filter kernel acting as the Hilbert transform scaled by a factor. Typically the scaling factor equals the angular spacing $\Delta\phi$ if all the projections are uniformly acquired over the π span. Here \mathcal{R}^\dagger , usually referred to as the back projection operator, is mathematically equivalent to discretizing \mathcal{R}_c^\dagger with respect to the variable ϕ :

$$(\mathcal{R}^\dagger g)(\mathbf{r}) = \sum_{i=1}^M \left[\int_{-r}^r g(s, \phi_i) \delta(s - \mathbf{r} \cdot \mathbf{n}_i) ds \right]. \quad (3.5)$$

Note that Eq. (3.4) appears similar to the classical FBP algorithm for CT image reconstruction, where the reconstruction kernel has been modified. However, in the case of noisy and/or few-view measurement data, analytic reconstruction methods are known to be suboptimal and the use of iterative methods is highly desirable.

3.2.2 Null-space properties of finite-view Radon transform

The finite-view Radon transform \mathcal{R} is a semi-discrete version of the classical Radon transform in which only discretization of the angular variable is performed. A unique and exact reconstruction of an arbitrary function is mathematically impossible when the tomographic data contains only a finite number of views. This implies that the finite-view Radon transform has a non-trivial null space. The functions in this null space, denoted as f_{null} , are invisible along the considered projection directions, or mathematically speaking, $\mathcal{R}f_{null} = \mathbf{0}$, where $\mathbf{0}$ is an infinite-dimensional zero vector defined in the range of \mathcal{R} . Correspondingly, the orthogonal complement of the null space is defined as measurable space.

By use of various mathematical tools, for example the orthogonal function series expansions or singular value decomposition, important insights into the null-space properties of the finite-view Radon transform have been established[96, 98, 28, 97, 145, 76]. Defining a compact disc support of radius r , and assuming a set of M equispaced projections over π span, Logan[96] revealed that the 2D Fourier transform of any null-space function corresponding to the imaging operator \mathcal{R} is negligible inside a disc of radius Ω in Fourier space when

$$\Omega = M/(2\pi r), \tag{3.6}$$

as illustrated in figure 3.1(a), where the estimate holds when $M \gg \pi/2$.

As a direct consequence, a function whose 2D Fourier transform is concentrated within this frequency disk Ω can be reliably reconstructed from its M projections[76]. An intuitive illustration is provided in figure 3.1(b). If the frequency contents of the object do not fall into the null space of the finite-view Radon transform, the object can be accurately reconstructed. More rigorous mathematical proofs can be found in previous works[145, 28].

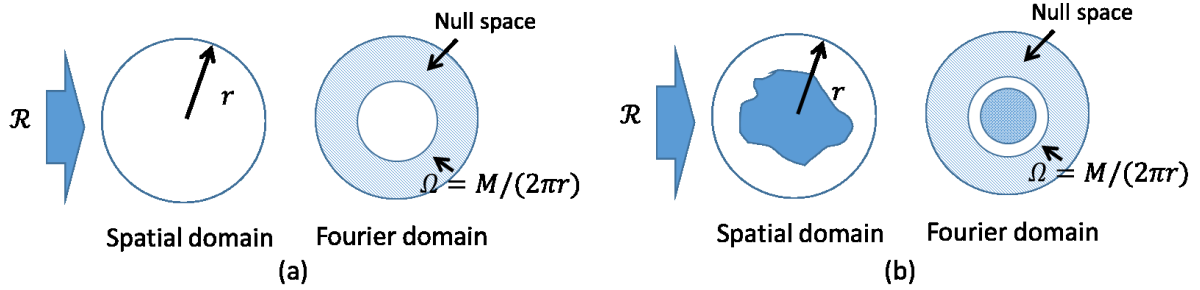


Figure 3.1: (a) The null-space functions of the finite-view Radon transform are contained exclusively outside a disk Ω in the Fourier domain, shown as the gray region. (b) If a to-be-imaged object has all the frequency contents confined to Ω without overlapping the null-space region, it means the object could be reliably reconstructed.

Remark 1: The above argument has been a long-time guide for determining the angular sampling requirements for a CT scan[76]. For non-truncated projections, the D-XPCT data set can be readily converted to a CT data set by use of an integral operator, without any information loss. So the conclusion is also valid for the D-XPCT imaging scenario.

Remark 2: For an imaging operator \mathcal{R} with the support radius and number of views already defined, the above argument tells under what conditions the image can be reliably reconstructed, which does not rely on any specific reconstruction algorithm. In practice, FBP-type algorithms taking the form of Eq. (3.4) have been widely implemented in CT, proving reliable reconstructions as long as the relationship of Eq. (3.6) is satisfied[145, 76, 133].

Remark 3: A compactly supported object theoretically does not have a strictly band-limited frequency distribution; therefore one should keep in mind that the argument only holds when we can assume the measurements are quasi-band-limited, which is the case in many practical implementations[122].

3.3 Motivation for subspace-based image reconstruction

3.3.1 Revisiting the FBP algorithm

When the imaging system corresponds to a field of view (FOV) of radius r that does not meet the requirement in Eq. (3.6), the aforesaid angular sampling is insufficient for an accurate reconstruction when the FBP algorithm is employed. From the perspective of the Fourier slice theorem, the acquired data suffer a significant high-frequency information loss, and a blurred reconstructed image is expected. However, it is interesting that, though the conventional FBP algorithm is known to give rise to streak-like aliasing artifacts, the reconstructed image looks sharper and more resolution-enhanced in comparison to the image that reflects the measurable component of the object[186]. Here, the measurable component f_{meas} is defined as the part of the object that lies in the measurable space of the operator \mathcal{R} . It can be interpreted as the least-square estimate of the object that has the minimum L2-norm, known as the pseudo-inverse solution, which can be computed by use of the Landweber iterative algorithm or other inversion methods[12].

In order to better interpret an image produced by use of the FBP algorithm, the to-be-imaged object f can be decomposed into two components as $f = Wf + (1 - W)f$. Here, W is a 0-1 function that performs as a circular mask with the center at the origin, such that

$$W(\vec{r}) = \begin{cases} 1 & \text{if } \|\vec{r}\| < r' \\ 0 & \text{elsewhere,} \end{cases} \quad (3.7)$$

where the radius r' is determined as

$$r' = M/(2\pi\Omega). \quad (3.8)$$

As introduced in Eq. (3.6), Ω denotes the maximum spatial frequency of the object. Motivated by the previous null-space properties of the finite-view Radon transform, W specifies the largest ROI that can potentially be reliably reconstructed, as will be discussed below.

Denote the FBP reconstruction operator as $\mathcal{B} = \mathcal{R}^\dagger C_h$ for a given finite-view D-XPCT problem, where the back projection operator \mathcal{R}^\dagger and filter C_h are defined as in Eq. (3.4). Assuming consistent data $g = \mathcal{H}f$, an image reconstructed by use of the FBP algorithm can be expressed as

$$\hat{f}_{\text{FBP}} = \mathcal{B}g = W\mathcal{B}g + (1 - W)\mathcal{B}g. \quad (3.9)$$

The reconstructed image within a designated ROI of radius r' can be isolated by applying the mask W on \hat{f}_{FBP}

$$\begin{aligned} W\hat{f}_{\text{FBP}} &= W\mathcal{B}g \\ &= W\mathcal{B}\mathcal{H}f \\ &= W\mathcal{B}\mathcal{H}Wf + W\mathcal{B}\mathcal{H}(1 - W)f. \end{aligned} \quad (3.10)$$

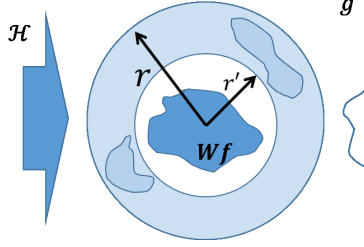


Figure 3.2: The illustration of the reconstruction over the support r and with a virtual mask W . FBP algorithm ensures that the reconstruction of ROI within r' is not affected by the masked region.

The first term in Eq. (3.10), $W\mathcal{B}\mathcal{H}Wf$, describes an image of the ROI reconstructed by use of the measurements that are solely produced from the structures inside the same ROI, as illustrated by the projection profile shown in Figure 3.2. Note that $\mathcal{B}\mathcal{H}Wf$ is the reconstructed image defined in the whole support, in which the area outside the radius r' is not zero but may contain streak artifacts when the number of projection views is not sufficient. However, due to the properties of the back projection operator \mathcal{R}^\dagger , the FBP method ensures that the reconstruction of the ROI of radius r' is independent of that for the masked region. Therefore reconstructing the designated ROI is equivalent to an conventional reconstruction problem that has a smaller FOV of radius r' . If $\Omega = M/(2\pi r')$ holds, it is reasonable to directly apply the argument stated in Section 3.2.2 to establish that this ROI can be reliably reconstructed by use of the FBP algorithm. Mathematically speaking, $W\mathcal{B}\mathcal{H}Wf = Wf$.

The second term of Eq. (3.10), $W\mathcal{B}\mathcal{H}(1-W)f$, namely represents the streak artifacts present in the ROI that is backprojected from the source $(1-W)f$ corresponding to the structures outside the ROI. It can be denoted as an error term ϵ , and will be further discussed it in Section 3.3.2.

In summary, by rewriting Eq. (3.10) it can be concluded that

$$W\hat{f}_{\text{FBP}} = Wf + \epsilon. \quad (3.11)$$

It implies that, for few-view tomographic reconstruction, although the information is not sufficient enough to accurately recover the entire image by use of an un-regularized reconstruction operator, there is still an opportunity to reliably estimate the object within a restricted ROI when ϵ is small.

3.3.2 The recovery of the object's high-frequency contents

Given the imaging operator \mathcal{H} and the data function g , an optimization problem is proposed based on Eq. (3.11) in order to extract certain high-frequency components of f that are usually difficult to retrieve:

$$\begin{aligned} f_1 &= \underset{f}{\operatorname{argmin}} \|f\|^2 \\ s.t. \quad \mathcal{H}f &= (C - 1)g, \end{aligned} \quad (3.12)$$

where the filter $C = \mathcal{H}\mathcal{R}^\dagger C_h$, and C_h is a scaled Hilbert transform operator as specified in Eq. (3.4). Mathematically, one can demonstrate that

$$Wf_1 = Wf_{\text{null}} + \epsilon, \quad (3.13)$$

where the determination of W is guided by the aforesaid rule of Eq. (3.8), and f_{null} denotes the null component of the object in terms of the imaging operator \mathcal{H} . Details regarding this interpretation are provided in Appendix A.

As suggested by the Fourier slice theorem, f_{null} mainly contains high-frequency information that is insufficiently sampled in the Fourier domain. As a consequence, Eq. (3.13) suggests that the recovery of Wf_1 can yield useful high-frequency information regarding the object within the ROI of radius r' , which is generally a challenge for few-view image reconstruction methods.

Note that the solution of Eq. (3.12) also satisfies

$$f_1 = \underset{f}{\operatorname{argmin}} \|\mathcal{H}f - (C - 1)g\|^2, \quad (3.14)$$

when a Landweber-type iterative algorithm is employed starting from a zero initial guess[113].

Remark 1: Since W is non-invertible, it should be noted $\mathcal{H}Wf_{\text{null}} = \mathbf{0}$ is generally not true. Therefore by definition Wf_{null} is not a null-space function of the imaging system, and the recovery of Wf_{null} does not violate linear operator theory.

Remark 2: Under certain conditions, the error term ϵ could be insignificant. This could occur, for example, if the outside-ROI structures are weak in magnitude or sparse in spatial distribution. Also, if the outside-ROI structures corresponds to lower frequencies, ϵ can be negligible. This could be understood by a similar analysis as stated in section 3.2.2, which implies a lower-frequency object could have a larger “artifact-free” zone. Particularly, if the outside-ROI structures have $\Omega \leq M/(2\pi R)$, then they won’t produce any streak artifacts over the entire object support R , and ϵ is consequently zero.

3.4 Subspace-based image reconstruction method

3.4.1 General forms of the discrete imaging model

Many iterative image reconstruction algorithms require a discrete imaging model, and a natural way to obtain this is to discretize the semi-continuous model in Eq. (3.3). When a digital detector is employed, the data function corresponds to an ordered collection of numbers. Since the reconstruction problem is inherently 2D, we will denote the discrete data function as

$$g[k, \phi_i] = g(s, \phi_i)|_{s=k\Delta_d}, \quad (3.15)$$

where k is integer-valued detector element index along the transverse direction, and Δ_d denotes the detector element dimension. Let the vector $\mathbf{g} \in \mathbb{R}^{K \times M}$ denote a lexicographically ordered representation of $g[k, \phi_i]$. The dimension of \mathbf{g} is the product of the number of detector row elements K and the number of view angles M .

In order to obtain a finite-dimensional approximate representation of the object function, a linear N -dimensional approximation of $f(\mathbf{r})$ can be formed as

$$f_a(\mathbf{r}) = \sum_{n=0}^{N-1} \tilde{f}_n \beta_n(\mathbf{r}), \quad (3.16)$$

where the subscript a indicates that $f_a(\mathbf{r})$ is an approximation of $f(\mathbf{r})$, $\{\beta_n(\mathbf{r})\}$ are a set of expansion functions, and $\{\tilde{f}_n\}$ are the corresponding expansion coefficients. Let \mathbf{f} be a $N \times 1$ vector of expansion coefficients that has an n -th element given by \tilde{f}_n . Rather than the conventional pixel basis functions, the Kaiser-Bessel window expansion functions[93, 85] were employed in this study. This choice is shown to have the attractive feature that the

derivative and Radon transform operators with respect to the expansion functions can be computed analytically, thereby circumventing the need to numerically approximate it.

With the defined discrete data function and object function, a system matrix \mathbf{H} employing the generalized Kaiser-Bessel window functions can be constructed[175] that approximately satisfies

$$\mathbf{g} = \mathbf{H}\mathbf{f}. \quad (3.17)$$

This represents a discrete imaging model for D-XPCT that can be used with iterative image reconstruction algorithms for estimation of \mathbf{f} from knowledge of \mathbf{g} and \mathbf{H} . From the estimated \mathbf{f} , the object function estimate - the sought after image - can be obtained by use of Eq. (3.16).

3.4.2 Proposed iterative reconstruction method

Equation (3.11) implies that, for a given object, the FBP algorithm can produce sharp and accurate images within a ROI whose radius is dependent on the number of tomographic views. However, the FBP algorithm usually does not effectively mitigate noise. Also, it produces severe streak artifacts outside the ROI when the number of views is insufficient. Meanwhile, the conventional TV-regularized iterative algorithm can effectively suppress noises and artifacts, but it also brings the risk of removing desired subtle structures.

In order to synergically combine the two reconstruction methods, we propose a subspace-based (SuB) reconstruction strategy, and reconstruct the images in a two-step, iterative approach that can be more robust against the noise.

Similar to the decomposition step described in the previous section, the reconstructed image \mathbf{f} is denoted as the sum of two images \mathbf{f}_1 and \mathbf{f}_2 by

$$\mathbf{f} = W\mathbf{f}_1 + \mathbf{f}_2, \quad (3.18)$$

where \mathbf{f}_1 and \mathbf{f}_2 can be computed respectively via a two-step approach as shown in Eq. (3.19) and (3.20). We first compute \mathbf{f}_1 by solving

$$\mathbf{f}_1 = \underset{\mathbf{f}}{\operatorname{argmin}} \|\mathbf{H}\mathbf{f} - (C - 1)\mathbf{g}\|^2, \quad (3.19)$$

with a gradient-descent algorithm and a zero initial guess. Subsequently, the object component $W\mathbf{f}_1$ is fixed and \mathbf{f}_2 is estimated as:

$$\mathbf{f}_2 = \underset{\mathbf{f}}{\operatorname{argmin}} \|\mathbf{H}(W\mathbf{f}_1 + \mathbf{f}) - \mathbf{g}\|^2 + \lambda\|\mathbf{f}\|_{TV}, \quad (3.20)$$

where $\|\cdot\|_{TV}$ indicates the total-variation semi norm[153].

As suggested in section 3.3.2, the first sub-problem [Eq. (3.19)] produces an estimate of $W\mathbf{f}_1$ that mainly contains the high-frequency contents of the object inside the designated ROI. In the second sub-problem [Eq. (3.20)], a TV-penalized least square (PLS-TV) estimator is employed for estimating \mathbf{f}_2 . Note that by subtracting the contribution of high-frequency component from the measurements, \mathbf{f}_2 will mainly contain low-frequency contents, which is considered smoother and therefore more suitable for the application of TV regularization.

Therefore, the proposed sub-space image reconstruction method, referred to as the Sub-PLS-TV method, includes the following potential benefits:

- The high-frequency details within the designated ROI can be stably recovered from measured few-view data.
- The global TV regularization is still employed for the purpose of suppressing noise and streak artifacts over the entire object domain.
- Since the two subspaces are naturally constrained in the second sub-problem, in the reconstructed image the transitions at the ROI boundaries are smooth.

Below, the proposed Sub-PLS-TV method, the FBP method, and the conventional PLS-TV method will be compared through numerical studies. The PLS-TV method corresponds to iteratively solving the following optimization problem

$$\hat{\mathbf{f}}_{\text{PLS}} = \underset{\mathbf{f}}{\operatorname{argmin}} \|\mathbf{H}\mathbf{f} - \mathbf{g}\|^2 + \lambda \|\mathbf{f}\|_{\text{TV}}, \quad (3.21)$$

which has been widely used for few-view CT image reconstruction[153]. A modern iterative reconstruction algorithm based on the FISTA acceleration framework[14] is employed for the two iterative methods.

3.5 Results

3.5.1 Computer-simulation studies

Computer-simulation studies were conducted to demonstrate and validate the proposed Sub-PLS-TV image reconstruction method. A 1024×1024 numerical phantom was generated, shown in Fig. 4.1(a), which contained a lumpy background with slowly varying magnitude

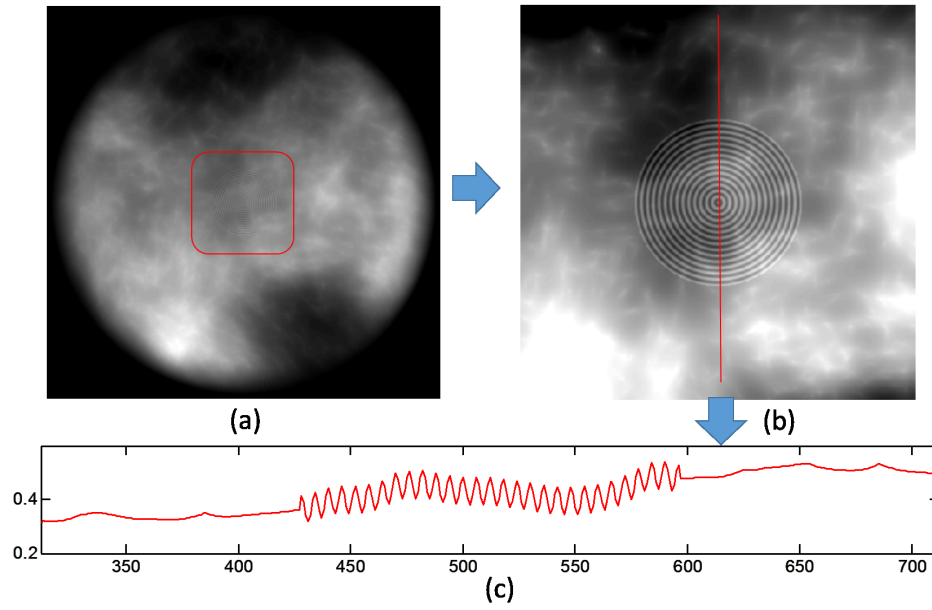


Figure 3.3: (a) The complete phantom. (b) A zoomed-in region of the phantom with adjusted gray-value window. The dashed circle indicates the designated ROI where the capability of reconstructing high-frequency structures is expected. (c) The extracted profile of the phantom across the center.

and a disk with fast varying ripple fluctuations. Differential phase-contrast measurement data corresponding to 90 tomographic views evenly distributed over 180 degrees were generated by projecting the phantom using the system matrix \mathbf{H} introduced in Section 3.4.1. Consequently, the system matrix used for data generation exactly matches the one used for reconstruction in this simulation study. In order to mitigate the inverse crime, here 5% Gaussian noise was added in the simulated data. Note that the model mismatch will be inherently present in the experimental study that is discussed in the next section.

In the phantom, the random background was generated based on the recommended parameters for mimicking the statistical texture of mammographic images[17]. The rippled disk represents the high-frequency details that normally bring challenges for few-view image reconstruction. For simplicity, the ripple was designed to have a constant spatial frequency at 6 pixels/cycle which could be reasonably considered as the phantom’s upper frequency limit. Therefore, based on Eq. (3.6), a ROI could be designated with the radius $r = M/(2\pi\Omega) = 86$ pixels in which the high frequency structures are expected to be well recovered. In this study, the radius of the rippled disk was also made as large as r for the purpose of demonstrating the maximum ability of reconstructing high-frequency structures.

We compared the performances of three methods: FBP, PLS-TV, and the proposed SuB-PLS-TV method. For both iterative methods, the regularization parameter λ was swept over a wide range to show the overall tendency of image quality. A series of typical reconstructed images corresponding to progressively increasing TV parameters (i.e. $1e^{-1}$, $1e^{-2}$, $1e^{-3}$ and $1e^{-4}$) are shown in Figs. 3.4 and 3.5, for the designated ROI region and an outside-ROI region, respectively.

In the designated ROI (Fig. 3.4), the conventional PLS-TV method was ineffective at recovering the high-frequency ripples of the disk, no matter how we tuned the regularization

parameter. TV regularization smooths the noisy background but meanwhile suppresses high-frequency details. As opposed to this, the proposed SuB-PLS-TV method selectively applies the TV regularization to the low-frequency subspace, and is thus able to preserve the high-contrast ripples within the ROI. Also, the proposed method still gains the benefits of noise suppression by using TV regularization, which is a significant advantage over the analytical FBP method. Since the lumpy background contains mostly low-frequency contents, there are no discernible streak artifacts shown in the designated ROI, suggesting that the error term in Eq. (3.13) is negligible.

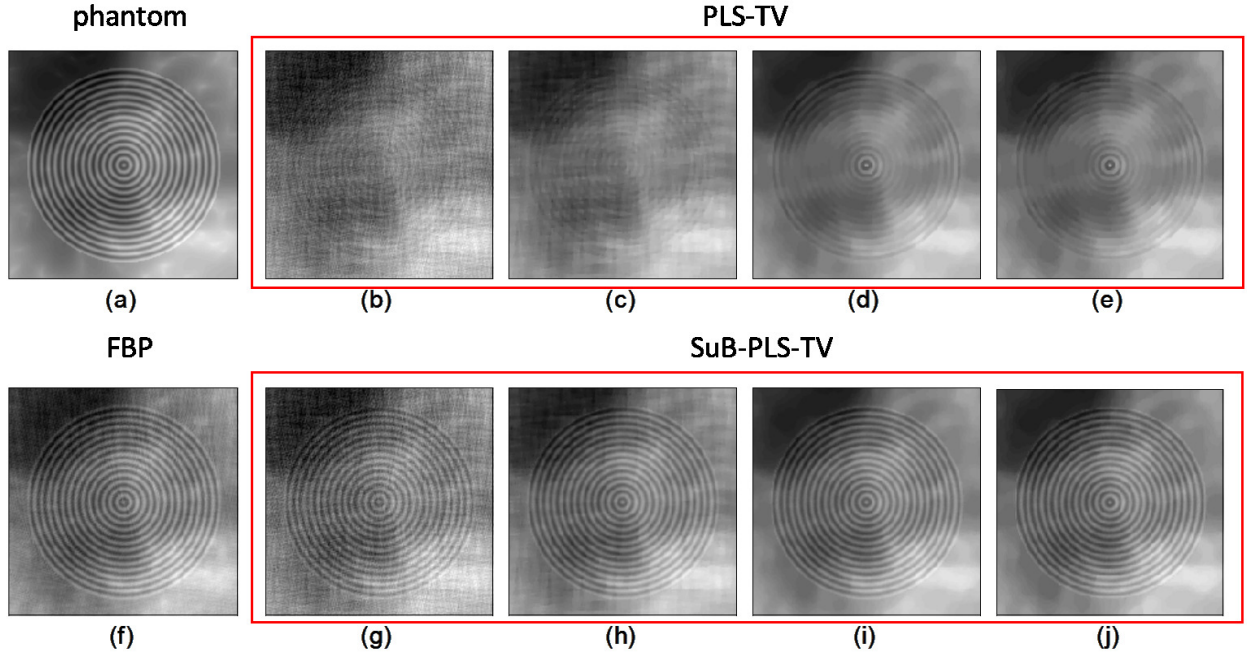


Figure 3.4: The comparison of reconstructed images inside the designated ROI. (a) Phantom; (b)-(e) The PLS-TV method with increasing TV regularization parameter values; (f) FBP method; (g)-(j) The proposed SuB-PLS-TV method with progressively increasing TV regularization parameter values.

In an outside-ROI region (Fig. 3.5), where streak artifacts occur in the image reconstructed by the FBP method, the SuB-PLS-TV method still outperforms the alternative iterative

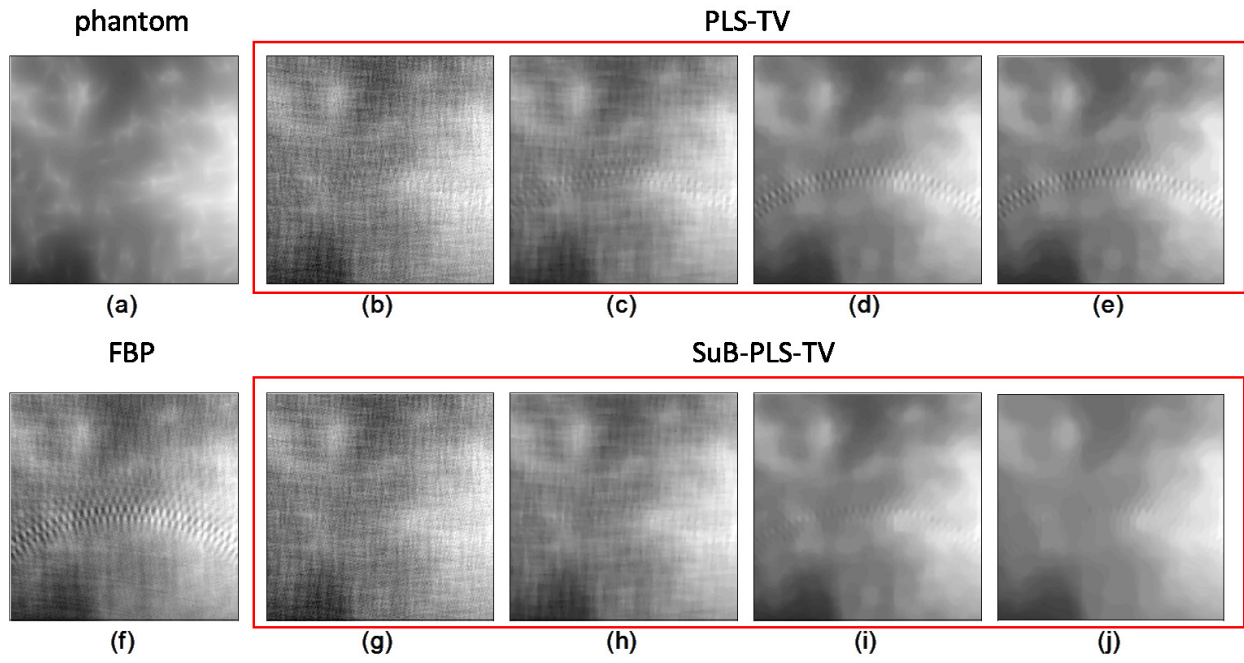


Figure 3.5: The comparison of reconstructed images outside the designated ROI. (a) Phantom; (b)-(e) The PLS-TV reconstruction results with increasing TV regularization parameter values; (f) FBP method; (g)-(j) The proposed SuB-PLS-TV reconstruction results with progressively increasing TV regularization parameter values.

method in terms of artifact suppression. This is credited to the novel cost function design of the sub-problem in Eq. (3.20). The subtraction of the contribution of $W\mathbf{f}_1$ from the measurement data leads to more accurate estimation of \mathbf{f}_2 representing the accurate low-frequency structures over the entire image.

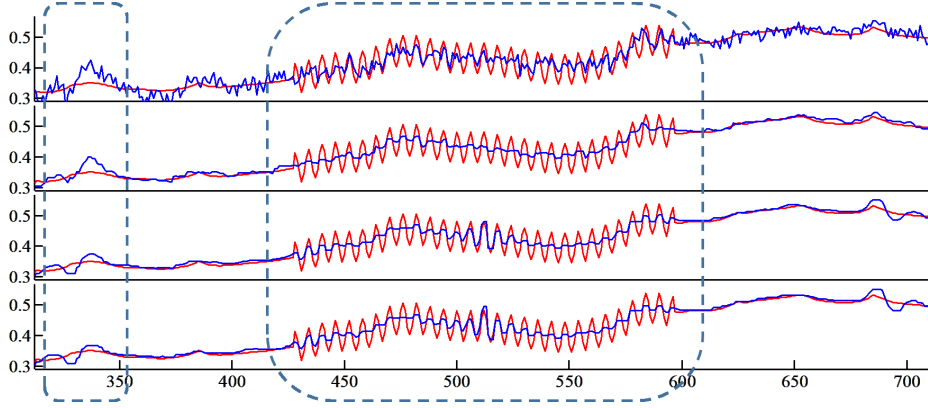


Figure 3.6: The profiles extracted from the conventional PLS-TV reconstructed images with increasing regularization parameter values (blue) and the corresponding ground truth (red).

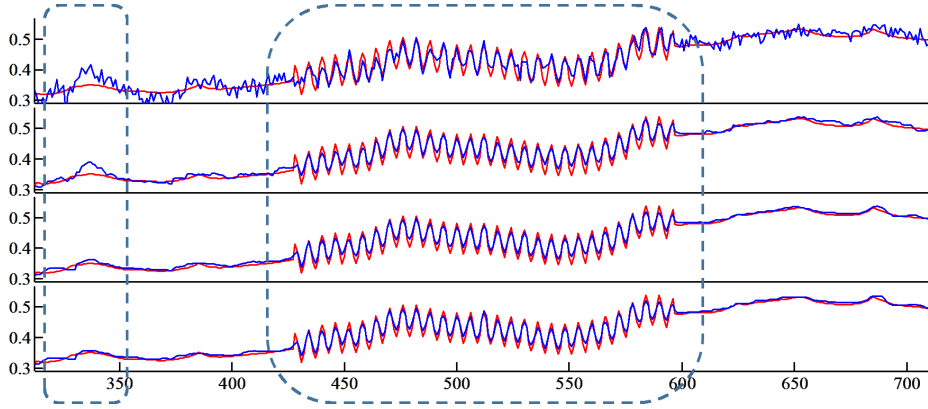


Figure 3.7: The profiles extracted from the SuB-PLS-TV reconstructed images with increasing regularization parameter values (blue) and the corresponding ground truth (red).

Line profiles were extracted from the reconstructed images and superimposed on the corresponding profiles through the true phantom. The profile through the center, as depicted in Fig. 4.1(a), crosses the designated ROI and an outside-ROI region where the streak artifacts

would occur. Figure 3.6 shows a series of profiles corresponding to the PLS-TV reconstructed images with increasing TV regularization parameters. Figure 3.7 shows a series of profiles corresponding to the SuB-PLS-TV results with increasing TV regularization parameters. Profiles through the reconstructed images for the inside and outside ROI are highlighted by dashed squares. Again, the SuB-PLS-TV method yields a reconstruction result that is visually more consistent with the ground truth. By tuning the regularization parameter, it performs better than the conventional PLS-TV method in terms of balancing the recovery of high-frequency ripples and the suppression of background noise and/or streak artifacts.

3.5.2 Experimental studies

The proposed reconstruction method was also validated by use of an experimental D-XPCT data set produced by a benchtop edge-illumination X-ray phase contrast CT system built at University College London[120, 63]. The sample was a dung beetle. The complete tomographic data set contained 720 views with an angular spacing of 0.5° , from which a reference image could be generated via the FBP algorithm, which is shown in Fig 3.8. Detailed features of the object are visible in the zoomed-in region.

For the few-view image reconstruction studies, a subset of 120 uniformly spaced views over a 180° span were extracted from the complete data set. This reduction in the number of measurements can reduce the acquisition times by one-sixth, resulting in a total time savings of an hour. Assuming the object's maximum frequency of interest is approximately 10 mm^{-1} , a central ROI with the radius of 2 mm (150 pixels) can be designated, where a reliable reconstruction of high-frequency structures is expected. The designated ROI is labeled as

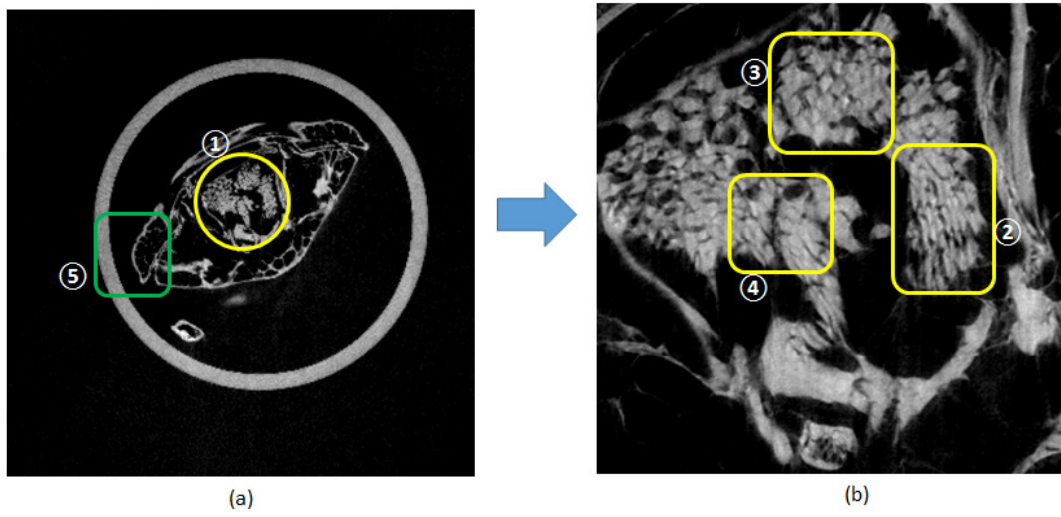


Figure 3.8: (a) The reference image of the object produced by use of the FBP algorithm and the complete data. (b) A zoomed-in region of the designated ROI.

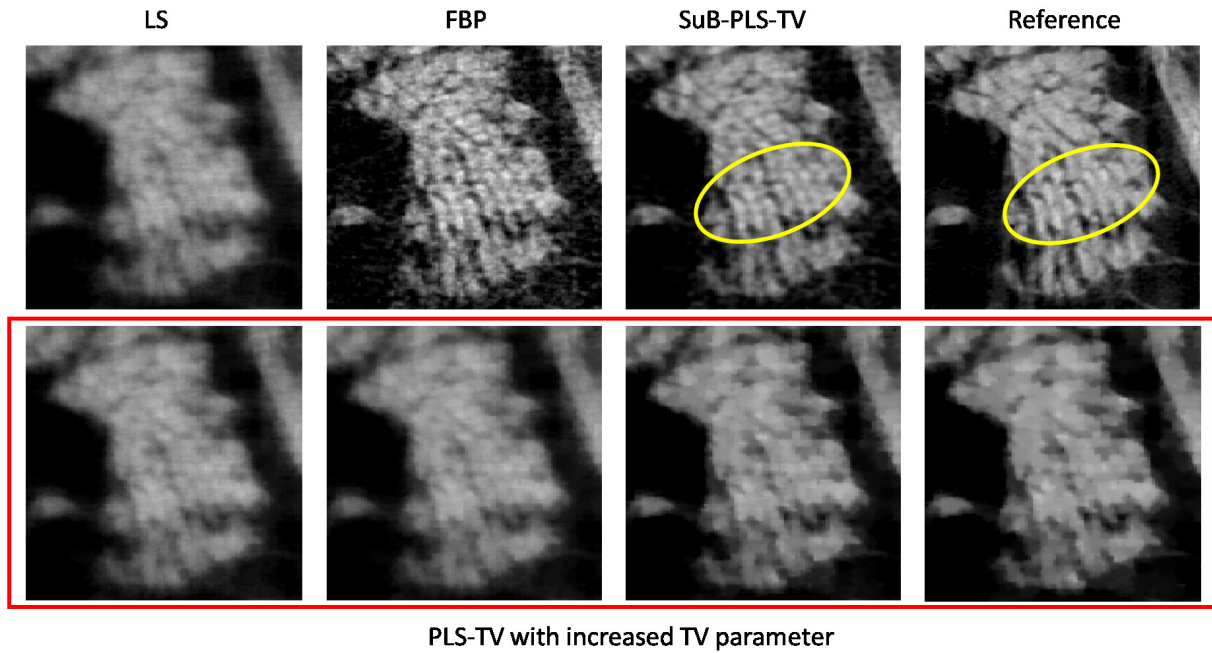


Figure 3.9: The comparison of the reconstructed ROI ② by use of FBP, PLS-TV and SuB-PLS-TV methods.

region ① in Fig 3.8. Three smaller windows ②-④ inside this ROI, as well as an outside-ROI region ⑤, will be inspected for evaluating the few-view reconstruction performances.

Figure 3.9 shows the reconstructed ROI images corresponding to the region ② labeled in Fig 3.8. The LS image indicates the least-square estimate of the object (i.e. Eq. (3.21) with $\lambda = 0$). It exhibits blurring appearance due to the nature of few-view data acquisition and the consequent insufficient sampling of high frequency contents in the Fourier domain. The image reconstructed by use of the FBP method preserves high-frequency details, but also contains a considerable amount of noise. In the bottom row, a series of images reconstructed by the PLS-TV method are shown with a wide range of increasing regularization parameter values that are listed in Table 3.1. As demonstrated before, they either appear blurred or oversmoothed. Instead, the proposed SuB-PLS-TV method provides promising results. The plotted ellipse highlights the structures that bear a close resemblance with the reference image while the conventional PLS-TV images do not have. In this study, the choice of the regularization parameter value for the presented SuB-PLS-TV image is fixed the same as the one for the third PLS-TV image for all Figs. (3.9)-(3.12).

Similar observations resulted when examining the other two ROIs labeled as region ③ and ④. The reconstructed images and the comparison between different methods are shown in Figs 3.10 and 3.11. Again, all the images reconstructed by use of the PLS-TV method do not show the trend of resolving those fine structures, but the proposed SuB-PLS-TV method could produce a noise-suppressed and more natural looking image that is very close to the reference.

Figure 3.12 shows a typical region ⑤ outside the designated central ROI ①. In this case, the SuB-LS-TV image gives a cleaner background compared with the FBP algorithm. It

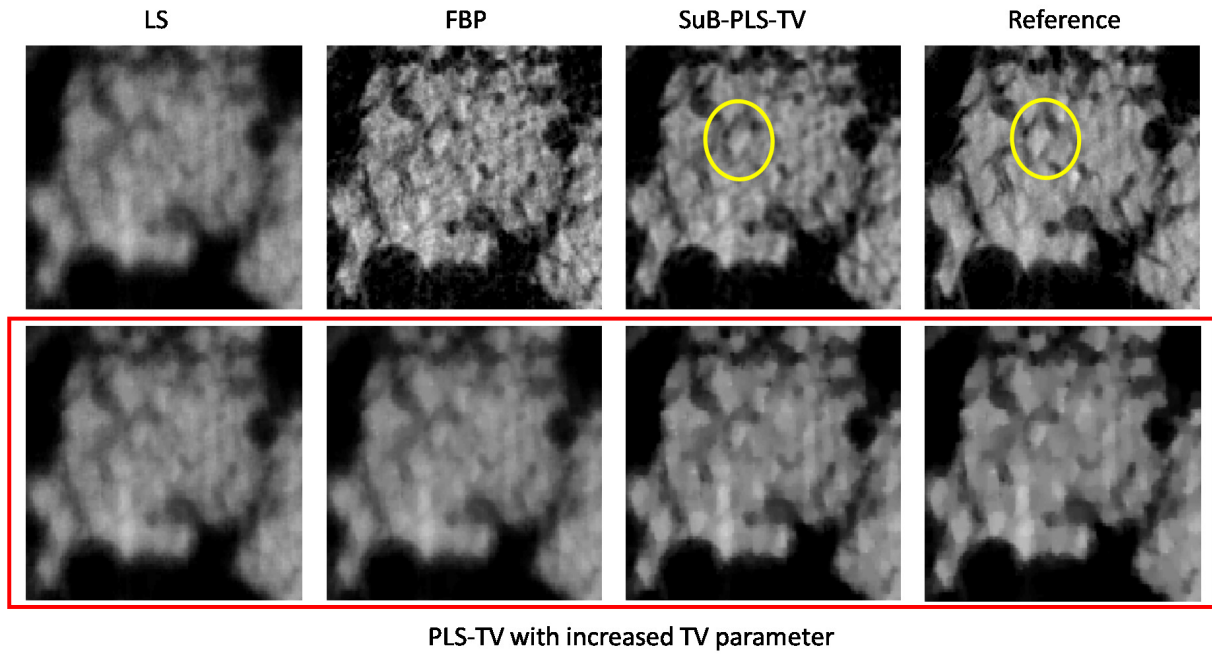


Figure 3.10: The comparison of the reconstructed ROI ③ by use of FBP, PLS-TV and SuB-PLS-TV methods.

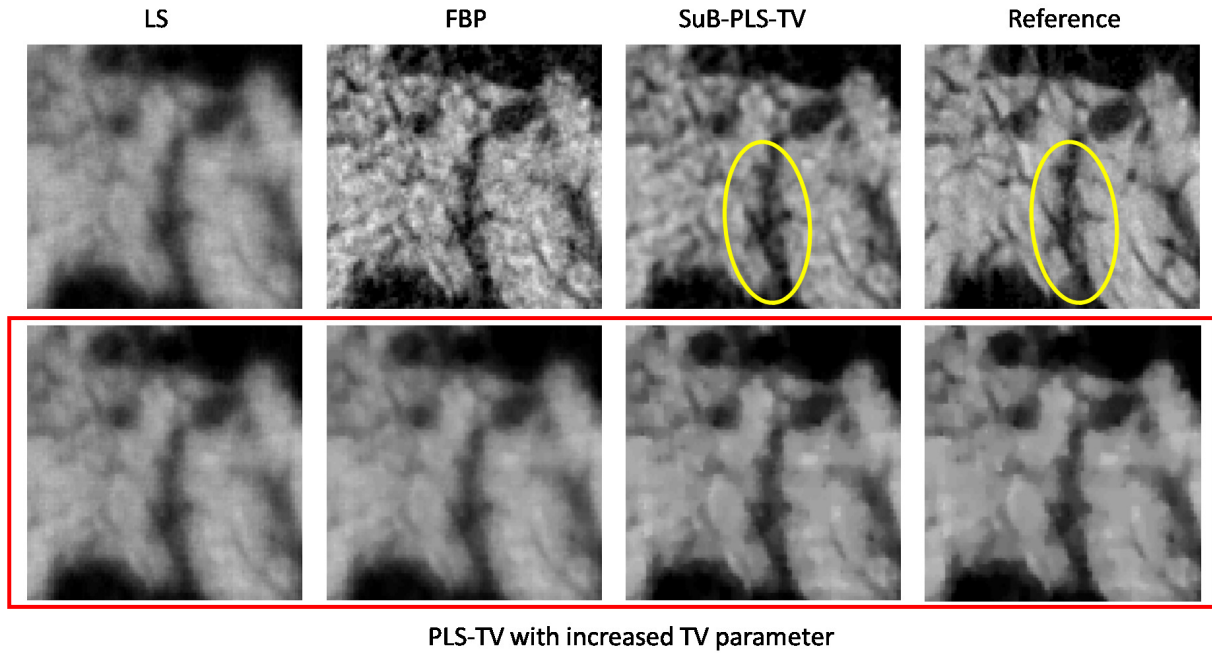


Figure 3.11: The comparison of the reconstructed ROI ④ by use of FBP, PLS-TV and SuB-PLS-TV methods.

also visually outperforms the PLS-TV image in terms of restoring the structures located far from the center as indicated in the plotted ellipse.

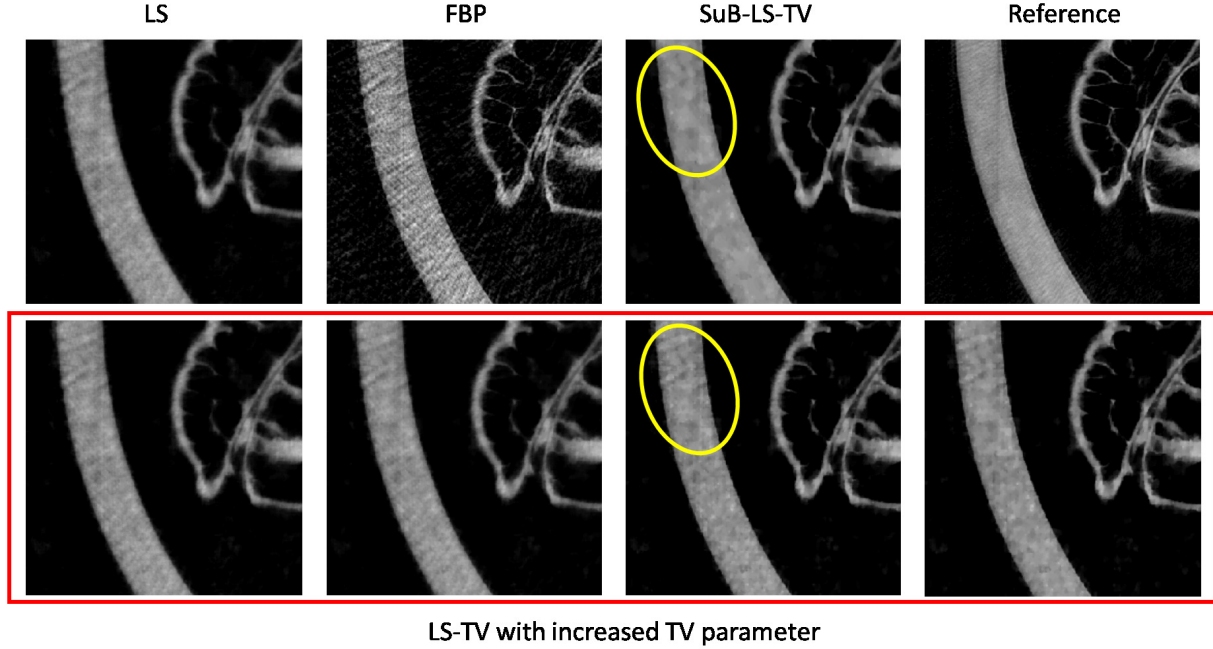


Figure 3.12: The comparison of the reconstructed region ⑤ outside the designated ROI by use of FBP, PLS-TV and SuB-PLS-TV methods.

All the images in Figs. (3.9)-(3.12) reconstructed by use of the PLS-TV, FBP and SuB-PLS-TV methods were quantitatively evaluated in terms of Mean Square Error (MSE) and Structure Similarity Index (SSIM), as shown in Table 3.1. The corresponding reference images were served as the standard when computing the figure of merits. In all listed regions, the SuB-PLS-TV method gives the lowest MSE and the highest SSIM, which proves the stable and reliable reconstruction performance compared with the other methods.

Table 3.1: Quantitative evaluation of the reconstructed images in MSE and SSIM

		PLS-TV w/ increasing TV parameter				FBP	SuB-PLS-TV
TV parameter value		$1e^{-8}$	$2e^{-8}$	$3e^{-8}$	$4e^{-8}$	-	$3e^{-8}$
Region ②	MSE	5.030	4.972	5.029	4.991	4.771	4.292
	SSIM	0.667	0.671	0.675	0.675	0.683	0.754
Region ③	MSE	5.296	5.229	4.975	4.924	4.529	4.185
	SSIM	0.685	0.690	0.708	0.706	0.768	0.777
Region ④	MSE	5.082	5.021	4.880	4.818	4.728	4.209
	SSIM	0.681	0.687	0.700	0.699	0.728	0.774
Region ⑤	MSE	4.401	4.212	4.110	4.085	5.480	3.625
	SSIM	0.560	0.579	0.588	0.588	0.450	0.623

3.6 Conclusion

A new subspace-based reconstruction strategy was proposed and investigated for use in few-view D-XPCT image reconstruction. It possesses the attractive features that subtle structures can be accurately reconstructed within a designated ROI, while the entire FOV can be effectively regularized to mitigate noise and streaking artifacts. More specifically, the object is split into two components that represent the high-frequency and low-frequency subspaces, respectively. The resulting two-step iterative method is expected to mitigate the high-frequency information loss caused by data incompleteness and produce better images than those produced by use of a conventional PLS-TV estimator. The proposed SuB-PLS-TV method was validated by a computer-simulated data set as well as an experimental data set acquired from an edge-illumination XPCT scanner.

The proposed reconstruction method can be applied with all XPCI imaging modalities that produce differential phase-contrast data. It can also be readily extended to conventional CT scenarios by use of a modified filter $C = \mathcal{R}\mathcal{R}^\dagger C_0$ in Eq. (3.12), where C_0 is the ramp

filter in this case. In practical applications, the prior information regarding the maximum frequency of the sample may not be known, but Ω can be preset based on the maximum frequency of interest in terms of a specific imaging purpose. The projection data might need to be preprocessed with a low-pass filter according to the cut-off frequency Ω . Multiple trials for determining an ideal Ω may be necessary before the resulting image quality is fully optimized. Note that there is always a trade off between the frequency setting Ω and the size of the recoverable ROI.

It is worthy noting that the error term ϵ presented in Eq. (3.13) might affect the reconstructed images. When ϵ is not small, generally the reconstructed ROI is still sharp but the recovery of the high-frequency structures is at the cost of the appearance of streak artifacts. However, it should be noted that in the medical imaging field the task-based image assessment is widely promoted[12]. In some imaging applications, resolution-enhanced images are useful for diagnostic purposes even though the artifacts are sometimes present, and the proposed strategy is able to provide such a solution.

Chapter 4

A total-projection-length constrained method for stabilized quantitative projection-based dual-energy material decomposition

Dual-energy X-ray imaging exploits the energy-dependent X-ray attenuation properties of materials to identify and characterize the material composition of structures in X-ray images acquired using high and low energy beams. Dual-energy computed tomography (DECT) has been widely investigated over the last decade and is available in several commercialized imaging systems. However, there is still a lack of reliable and valid methods for projection-based material decomposition, which remains a bottleneck for the development of dual-energy computed radiography (DECR). One main difficulty is the extreme sensitivity to data noise, as conventional projection-based decomposition relies on solving high-order polynomial equations. In this work, we claim that a constraint of total projection length can effectively stabilize the two-material decomposition process. Also, two feasible “water-bath”

and “scout-scan” ideas are proposed in order to practically obtain the constraint. Results from numerical simulations demonstrate that the constrained method is capable of quantitatively accurate material decomposition and presents robustness against data noise, showing promising potentials of DECR in clinical applications for example mammography where the size of calcification is of interest.

4.1 Introduction

Dual-energy X-ray imaging is a technique in which two (or two sets of) projections using two different incident beam spectra are acquired of the same object. X-ray attenuation for the range of energies employed in diagnostic radiography consists of contributions from photoelectric absorption and Compton scattering. The probability of Compton interactions is relatively independent of energy and material composition. However this is not the case for the photoelectric effect for which the interaction cross section is approximately proportional to Z^3/E^3 , where E is the x-ray energy and Z is the average atomic number of the material. Two X-ray projections of an object, one acquired with a high energy beam and the other with a low energy beam, will have differences in detected intensities between the two radiographs which depend on the composition of the object. For an object composed of two materials, these intensity changes can be exploited to form two basis material images[5, 23]. This procedure is often referred to as material decomposition. The decomposed information can facilitate material segmentation or identification of an abnormality[131, 159].

Dual-energy X-ray imaging modalities can be generally categorized into two classes: dual-energy computed tomography (DECT)[112, 159] and dual-energy computed radiography

(DECR)[24, 121]. The former acquires tomographic data sets and performs the decomposition in the reconstructed image domain, which is referred to as the image-based method. The image-based decomposition requires beam hardening corrections for reconstructed images or advanced reconstruction algorithms that can handle polychromatic spectrum, and then the material type can be recognized by examining reconstructed pixel's CT numbers from high- and low-energy exposures. This method has gradually become popular during the last decade, and there have already been a number of commercialized DECT systems developed and widely employed in various clinical applications[41, 147, 162]. On the other hand, DECR, which performs material decomposition in the projection domain, has not yet found widespread implementation in medical imaging applications. Though projection-based decomposition is essentially free of the beam hardening problem[131], DECR requires the strict registration of the two projections, and seeks for the solution of an ill-posed inverse problem which is sensitive to noise[11, 22].

In DECR chest imaging applications, an image subtraction method was employed to provide a qualitative material decomposition. A linear weighted subtraction of the two projections was used to produce a bone-selective image, whereas another subtraction with different weights was used to produce a soft tissue-selective image[67, 137]. This subtraction approach has also been applied to dual-energy X-ray absorptiometry to estimate a body composition in terms of fat and bone mineral[89]. However, the image subtraction method is valid only for monochromatic spectra in theory. When a bench-top X-ray tube is used, the simple linear subtraction is actually suboptimal in the sense that it fails to provide accurate quantitative information regarding the composition. A more rigorous decomposition method should take polychromatic spectra into account. Suppose an object is composed of only bone and soft tissue, with corresponding projected thicknesses (or line integrals) l_b and l_s along the X-ray beam direction, respectively. For two energy spectra $S_H(E)$ and $S_L(E)$, the physical model

that describes the dual-energy imaging process is given by[159]

$$\begin{aligned} I_H/I_{H0} &= \int S_H(E) \exp[-l_b \mu_b(E) - l_s \mu_s(E)] dE \\ I_L/I_{L0} &= \int S_L(E) \exp[-l_b \mu_b(E) - l_s \mu_s(E)] dE, \end{aligned} \tag{4.1}$$

where μ_b and μ_s denote the linear attenuation coefficients of bone and soft tissue, I_H and I_L are the high- and low-energy intensity measurements, and I_{H0} and I_{L0} are the corresponding flat field images.

Because Eq. (4.1) contains transcendental functions, it brings difficulties in mathematically solving the decomposition problem for closed-form solutions. A conventional strategy is to use high-order polynomials to approximate the dual-energy imaging process described in Eq. (4.1)[23, 131]. Once the approximating functions are constructed via a calibration step, they are involved in an inverse problem to estimate the individual material's line integral of an object, as long as the imaging conditions (e.g. spectra) remain the same. Although there have been a number of methods proposed under this framework, either the direct fit of the dual energy equations [5], or the approximation of its inverse map [23, 80], they all have been reported to be unstable and sensitive to photon noise. The main problem lies in the high non-linearity of the dual-energy imaging model when polychromatic spectra are used [35].

To mitigate this issue, we propose to introduce a constraint of total projection length, which can effectively stabilize the conventional projection-based material decomposition. We also develop two feasible “water-bath” and “scout-scan” ideas that can be used to practically implement the desired constraint. Numerical studies show that our method is capable of accurate two-material decomposition and shows robustness against data noise.

4.2 Methods

4.2.1 Calibration method

In biomedical applications such as chest imaging or mammography, it is difficult to obtain calibration data using biological materials due to their irregular shapes and structural heterogeneity. It is therefore common to choose aluminum (Al), a bone-like material, and plexiglas (Lucite) (Pl), a tissue-like material, as basis materials. Calibration phantoms made from Al and Pl can be fabricated to high precision and their X-ray attenuation properties are well-defined. Therefore, we presume the attenuation of any biomedically relevant objects to be equivalent to the combined attenuation of Al and Pl. It is important to note that Al does not strictly represent bone nor does Pl represent soft tissue.

Figure 4.1(b) displays an example of a typical setup for acquiring calibration data from Al and Pl wedges. More details will be introduced in Sec 4.3. Basically, two projections of the calibration phantom are acquired, one with a high-energy beam and one with a low-energy beam. We denote a pixel's measured log signals as $f = \log(I_H/I_{H0})$ and $g = \log(I_L/I_{L0})$, for high- and low-energy exposures, respectively. The detected signals (f, g) at a given pixel correspond to a thickness pair of two basis materials, denoted as (p, q) .

In contrast to the conventional polynomial approximation, the conic rational equation is a recommended model for approximating the polychromatic imaging process described in Eq. (4.1). The new model claims the advantages of better smoothness, monotonicity and asymptotic linearity[29, 35]. We therefore construct the following two rational functions

$F(p, q)$ and $G(p, q)$:

$$\begin{aligned} F(p, q) &= \frac{a_0 + a_1p + a_2q + a_3p^2 + a_4pq + a_5q^2}{1 + a_6p + a_7q} \\ G(p, q) &= \frac{b_0 + b_1p + b_2q + b_3p^2 + b_4pq + b_5q^2}{1 + b_6p + b_7q}, \end{aligned} \tag{4.2}$$

where the variables p and q are the projected thicknesses (or line integrals) of the two basis materials, the corresponding function values F and G are the computed log signals under high- and low-energy spectra. By use of calibration data, one can estimate the coefficients $\{a_i\}$ and $\{b_i\}$ by fitting Eq. (4.2) from measured signals (f, g) at known combinations of (p, q) . In this work, the weighted least squares $\sum_n \frac{(F_n - f_n)^2}{\sigma_{f_n}^2}$ is minimized iteratively via the Levenberg-Marquardt algorithms[107] to obtain $\{a_i\}$, where n is the calibration pixel index and the signal variance $\sigma_{f_n}^2$ is used as weights allowing for the noise issue. For Poisson noise model, $\sigma_{f_n}^2$ is related to the expected values of photon numbers received on the detector element. Similar steps can be taken to obtain $\{b_i\}$.

Note that, as opposed to Eq. (4.1), the approximating functions $F(p, q)$ and $G(p, q)$ do not explicitly involve the integral over the spectrum when computing the signal intensities. The effects of polychromatic spectra have actually been incorporated in the approximating functions by estimating the coefficients from calibration data. Therefore, this method claims the advantage of eliminating the requirement for measuring the two source spectra employed in dual-energy imaging.

4.2.2 Decomposition method

In most cases, the object to be imaged does not consist of the same materials as those used to make the calibration phantom. In order to generally apply the approximation functions,

any objects to be decomposed should be first converted into the basis material combinations with equivalent total attenuation. For example, suppose a biological sample consists of bone (μ_b) and soft tissue (μ_s); the calibration phantom is made of aluminum (μ_{Al}) and plastic (μ_{Pl}). We can define attenuation properties of bone and soft tissue as a linear combination of the properties of the basis materials:

$$\begin{aligned}\mu_b(E) &= \alpha_{11}\mu_{Al}(E) + \alpha_{12}\mu_{Pl}(E) \\ \mu_s(E) &= \alpha_{21}\mu_{Al}(E) + \alpha_{22}\mu_{Pl}(E),\end{aligned}\tag{4.3}$$

where the coefficients $\{\alpha_{ij}\}$ are unique and energy-independent[91]. The determination of $\{\alpha_{ij}\}$ is described in Appendix B.

For any detector pixel, we denote the corresponding projected bone length as l_b , and the projected soft tissue length as l_s . By multiplying l_b at the both sides of Eq. (4.3), it implies that a bone of length l_b , is equivalent to aluminum of length $\alpha_{11}l_b$ plus plastic of length $\alpha_{12}l_b$, in terms of X-ray attenuation effect. Similarly, soft tissue of length l_s , is equivalent to aluminum of length $\alpha_{21}l_s$ plus plastic of length $\alpha_{22}l_s$. As a result, the total attenuation of bone and soft tissue along the line integral can be equivalently converted to basis materials (Al and Pl) with thickness pair (p, q)

$$\begin{aligned}p &= \alpha_{11}l_b + \alpha_{21}l_s \\ q &= \alpha_{12}l_b + \alpha_{22}l_s.\end{aligned}\tag{4.4}$$

By substituting Eq. (4.4) into (4.2), one can use the two-dimensional Newton-Raphson method to iteratively solve for l_b and l_s . Note that the exact solutions may not exist.

For the ease of interpretation, an equivalent, optimization-based problem[29] is proposed:

$$(l_b, l_s) = \underset{l_b, l_s}{\operatorname{argmin}} w_H \|f - F(p, q)\|^2 + w_L \|g - G(p, q)\|^2. \quad (4.5)$$

The objective function value would vanish if the exact solutions for Eq. (4.2) exist, otherwise the obtained (l_b, l_s) minimizes the divergence from the measured data in the sense of weighted least squares. Ideally, the weights w_H and w_L are the reciprocals of the signal variance of f and g , respectively. Given the quadratic approximation of the Poisson log-likelihood function[18], the weights can be practically set as the number of photon counts detected at the specific pixel for both high- and low-energy exposures. This weighting makes sense because the photon counts reduce the variance of measured transmission projection and therefore give more weight to the item whose noise is less.

4.2.3 The total-projection-length constraint

Due to the inherent high-order polynomial nature of Eq. (4.2), noise in measured signal f or g may induce either a small change in the p estimate (heavy material) or possibly a large change in the q estimate (light material). In another word, the inverse problem is ill-posed. Therefore, the decomposed l_s value is more easily corrupted by noise and there has been reported over 200% approximation error when the conventional method was applied to the dual energy CT scanner[181]. Since there are two unknowns to be estimated from exactly two measurements, the solution prescribed by Eq. (4.5) is anticipated to be susceptible to noise and numerically unstable.

To order to circumvent this problem, the solutions may have to be regularized by additional conditions or constraints. A straightforward constrained decomposition method is to enforce

$l_b \geq 0$ and $l_s \geq 0$ which is easy to implement and physically meaningful[181]. However, the effects of this positivity constraint are still far from ideal. In this study, we demonstrate that a more powerful total-projection-length constraint can significantly alleviate the noise sensitivity. If the prior knowledge of $l_b + l_s$ corresponding to each detector pixel is known, the constrained version of Eq. (4.6) can lead to an accurate solution, eliminating the estimates that drastically deviate from the ground truth:

$$\begin{aligned} (l_b, l_s) = \operatorname{argmin}_{l_b, l_s} & \|f - F(p, q)\|^2 + \|g - G(p, q)\|^2 \\ \text{s.t.} \quad & l_b + l_s = L \end{aligned} \tag{4.6}$$

where the relationship between (l_b, l_s) and (p, q) are the same as in Eq. (4.4).

4.3 Descriptions of numerical simulations

Figure 4.1(a) displays a 2D numerical test phantom designed for the simulation studies, which is a breast-shaped semi-ellipse (soft tissue) with three small spheres (calcifications) buried inside. The radius of each calcified sphere is $r=2$ mm, 1.5 mm and 1 mm, respectively. The total size of the breast phantom is 10 cm \times 4 cm. The X-ray beams propagate along the direction as the arrows indicate, and the transmission dual-energy projections will be recorded with respect to this orientation. The aim of the numerical studies is to demonstrate the ability and accuracy of the proposed decomposition method to quantitatively estimate the sizes of buried calcifications, which is expected to broaden the applications of the current DECR technique that was conventionally limited for qualitative diagnosis uses only.

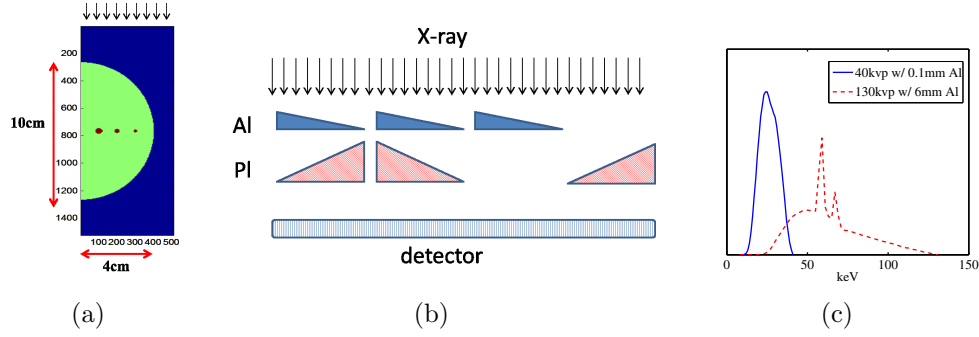


Figure 4.1: (a) The numerical breast phantom. (b) A schematic view of the arrangement of calibration phantoms. (c) The two spectra employed in the numerical studies.

In the calibration step, we generated a few of wedge-shaped calibration phantoms made of two basis materials, aluminum (Al) and plexiglas (Pl), positioned as Fig. 4.1(b) shows. The maximum thickness of the Al wedge along the X-ray beam direction is 2 cm, and the maximum thickness of the Pl wedge along the X-ray beam direction is 20 cm. The purpose for this arrangement is to generate different combinations of the two thicknesses. We chose 24 calibration points that were evenly distributed along the x-ray wavefront, the number of which is much smaller than other calibration methods that have been reported[35]. The attenuation properties of the biological materials (breast tissue and calcification) and the basis materials (Al and Pl) were computed from the NIST physical reference data library [1].

Both for the calibration and breast phantoms, we simulated the dual-energy projection data with two incident polychromatic x-ray spectra (tungsten anode). The spectra were generated from an on-line tool for spectrum simulation[2]. The high-energy spectrum (130kVp with 6mm aluminum filter) and the low-energy spectrum (40kVp with 0.1mm aluminum filter) are depicted in Figure 4.1(c). Given the projected lengths of two materials, the noise-free projection data were calculated based on Eq. (4.1). Considering for larger counts the central limit theorem ensures that the photon noise distribution approaches a Gaussian[68], for

simplicity, uncorrelated Gaussian noise with respect to local intensity was added in all the measurements. The noise level was 1% unless otherwise stated.

The calibration data were employed to fit Eq. (4.2) to estimate the polynomial coefficients. The subsequently constructed functions F and G , along with the simulated breast phantom data, were used in Eq. (4.5) or (4.6) to perform material decomposition in a pixel-wise manner. In all studies, the pixel size was set as 0.1mm.

4.4 Simulation study results

4.4.1 The effect of total-projection-length constraint

Figure 4.2 shows the decomposition results from the conventional decomposition method with respect to solving Eq. (4.5) with positivity constraints. The data contained 1% noise. In the figure, l_1 is the decomposed projected-length of calcification, and l_2 is the decomposed projected-length of soft tissue. The ground true values are also plotted. Because the approximating functions $F(p, q)$ and $G(p, q)$ are sensitive to the data noise, the estimated projected lengths vary erratically with large deviations from the ground truth values.

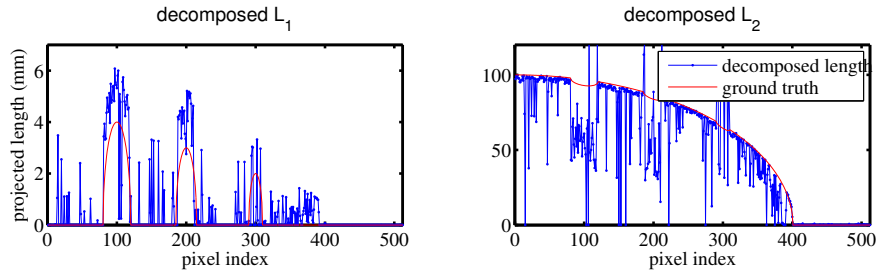


Figure 4.2: The decomposition results obtained by use of the conventional method (1% noise)

Figure 4.3 shows the decomposition results obtained by use of the total-projection-length constrained method associated with Eq. (4.6). In this case, the total projection length of the phantom, i.e. $l_1 + l_2$, is assumed to be exactly known for each detector pixel. The noise level of the projection data is also 1%. The decomposed l_1 in Fig. 4.2 has a root-mean-square error up to 1.5 mm with respect to the true calcification size, while the result in Fig. 4.3 has only a root-mean-square error as small as 0.01 mm. It clearly demonstrates that the new approach provides a more robust material decomposition with improved quantitative accuracy than that corresponding to the conventional decomposition method.

The proposed constraint can facilitate accurate image reconstruction for even more elevated noise levels. Figure 4.4 shows the decomposition results obtained by use of the total-projection-length constrained method when the measurements were contaminated with up to 10% Gaussian noise. The root-mean-square error increases to 0.1 mm, but no “bad pixels” that behave erratically are produced.

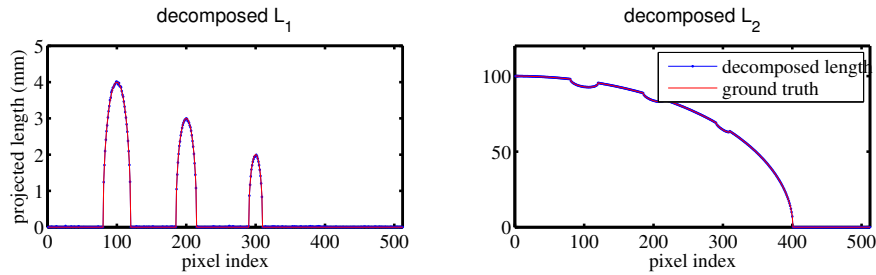


Figure 4.3: The decomposition results obtained by use of total-projection-length constrained method (1% noise)

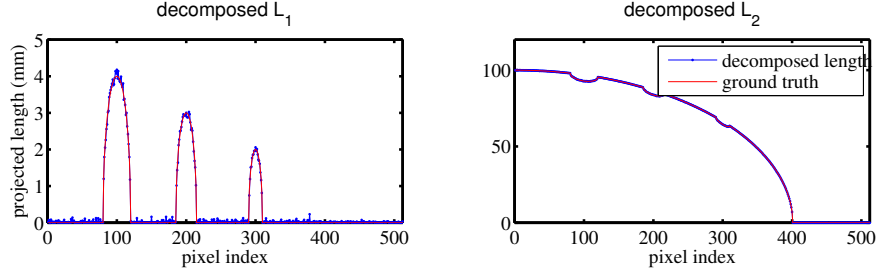


Figure 4.4: The decomposition results obtained by use of total-projection-length constrained method (10% noise)

4.4.2 The water-bath implementation of total-projection-length constraint

While the projected-length constraint can be readily implemented in computer simulations, it is not straightforward to do so in practical biomedical imaging applications. One may consider several candidate methods for determining an irregular-shaped objects' true dimensions. A solution we propose is to submerge the object in water bath. We explored this approach in a simulation study, proposing the sample placed in a rectangular container, as indicated in Fig 4.1(a) where the regions other than the breast phantom are filled with water. The total thickness of three materials (including water) along the X-ray beam direction is therefore known and assumed as $L=15$ cm everywhere.

Accordingly, the problem described in Eq. 4.6 should be modified to meet a three-material decomposition problem, with a newly introduced material, water, whose projected length is denoted as l_3 . With the presence of water, the new equivalent lengths of two basis materials (Al and Pl) are

$$\begin{aligned} p' &= \alpha_{1a}l_1 + \alpha_{2a}l_2 + \alpha_{3a}l_3 \\ q' &= \alpha_{1b}l_1 + \alpha_{2b}l_2 + \alpha_{3b}l_3, \end{aligned} \tag{4.7}$$

where all the coefficients come from the conversion relationships between the to-be-decomposed materials and the basis materials similarly defined in Eq. (4.4):

$$\begin{aligned}
\mu_{cal}(E) &= \alpha_{1a}\mu_{Al}(E) + \alpha_{1b}\mu_{Pl}(E) , \\
\mu_{tissue}(E) &= \alpha_{2a}\mu_{Al}(E) + \alpha_{2b}\mu_{Pl}(E), \\
\mu_{water}(E) &= \alpha_{3a}\mu_{Al}(E) + \alpha_{3b}\mu_{Pl}(E),
\end{aligned} \tag{4.8}$$

Therefore, a new total-projection-length-constrained, weighted-least-squares problem is formulated as

$$\begin{aligned}
(l_1, l_2, l_3) &= \arg \min_{l_1, l_2, l_3} w_1 \|f - F(p, q)\|^2 + w_2 \|g - G(p, q)\|^2 + w_3 \|f' - F(p', q')\|^2 + w_4 \|g' - G(p', q')\|^2 \\
s.t. \quad & l_1 + l_2 + l_3 = L
\end{aligned} \tag{4.9}$$

where f' and g' are two additional data sets acquired with the object immersed in water, using high- and low-energy spectra respectively. However, since there are three unknowns (l_1, l_2, l_3) , only three least-square terms along with the constraint are sufficient to stably solve Eq. (4.9). So we may drop either the third term $\|f' - F(p', q')\|^2$ or the last term $\|g' - G(p', q')\|^2$ and acquire three data sets only.

Though Eq. (4.9) seemingly escalates to a three-material decomposition problem, it essentially still serves for the two-material decomposition as water is considered as a known material. Figure 4.5 shows the decomposition results using the water-bath method. The data noise level was 1%. Again, the comparison with the conventional method clearly demonstrates that the proposed method is able to provide a robust material decomposition with a

high quantitative accuracy. The computed root-mean-square error of l_1 is around 0.01mm, as good as that in Fig. 4.3.

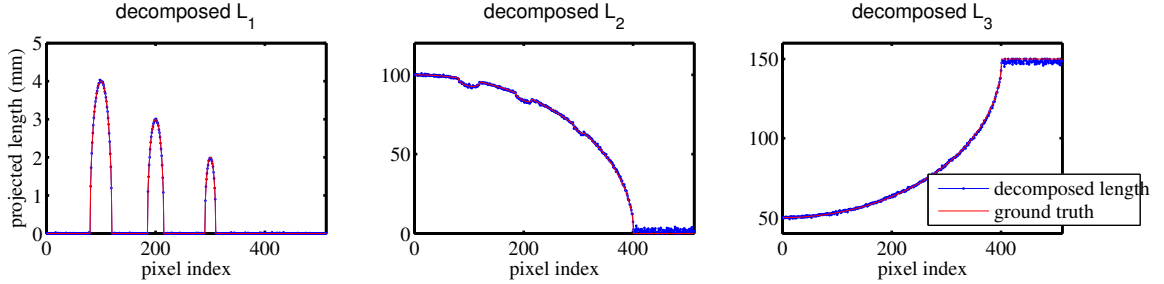


Figure 4.5: The total-projection-length constrained decomposition results using “water-bath” method (1% noise)

4.4.3 The scout-scan implementation of total-projection-length constraint

For the conditions where the object is not suitable for water bath, we propose another method to implement the total-projection-length constraint. In some cases, a sparse-view, low-dose tomographic scan can be quickly performed for 3D contouring of the object. The total-projection-length along a certain beam direction can be estimated from the reconstructed image by use of the scout-scan tomographic data. The reconstructed image from incomplete data is expected of low quality in recovering the attenuation map or identifying interior structures, however, it can provide useful information for outmost boundary segmentation, because the differentiation between object and air is considered an easy task.

In this study, a 3D numerical breast phantom was generated containing three spheres that represented calcifications. Figure 4.6(a) shows the central vertical slice of the phantom. The semi-major-axis sizes of the ellipsoid and the radius of the three embedded spheres are the same as those for the 2D phantom described in Sec. 4.3. Figure 4.6(b) illustrates

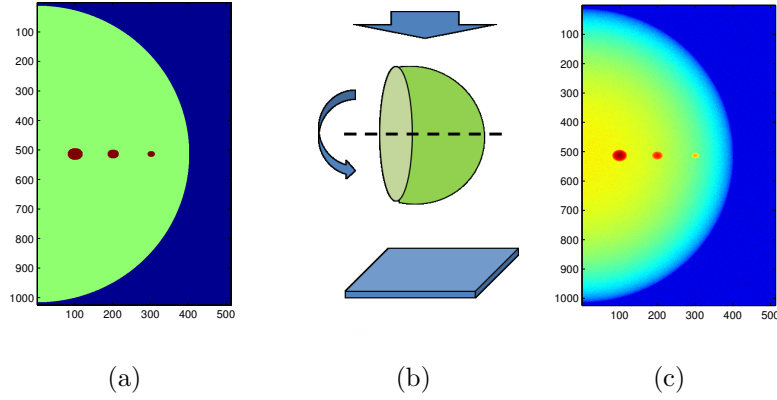


Figure 4.6: (a) The 3D numerical breast phantom. (b) The acquisition geometry of the scout scan. (c) A typical simulated projection image.

the acquisition geometry of the scout scan. The scout-scan projections were simulated at 30 angular positions evenly distributed over 180° , and as high as 10% Gaussian noise was added in all measurements in order to simulate a low-dose scan condition. The source spectrum employed for the scout scan was chosen as the low-energy one plotted in Fig. 4.1(c), for the reason that it achieves better contrast noise ratio than that using the high-energy spectrum. Figure 4.6(c) shows a typical scout-scan projection image.

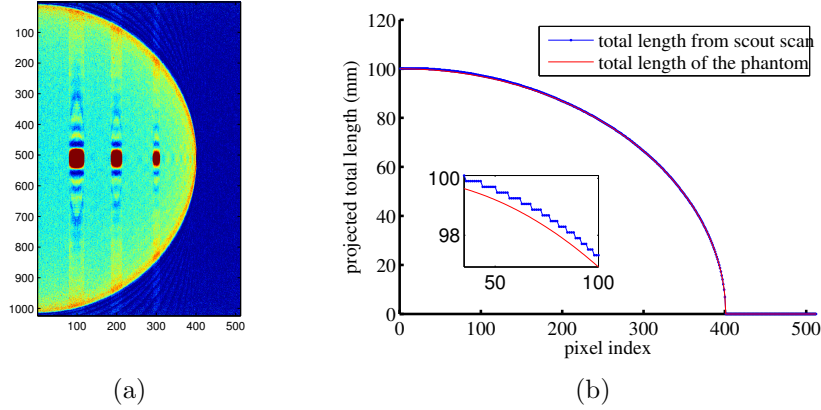


Figure 4.7: (a) The central vertical slice of the reconstructed image from 30-view data set. (b) The total-projection-length along the X-ray beam direction extracted from the reconstructed image.

Figure 4.7(a) shows the reconstructed image of the central vertical slice of the phantom from the 30-view data set and by use of the FBP algorithm. The reconstructed voxel size was 0.1 mm. There can be observed significant aliasing and beam hardening artifacts, due to the insufficient angular sampling and the effects of polychromatic spectrum, as well as considerable noise corruption. The shapes of the reconstructed spheres are obviously elongated, by comparison to the ground truth in Fig. 4.6(a), and therefore the scout-scan reconstruction cannot be used to reflect the true sizes of the calcifications. However, the outermost boundaries between the phantom and air can still be reliably reconstructed, because the attenuation properties of the two are quite different. A simple thresholding method was used to extract the total-projection-length of the phantom along the X-ray beam direction from the reconstructed image corresponding to Fig. 4.7(a). The extracted total-projection-length and the true phantom length are plotted in Fig. 4.7(b), showing the high accuracy of phantom-air boundary differentiation. Note that the two curves do not exactly coincide. There is still an error in the estimate of the total-projection-length by use of the scout scan, which can be up to 0.5 mm in this study.

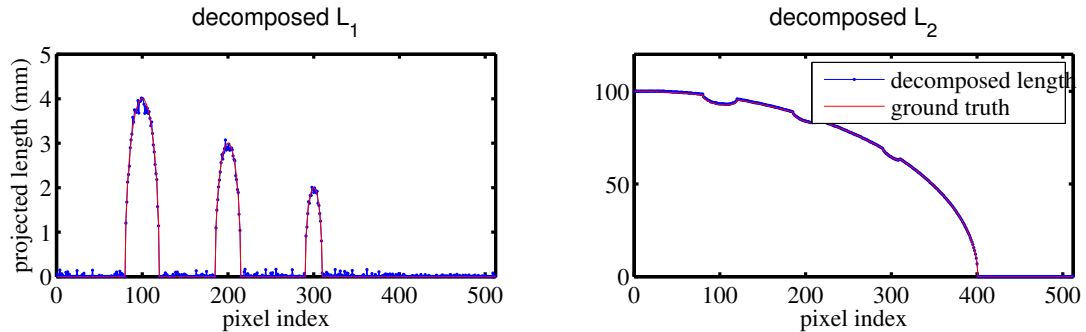


Figure 4.8: The total-projection-length constrained decomposition results using “scout-scan” method (5% noise)

The dual-energy projection sets of the phantom simulated at an angular position (with 5% Gaussian noise added), along with the corresponding total-projection-length constraint

obtained from the scout scan, were then employed for material decomposition by solving for Eq. (4.6). Figure 4.8 shows the decomposed projected length of calcifications (l_1) and the decomposed projected length of soft tissue (l_2). The root-mean-square error of l_1 is around 0.05 mm. The results demonstrate that the proposed material decomposition method does not require a strictly tight total-projection-length constraint. It is capable of producing robust and accurate decompositions as long as the constrain is within a reasonable precision.

4.5 Conclusions and Discussions

Conventional approaches to projection-based dual-energy material decomposition suffer from sensitivity to data noise, which is one factor in preventing dual-energy radiography from being widely employed in clinical applications. In this chapter, we described and demonstrated that a simple physical constraint can effectively regularize the decomposition process. By applying a constraint of the object’s total projection length along the X-ray beam direction, we obtained promising results in numerical studies with improved accuracy in estimates of projected thicknesses of decomposed materials in a breast phantom. The use of total-projection-length constraint essentially assumes the constituent materials are exclusively combined without sacrificing volume. Such a volume-conservation assumption was previously proposed in a three-material decomposition method conducted in image domain[185], acting as the third equation along with the dual-energy measurements to solve for three unknowns. However, this method only works well for monochromatic beams. When the imaging model involves polychromaticity, the 3×3 system of non-linear equations is expected to be very ill-posed and susceptible to noise. Alternatively, our method uses the constraint in another application such that it acts as an additional regularizer imposed on an existing 2×2 nonlinear

system for a two-material decomposition problem. Basically, it is the necessary information redundancy that eliminates the instability introduced by the data noise and the high non-linearity of the system.

In order to piratically implement the “total-projection-length” constraint, we also conducted simulation studies with two proposed “water-bath” and “scout-scan” ideas. The “water-bath” method utilizes a rectangular container filled with water to submerge the object, so that the size of the container is naturally the total-projection-length constraint. By acquiring one more data set with the object immersed in water, three measurements and one constraint can result in an accurate material decomposition. Though this method escalates the original task into a new three-material decomposition problem, it still employs dual-energy measurements only. The “scout-scan” method proposes a fast and low-dose CT scan for 3D contouring of the object, and the total-projection-length can be reliably estimated from the reconstructed image. The numerical study has demonstrated that the constraint does not have to be strictly tight and the material decomposition by use of the constraint obtained from scout scan can be robust and accurate. Note that the scout-scan method is different from the image-based decomposition approach. There is no need to densely acquire the projections, or to perform beam hardening corrections during the image reconstruction.

As a summary, our proposed total-projection-length constrained material decomposition method still follows the conventional dual-energy calibration and approximating protocols, but allows for robust decomposition performances against data noise and provides high accuracy in the estimates of decomposed materials’ projected thicknesses (i.e. line integrals). With the ease and reliability of projection-based material decomposition, the applications of dual-energy radiography may be promoted in more areas. For example, conventional mammography could only differentiate a tumor from healthy breast tissue; but using the

proposed constrained decomposition method, it is possible to simultaneously provide the size information in the beam direction which doctors may take advantage of to make a further surgery plan.

Chapter 5

Image reconstruction algorithms for tetrahedron beam computed tomography using CUDA-enabled GPUs

Tetrahedron beam computed tomography (TBCT) is a novel volumetric imaging system with a modified geometrical design compared to the commonly used cone-beam computed tomography (CBCT). It holds great promise of mitigating the photon-scattering problem, and features flexible geometrical settings that can facilitate imaging guided radiation therapy (IGRT). Though a few preliminary image reconstruction results came along with the invention of TBCT, a careful investigation of the reconstruction algorithms specific to the TBCT geometries has not been conducted. In this work, we derived a reliable analytical reconstruction method from the conventional FDK algorithm by introducing a proper weighting function in the TBCT image domain. An advanced total-variation regularized iterative algorithm is also developed that features fast convergence rate and robustness against data noise

and data incompleteness. In order to efficiently exploit the parallelism in GPU computing, the reconstruction algorithms were further optimized with special computational skills. The reconstructed results from numerical and experimental data sets have demonstrated the good performances of the proposed reconstruction algorithms in terms of both the image quality and computational efficiency.

5.1 Introduction

5.1.1 Descriptions of TBCT imaging system

Tetrahedron beam computed tomography (TBCT) is a novel volumetric imaging system with a modified geometrical design compared to the commonly used cone-beam computed tomography (CBCT)[178]. In TBCT, a linear array of sources are stacked vertically, forming a series of quasi-fan beams directed towards a linear CT detector array that is positioned orthogonally to the source array (Fig. 5.1). In contrast to the cone-shaped volume formed by the point source and a flat panel detector in CBCT, the stacked fan beams of TBCT form a tetrahedral volume. During the scan, the X-ray source sequentially operates along the z -direction and the corresponding projection images are continuously recorded at every angular position. While the gantry rotates around the object, the collected data can be used for volumetric image reconstruction.

In practice, rather than a single-row linear detector, the detector array may use multiple element rows for achieving better z -resolution. It should be noted that, due to the use of multiple X-ray sources, the number of detector element rows can be accordingly reduced while keeping the field of view (FOV) unchanged. For example, in a developed bench-top

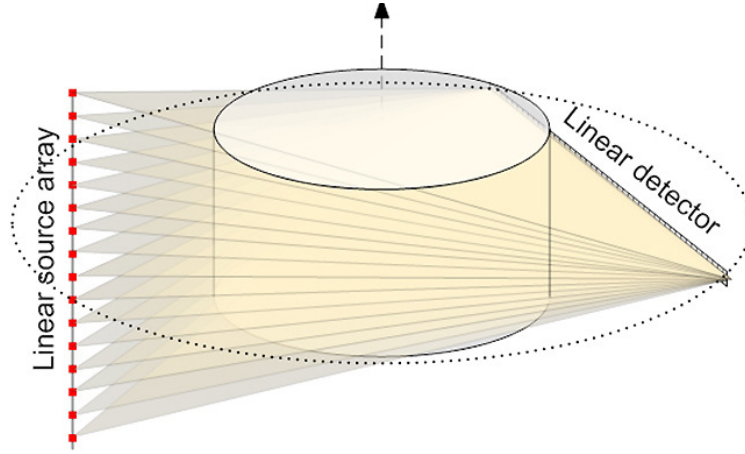


Figure 5.1: Diagram of TBCT geometry.

TBCT imaging system[178], the number of X-ray sources was 75, and the number of detector element rows was only 5 (Fig. 5.2). The reduction in the detector element numbers allows for the use of a high quality CT detector similar to those used in helical CT scanners.

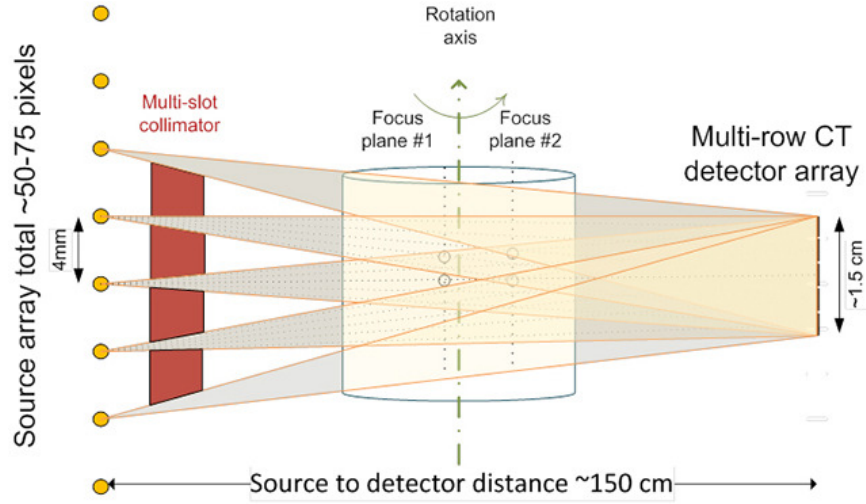


Figure 5.2: Side view of TBCT.

TBCT also holds great promise for mitigating image quality degradation due to photon scattering. Excessive scattered photons are considered a major problem for CBCT in which a large flat panel imager is employed. An anti-scatter grid usually has to be equipped in

CBCT scanners, placed right before the detector, in order to reject the scattered photons. TBCT, however, eliminates the need of anti-scatter grids. The source collimator is adjusted to make sure that all fan beams are well aligned with the the central row of the detector, as shown in Fig. 5.2. So most scattered photons are deflected out of the fan beam paths and therefore go undetected.

Besides the volumetric imaging, the TBCT system design is conceptually capable of stereoscopic imaging functionality. Similar to the X-ray tomosynthesis, the sequentially acquired TBCT projections, corresponding to different operating sources, can be synthesized to provide limited stereoscopic information along the direction orthogonal to the linear detector array. However much additional in-depth resolution can be obtained depends on the angular range of the irradiated region being overlapped by multiple fan beams. However, note that an ideal stereoscopic image obtained from TBCT may require a large-area detector and a densely distributed X-ray source array.

TBCT features flexible geometrical settings and can be further modified to incorporate dual-source arrays and dual-detector arrays to increase FOV and to facilitate imaging guided radiation therapy (IGRT)[83]. Figure 5.3(a) shows a possible configuration of dual-source, dual-detector TBCT system mounted on a regular LINAC gantry. In this novel design, the MV treatment beams and kV-TBCT beams share the same central axis, so the real-time projection imaging can be sensitive to the target motion that is orthogonal to the treatment beam. This is a desirable feature as opposed to the traditional kV-CBCT based IGRT system in which an additional gantry with 90 degree apart is installed, as shown in Fig. 5.3(b), and the kV beam is orthogonal to the treatment beam thus not sensitive to the target motion for real-time imaging.

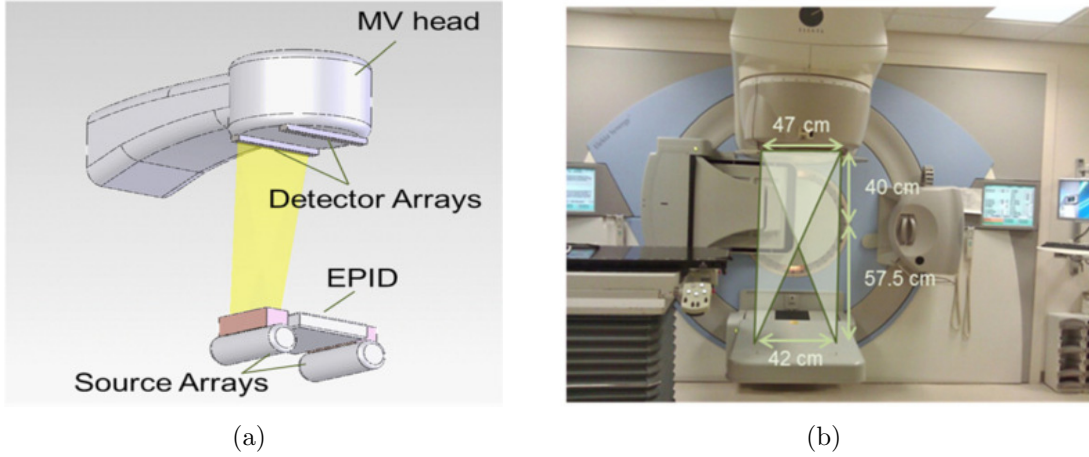


Figure 5.3: (a) A possible configuration of dual-source, dual-detector TBCT system mounted on a regular LINAC gantry. (b) Dimensions of a commercial LINAC with kV-CBCT installed.

5.1.2 TBCT reconstruction algorithms

Though the reconstruction algorithms for TBCT can be largely derived from those for CBCT, they have not yet been systematically investigated. As a variant of X-ray based 3D volumetric imaging setup, TBCT shares a lot of features in common with CBCT, however, TBCT system typically consists of multiple sources that may significantly increase the complexity of reconstruction and computational efficiency. Without the loss of generality, in this study we focus on the reconstruction algorithms for the TBCT design of single-source-array and single-detector-array, though they can be readily extended for dual-source-array, dual-detector-array or other more geometrically complicated designs by introducing proper data weights.

Filtered back projection (FBP) is the most widely used 2D image reconstruction algorithm in commercial machines because of its high computational efficiency. The FBP algorithm is derived from the Fourier slice theorem and provides accurate reconstruction when the sampling is sufficient. The well-known FDK algorithm[48] is a modified FBP that was developed for CBCT reconstruction, in which the 3D image is obtained by summing the

contribution to the object from all the tilted 2D fan beams. Note that the reconstructed images by use of FDK algorithm are inexact when the cone-angle of the fan beam is large. There has been previously reported the use of FDK-type algorithm adapted for TBCT reconstruction[81], however, an important “data redundancy” issue was not specified and the presented images showed excessively degraded quality. In Sec. 5.3.2 we will discuss the proper FDK algorithm adapted for TBCT and its acceleration implementation using GPUs.

For undersampled and/or noisy data, iterative reconstruction methods have been demonstrated to provide better image quality than analytical methods such as the FDK algorithm. A previous attempt for iterative TBCT reconstruction explicitly calculated and stored the system matrix on the hard drive[82]. Using a cylindrical image grid allowed for taking advantage of the symmetries of the circular scanning geometry and reducing the size of the system matrix; however, the size is still prohibitively large. Suppose the size of the reconstructed images was $256 \times 256 \times 256$ with a 256×5 detector array and a 75-element source array, the system matrix would be as large as 6000 GB. The saving and loading of the system matrix and the subsequent matrix multiplication computing is extremely time consuming. The explicit system matrix storage is not a wise and efficient strategy because it does not exploit the sparseness of the huge system matrix. There are also a few other limitations for TBCT image reconstruction with cylindrical image grid. For example, the calculation of the system matrix element has to be statistically estimated because the exact ray-passing areas are difficult to analytically compute. Also, the cylindrical voxelization essentially leads to a non-uniform resolution reconstruction, which is suboptimal.

In this study, a ray-tracing, Cartesian-coordinates-based iterative algorithm is developed for TBCT image reconstruction. The forward-projection and back-projection operators are computed “on the fly” and therefore no system matrix needs to be explicitly stored. The

OS-SART-FISTA-TV algorithm previously employed in CBCT image reconstruction [176] is adapted for TBCT to provide fast convergence and robust performance against noisy and/or undersampled data. The general framework of OS-SART-FISTA-TV algorithm will be introduced as the background detailed in Sec. 5.2.

A graphic processing unit (GPU) card is a specialized device specifically designed for parallel computations[94]. Compute unified device architecture (CUDA) is an extension of the C language that provides a convenient programming platform to exploit the parallel computational power of NVIDIA GPUs[118]. The CUDA-enabled GPU parallel programming technique has been successfully applied to accelerate image reconstruction in many imaging modalities[194, 119, 148]. Sec. 5.3.3 provides details of the derivation of TBCT ray-tracing model in 3D, and explains how GPU threads were allocated for both forward and backprojection, and the steps undertaken by each thread to compute the system matrix elements. Pseudo code of our implementation is also listed. Moreover, due to the sequential operation of the multi-sources in TBCT, special attention is required when optimizing the GPU code in order to achieve better computational efficiency under different system geometrical settings. Choices of two different implementations of the backprojection operator are offered upon the number of sources and the whole data size. In Sec. 5.3.4 we describe how the OS-SART-FISTA-TV framework, including forward projection and backprojection, is implemented on a multi-GPU architecture that can bring significant speedup.

A series of simulation studies are described in Sec. 5.4, in which the computational accuracy and efficiency of the developed TBCT reconstruction algorithms are carefully investigated. The reconstructed images from an experimental data set acquired in a bench top TBCT imaging system is presented in Sec. 5.5.

5.2 Background

5.2.1 Discrete imaging model for TBCT

We consider a discrete TBCT imaging model

$$\mathbf{g} = \mathbf{H}\mathbf{f}, \quad (5.1)$$

where $\mathbf{g} \in \mathbb{R}^M$ represents a lexicographically ordered vector describing the tetrahedron-beam projection data with the dimension M defined by the product of detector elements N_d , number of sources N_s and number of tomographic views acquired N_v . It is worth noting that, a TBCT projection dataset contains a third dimension that represents the irradiating source, as opposed to the CBCT dataset that is only indexed by the detector element and the tomographic view.

The vector $\mathbf{f} \in \mathbb{R}^N$ is a finite-dimensional approximation of the sought-after 3D attenuation coefficient map $f(\mathbf{r})$. In the studies described below, we assume without loss of generality that \mathbf{f} is formed by use of voxel expansion functions. The $M \times N$ system matrix \mathbf{H} represents a discrete imaging operator that maps \mathbf{f} to \mathbf{g} . In this work, \mathbf{H} is defined as discrete approximation of a divergent beam X-ray transform.

5.2.2 PWLS-TV iterative image reconstruction

In this study, a total-variation penalized weighted least square (PWLS-TV) estimator is considered for TBCT image reconstruction:

$$\hat{\mathbf{f}} = \underset{\mathbf{f} \geq \mathbf{0}}{\operatorname{argmin}} \|\mathbf{H}\mathbf{f} - \mathbf{g}\|_{\mathbf{W}}^2 + \lambda \|\mathbf{f}\|_{\mathbf{TV}}, \quad (5.2)$$

where $\|\cdot\|_{TV}$ indicates the total-variation semi-norm[153], and \mathbf{W} is a diagonal weight matrix with all positive entries. Note that \mathbf{W} describes the relative influence of the measurements in the data set. Typically in TBCT system, the source collimators are designed to shape the incident beams in such a way that the central rows of the detector usually receive more photons than the side rows at the top or at the bottom, therefore given more credence. Ideally, the weights correspond to the reciprocals of the signal variance. For simplicity, \mathbf{W} can be an identity matrix if there is no prior knowledge about the flat-field photon distribution on the detector.

There are numerous algorithms that have been developed to solve TV-regularized image reconstruction problems[33, 74, 143, 134]. In this study, an iterative reconstruction algorithm based on the FISTA framework[14] is employed for TBCT image reconstruction. FISTA is an efficient algorithm that can be applied to a variety of reconstruction methods that incorporate non-smooth regularizers typically like TV[14].

Let

$$d(\mathbf{f}) \equiv \|\mathbf{H}\mathbf{f} - \mathbf{g}\|_{\mathbf{W}}^2, \quad (5.3)$$

and

$$g_{tv}(\mathbf{f}) \equiv 2\lambda_{tv}\|\mathbf{f}\|_{TV} + \delta_C(\mathbf{f}), \quad (5.4)$$

where C represents a proper closed convex set with non-negative elements and δ_C is a indicator function that is defined as

$$\delta_C = \begin{cases} 0 & \text{if } \mathbf{f} \in C \\ +\infty & \text{elsewhere.} \end{cases} \quad (5.5)$$

The flowchart of the standard FISTA-TV[14] algorithm developed to solve Eq. (5.2) is provided in Table 5.1.

Table 5.1: The flowchart of the standard FISTA-TV algorithm

Algorithm 5.1	
Input: $L \geq L(d(f))$ - An upper bound on the Lipschitz constant of $\nabla d(\mathbf{f})$ Lipschitz constant: $\equiv 2\sigma_{\max}\{\mathbf{H}^T \mathbf{W} \mathbf{H}\}$, σ_{\max} represents the maximum eigenvalue.	
Initialization: $\mathbf{e}_1 = \mathbf{f}_0 = \mathbf{0}$, $t_1 = 1$	
for $k = 1$ to n do	
$\mathbf{x}_g = \mathbf{e}_k - \frac{1}{L} \nabla d(\mathbf{e}_k) = \mathbf{e}_k - \frac{2}{L} \mathbf{H}^T \mathbf{W} (\mathbf{H} \mathbf{e}_k - \mathbf{b})$	(5.6)
$\mathbf{f}_k = \text{prox}_{1/L}(g_{\text{tv}})(\mathbf{x}_g)$	(5.7)
$t_{k+1} = \frac{1 + \sqrt{1 + 4t_k^2}}{2}$	(5.8)
$\mathbf{e}_{k+1} = \mathbf{f}_k + \frac{t_k - 1}{t_{k+1}} (\mathbf{f}_k - \mathbf{f}_{k-1})$	(5.9)
end for	
Output: \mathbf{f}_n	

The algorithm can be summarized as the following steps. First, a gradient descent step is applied to minimize the least squares term $d(\mathbf{f})$, obtaining an intermediate image denoted as \mathbf{x}_g , as described in Eq. (5.6). Second, a TV-proximal problem stated in Eq. (5.7), defined as

$$\text{prox}_{1/L}(g_{\text{tv}})(\mathbf{x}_g) = \underset{\mathbf{u} \in C}{\operatorname{argmin}} 2\lambda_{\text{tv}} \|\mathbf{u}\|_{\text{TV}} + \frac{L}{2} \|\mathbf{u} - \mathbf{x}_g\|^2, \quad (5.10)$$

is solved by use of the fast gradient projection algorithm (FGP)[111]. In this study, an extended 3D version of the FGP algorithm was employed[176]. Finally the solution of the proximal problem \mathbf{f}_k is utilized to define a new image estimate \mathbf{e}_{k+1} that is substituted into the first step and the procedure is repeated until a convergence criteria is met.

It can be interpreted from Eq. (5.9) that, in each iteration the new image estimate \mathbf{e}_{k+1} is formed by use of the convergence momentum from the intermediate results of the previous two iterations. This strategy can greatly accelerate the iterative process towards to convergence. In fact, it can be demonstrated that the standard FISTA achieves a quadratic convergence rate[14] described as

$$F(\mathbf{f}_k) - F(\mathbf{f}^*) \leq \frac{2L\|\mathbf{f}_k - \mathbf{f}^*\|^2}{(k+1)^2}, \quad (5.11)$$

where $F(\cdot)$ is the objective function, k is the iteration number, \mathbf{f}_k is the image estimate at the k -th iteration and \mathbf{f}^* is the true solution to the optimization problem.

5.2.3 Ordered subsets acceleration strategy

When the standard FISTA is employed for TBCT image reconstruction, the basic gradient-descent update step in Eq. (5.6) will be the most time consuming step. This is because it requires to compute the operations corresponding to the forward-projection operator \mathbf{H} and the back-projection operator \mathbf{H}^T in each iteration, which is generally considered computationally burdensome in X-ray CT due to the large amount of projection data and image voxels. In addition, when the Lipschitz constant L is large, the update step size $1/L$ is small in the basic gradient step, which indicates that more iterations are needed to minimize $d(\mathbf{f})$.

Instead of employing all the projection data at once to compute the gradient, it is well known that an intermediate solution to a least squares minimization problem can be obtained more efficiently by employing a strategy in which the estimate of the object function is updated frequently by use of ordered subsets of the data sequentially. Such a procedure can accelerate convergence by a factor proportional to the number of subsets [70]. Many advanced iterative methods that seek to solve the least squares problem have incorporated the ordered subsets (OS) idea to accelerate the image reconstruction process[102, 78, 46].

In computed tomography, the sequential processing of ordered subsets is very natural, as projection data are collected separately at each projection angle as the source-detector gantry rotates around the patient. It should be noted that TBCT employs multiple sources, so there might be another grouping strategy in which all the rays starting from a certain source are clustered as one subset, rather than being grouped by the tomographic views. However, since each X-ray source may only irradiate one portion of the object and all the portions may not considerably overlap, in this case the image voxels won't be continuously updated by all subsets, therefore it may not bring the acceleration benefits. So in this study we stick to the the conventional ordered-subset strategy that is based on the sequence of tomographic views.

It has been established that the ordering of data access can also affect the convergence speed[58]. The multilevel projection access ordering scheme (MAS) was developed for algebraic reconstruction algorithms in order to achieve a further improvement in the convergence rate of the iterative reconstruction [57]. It is well known that two views of 90° apart have the maximum orthogonality and the minimum correlation, which can guide the optimal ordering of the projection access. For a system with V projection views ordered sequentially as $0, 1, \dots, V-1$, this scheme determines a number of levels $L = \log_2 V$. Views in one level halve

the angular spacing in the previous level, and each time we select a view to keep the overall correlation minimal with respect to the others already accessed. For example, if the imaging system acquires projection data that cover the range 0 to 180° , the first level is set to contain 0 (0°) followed by $V/2$ (90°). The second level has two elements and the indices are $V/4$ (45°), and followed by $3/4V$ (135°) which is ninety degree apart from the last. Similarly, the projection order of the third level is $V/8$ followed by $5V/8$, $2V/8$ (accessed) followed by $6V/8$ (accessed), and $3V/8$ followed by $7V/8$. The index should be skipped if it has been already accessed in the previous levels; also, it is rounded down to the nearest integer if the division results in a decimal. This process is repeated until all L levels are complete. The MAS scheme allows fast convergence since the first few update will be very significant and then gradually reduced to approach the solution.

5.2.4 Simultaneous algebraic reconstruction technique

The standard algebraic reconstruction technique (ART)[54] iteratively updates the voxels in a ray-by-ray manner. Later, Andersen and Kak [8] found that the correction can be simultaneously performed on all the rays and this can avoid the salt and pepper noise and striping artifacts in ART. The simultaneous algebraic reconstruction technique (SART) performs to be an efficient iterative algorithm for solving the least squares problem[75]. Along with the aforesaid ordered subset (OS) strategy, the combined OS-SART algorithm is widely used for iterative reconstructions[161], in which the projection measurements (i.e. line integrals) collected at a single view are used to simultaneously update image voxels. Then the view-by-view update strategy is performed for all view angles within each iteration.

The OS-SART algorithm adopted in this work is now reviewed briefly. Rewrite Eq. (5.1) in the form of element summation:

$$\sum_{j=1}^N h_{ij} f_j = g_i, \quad i = 1, 2, \dots, M, \quad (5.12)$$

where f_j is j th element of the vector \mathbf{f} (i.e. the voxel index), N is the number of image voxels; M is the number of source-detector element pairs (i.e. line integrals, or rays), and h_{ij} is the element of \mathbf{H} corresponding to the i -th row and j -th column, which can be interpreted as a weight element that represents the contribution of the j -th voxel to the i -th line integral. Note that for TBCT, g_i ($i = 1, 2, \dots, M$) include all the line integrals connecting every source and every detector element.

Consider that the projection data \mathbf{g} are grouped into T subsets that are indexed by v . In this study, T equals to the number of projection views N_v . Let the vector \mathbf{g}^v denote the projection data corresponding to the v -th subset. The reduced imaging model, representing the X-ray transform at a particular view angle, can be expressed as $\mathbf{g}^v = \mathbf{H}_v \mathbf{f}$, where \mathbf{H}_v contains a subset of the elements in the full \mathbf{H} . By use of the subset notation, Eq. (5.12) can be rewritten as

$$\sum_{j=1}^N h_{ij,v} f_j = g_i^v, \quad i = 1, 2, \dots, M_v, \quad v = 1, 2, \dots, T, \quad (5.13)$$

where g_i^v is the i -th component of \mathbf{g}^v , $h_{ij,v}$ is the element of \mathbf{H}_v corresponding to the i -th row and j -th column, and $M_v = N_d N_s$ is the total number of rays in the v -th subset.

The OS-SART algorithm is composed of two sub-steps, a forward correction step and a backprojection-update step. These two steps are implemented as

$$c_{i,v} = \frac{g_{i,v}^{data} - \sum_{j=1}^N h_{ij,v} f_{j,v-1}^k}{\sum_{j=1}^N h_{ij,v}} \quad (5.14)$$

$$f_{j,v}^k = f_{j,v-1}^k + \gamma_v \frac{\sum_{i=1}^{M_v} c_{i,v} h_{ij,v}}{\sum_{i=1}^{M_v} h_{ij,v}} \quad (5.15)$$

where $g_{i,v}^{data}$ represents the i -th ray projection data in the v -th subset, and $f_{j,v-1}^k$ and $f_{j,v}^k$ are the j -th voxel value updated by use of the $(v-1)$ -th and the v -th data subset at the k -th iteration, respectively. $c_{i,v}$ is the corrective value. γ_v is the step size of which a general choice is $(0, 2)$.

Equations (5.14) and (5.15) can be expressed in a matrix-vector form as

$$\mathbf{f}_v^k = \mathbf{f}_{v-1}^k - \gamma_v \mathbf{D}_v \mathbf{H}_v^T \mathbf{U}_v (\mathbf{H}_v \mathbf{f}_{v-1}^k - \mathbf{g}_v) \quad (5.16)$$

Here, \mathbf{U}_v is a weight matrix defined in Eq. (5.17), and each element of \mathbf{U}_v is the reciprocal of the i -th ray length.

$$\mathbf{U}_v = \text{diag}\{1/\sum_{j=1}^N h_{ij,v}\} \quad i = 1, 2, \dots, M_v. \quad (5.17)$$

The matrix \mathbf{D}_v can be interpreted as a preconditioning matrix defined in Eq. (5.18). Each element of \mathbf{D}_v is the reciprocal of the sum of intersection lengths of rays that intersect the j -th voxel in the v -th subset.

$$\mathbf{D}_v = \text{diag}\{1/\sum_{i=1}^M h_{ij,v}\} \quad j = 1, 2, \dots, N. \quad (5.18)$$

Equation (5.16) can be interpreted as a pre-conditioned gradient-based update method with sequential data-access strategy. It is well known that incorporating a preconditioning matrix in the gradient step can improve the convergence rate of an iterative algorithm[49], and as we see, OS-SART implicitly incorporates such a preconditioning matrix \mathbf{D}_v . So the standard FISTA-TV algorithm can be accelerated by replacing the gradient update step, Eq. (5.6), with the OS-SART update strategy, Eq. (5.16), while all the other steps remain the same. Note that the weight matrix \mathbf{W} in the original PWLS-TV problem is now defined as \mathbf{U} . In this study, the modified algorithm is referred to as OS-SART-FISTA-TV which was previously developed by Qiaofeng for CBCT reconstruction[176]. The proposed OS-SART-FISTA-TV algorithm is detailed in Table 5.2, and will be employed for solving Eq. (5.2) in the context of TBCT reconstruction.

Table 5.2: The flowchart of the OS-SART-FISTA-TV algorithm

Algorithm 5.2
Input: $L \geq L(d(f))$ - An upper bound on the Lipschitz constant of $\nabla d(\mathbf{f})$ Lipschitz constant: $\equiv 2\sigma_{\max}\{\mathbf{H}^T \mathbf{W} \mathbf{H}\}$, σ_{\max} represents the maximum eigenvalue. Initialization: $\mathbf{e}_0^1 = \mathbf{f}^0 = \mathbf{0}$, $t_1 = 1$ for $k = 1$ to n do for $v = 1, 2, \dots, N_v$ do $\mathbf{e}_v^k = \mathbf{e}_{v-1}^k - \gamma_v \mathbf{D}_v \mathbf{H}_v^T \mathbf{U}_v (\mathbf{H}_v \mathbf{e}_{v-1}^k - \mathbf{g}_v)$ end for $\mathbf{f}^k = \text{prox}_{1/L}(g_{\text{tv}})(\mathbf{e}_v^k) = \text{prox}_{1/L}(2\lambda_{\text{tv}}\ \mathbf{f}\ _{\text{TV}})(\mathbf{e}_v^k)$ $t_{k+1} = \frac{1 + \sqrt{1 + 4t_k^2}}{2}$ $\mathbf{e}_0^{k+1} = \mathbf{f}^k + \frac{t_k - 1}{t_{k+1}}(\mathbf{f}^k - \mathbf{f}^{k-1})$ end for Output: \mathbf{f}^n

5.3 GPU-accelerated TBCT reconstruction algorithms

5.3.1 Measurement geometry

The region to be reconstructed is a rectangular cuboid centered at the origin of the Cartesian coordinate system, as shown in Fig. 5.4. The edges are parallel to the axes of the coordinate system and the left-bottom-back voxel is located at $(x_{\min}, y_{\min}, z_{\min})$. The number of voxels along the three coordinates are denoted by N_x, N_y and N_z , respectively, totally $N = N_x N_y N_z$ voxels. The image voxel is assumed to be isotropic with the physical size Δ_v . \mathbf{f} is the 3D array that contains all the voxels of the reconstructed image.

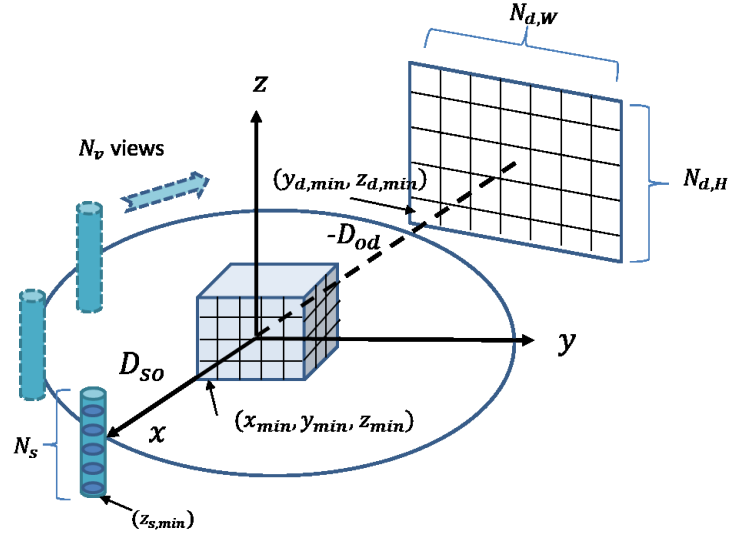


Figure 5.4: A schematic of the TBCT imaging geometry

The source array is originally located $x = D_{so}$, and the distance between the source array and the origin doesn't change during the gantry rotation. The source array contains N_s elements and all the sources are stacked vertically with the uniform spacing Δ_s , of which the most bottom source is located at $(D_{so}, 0, z_{s,\min})$.

The measurements \mathbf{g} are a set of projection pixel values indexed by the detector element, the source, and view angle. The detector is a flat panel whose center is the origin of y - z plane located at $x = -D_{od}$. The detector has N_d elements in total, $N_{d,W}$ in width and $N_{d,H}$ in height, and the element is assumed to be isotropic with the pixel size Δ_d . The left-bottom detector element is located $(-D_{od}, y_{d,\min}, z_{d,\min})$. The projection dataset from N_v views are assumed to be evenly acquired over $[0, 2\pi)$ with equal angular step Δ_θ . As a result, the total number of elements contained in \mathbf{g} is $N_{d,W}N_{d,H}N_sN_v$. In the view-by-view update strategy, the projection at each view angle is denoted as an array \mathbf{g}_v ($v = 1, 2, \dots, N_v$) and correspondingly \mathbf{g}_v has the dimension of $N_{d,W} \times N_{d,H} \times N_s$.

5.3.2 Implementation of the FDK algorithm

The first and most popular approximate reconstruction scheme for cone-beam projections is the algorithm developed by Feldkamp and colleagues[48], referred to as the Feldkamp, Davis, and Kress (FDK) method. This algorithm, used by most commercial vendors for CBCT with 2D detectors, employs a convolution-backprojection method similar to the FBP algorithm. FDK is easy for hardware implementation and capable of producing good reconstructed images when the data sampling is sufficient. However, the FDK algorithm is inexact when the cone-angle of the fan beam is large, which may result in structure distortion and resolution degradation appearing at the top and bottom of the reconstructed images[188]. This is due to the underlying principle that large cone-angle fan beams contain incomplete frequency contents of the object along z -axis for accurate reconstruction.

Considering the high efficiency of the analytic-based reconstruction algorithm, it is still desirable to develop a FDK-type algorithm that is adapted for TBCT reconstruction. Ideally,

the TBCT projection data can be weighted, ramp-filtered and backprojected in a similar way as the conventional FDK. However, there is a significant issue that requires attention. All the CBCT rays start from a single source typically at the center of y - z plane; while the TBCT rays vary their starting points at a series of sources. As a result, in TBCT system there could be multiple fan beams passing through a image voxel, with the starts from different sources, as shown in Fig. 5.5. The number of fan beams associated with a voxel may vary for different voxels depending on their specific geometrical locations. The conventional FDK algorithm for CBCT is implemented in a “voxel-driven” fashion such that at each view angle an image voxel will be updated by one fan-beam. If the TBCT reconstruction follows the same routine, some voxels might get backprojected more frequently than the others. This will result in non-uniform updates of the image volume.

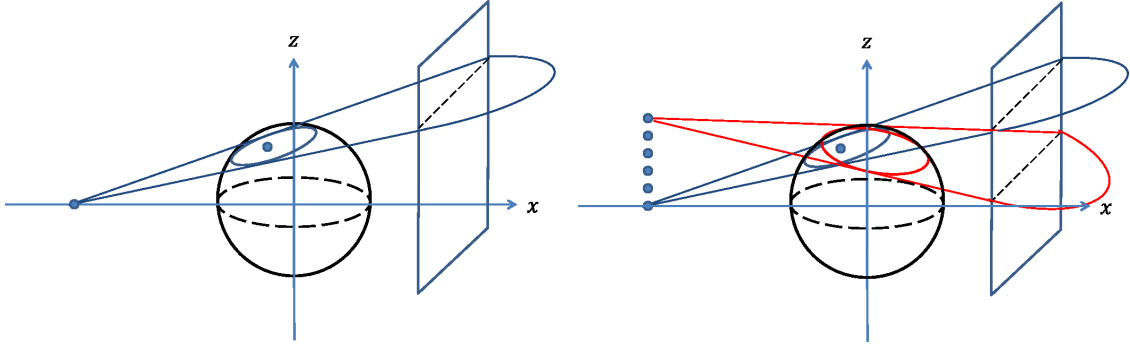


Figure 5.5: The illustrations of backprojection processes for CBCT (left) and TBCT (right).

The problem mentioned above is referred to as the “data redundancy” issue in analytic-based algorithms, also encountered in the scenarios of offset-detector CBCT[16] and dual-source CBCT[100]. For those image voxels with multiple source-detector element pairs passing through, data values have to be normalized by a weighting function before being used to update the voxel. Typically for offset-detector / dual-source CBCT, the Parker Weighting[126] method is commonly used to apply a filter in the projection domain so that the redundant data are normalized. However TBCT has a more complicated situation that the “data

redundancy” condition is image voxel dependent. A weighting function in the projection domain is therefore difficult to design, especially in the case where the sources are non-uniformly distributed along the array, e.g. for the purpose of optimizing z -axis resolution of the reconstructed image.

A simple remedy to this problem is to design a voxel-dependent weighting strategy. When there are multiple fan beams passing through the voxel of interest, the backprojection values from these fan beams can be weighted in the following proposed ways:

- **Equal weight:** For a given image voxel, we count the total number of fan beams that pass through, and the sum of all backprojection values is scaled by this number and then applied to update the voxel. This method essentially assigns the contributions of all the rays within the same projection with equal weights.
- **One weight:** For a given image voxel, we only select the fan beam that has the smallest cone angle with respect to the voxel. As discussed above, a smaller cone angle means the fan-beam projection contributes more reliable backprojection values when employing the FBP algorithm. In this method the backprojection is performed only once for each voxel.
- **Inverse weight:** For a given image voxel, we assign all the passing fan beams with the weights inversely proportional to their respective cone-angles. Therefore all available measurements contribute to the backprojection for this voxel but the ray that has the smallest cone angle plays the most important role.

In this section, we conduct a quick performance comparison between the proposed weighting methods for TBCT-FDK. Figure 5.6 displays the previously reported reconstruction results

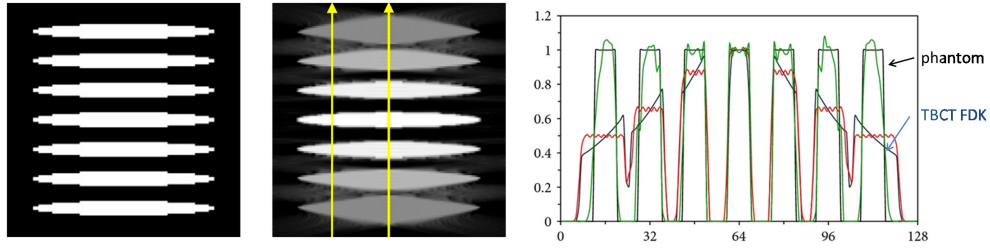


Figure 5.6: Reconstruction performance of the TBCT-FDK previously reported. (left) the central vertical plane of the phantom; (right) the corresponding reconstructed image; (right) the profile comparison along the central vertical line.

by use of TBCT-FDK algorithm developed by *Kim et al.*[81]. The phantom was a stack of thin ellipsoid disks and the largest cone angle was 20 degree. The “data redundancy” issue was not mentioned in that work. The reconstructed image showed significant elongation of the disks along the longitudinal axis and a drop in the reconstructed CT values at large cone angles.

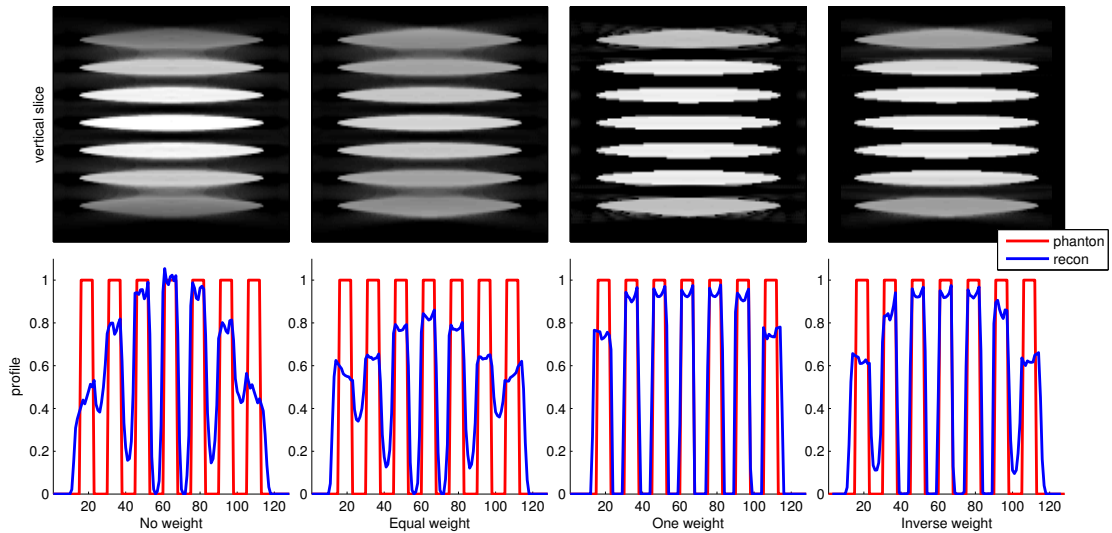


Figure 5.7: Reconstruction performance of the TBCT-FDK developed by the author. Each column corresponds to different weight strategy for handling “data redundancy” issue.

Figure 5.7 displays the reconstruction results by use of the proposed TBCT-FDK algorithm. The simulation conditions are all the same as those described in the reference[81] that produced Fig 5.6. The top row displays the reconstructed images of the central vertical plane of the phantom. The bottom row shows the profile comparison corresponding to the central vertical lines of the top-row images. Four different weighting strategies were employed when handling the “data redundancy” issue. The first one “no weight” means all the back-projection values were added for updating voxels when available without any scaling. The other three “equal weight”, “one weight” and “inverse weight” correspond to the three methods described above, respectively. The previously reported reconstruction result visualizes very similar to that with no weighting applied, showing the worst performance. Among all the results, “one weight” methods performs best in terms of the reconstructed CT value accuracy, because it only employs the most reliable measurement that corresponds to the smallest cone-angle. Nevertheless, this method produces saw-shaped discontinuities along the disk edges, because adjacent voxels may be associated with fan beams that correspond to largely different cone angles when the source spacing is considered too wide. “Equal weight” method provides the smoothest reconstructed image by averaging all the contributions from all available measurements, but at the cost of reconstruction accuracy. “Inverse weight” method achieves kind of balanced performance from the previous two strategies, and has the room for further improvement by carefully tuning the weights. In conclusion, TBCT-FDK can provide better reconstruction results than those that were previously reported as long as the “data redundancy” issue is properly addressed.

The flowchart of the FDK algorithm adapted for TBCT (with inverse weight strategy) is provided in Algorithm 5.3. The backprojection is implemented in a way that is referred to as “voxel-driven” approach, which will be detailed in the next section. For GPU implementation, we assigned each thread to execute the backprojection for a single voxel, which is

Table 5.3: The flowchart of the FDK algorithm(on kernel)

Algorithm 5.3

```

kerneK_FDK<<< ( $N_x, 1, 1$ ), ( $N_y, N_z, 1$ ) >>> (f,  $\tilde{\mathbf{G}}$ )
Input: cosine weighted, row-wise ramp-filtered projection data  $\tilde{\mathbf{G}}$ 
Output: f
 $x=x_{\min}+(\text{threadIdx.x})\Delta_v$ ;  $y=y_{\min}+(\text{blockIdx.x})\Delta_v$ ;  $z=z_{\min}+(\text{blockIdx.y})\Delta_v$ ;
 $\Sigma = 0$ ;
for  $\mathbf{v} = 0$  to  $N_v - 1$  do
    totalWeight= 0;
     $\theta = \mathbf{v}\Delta_\theta$ ;
    for  $\mathbf{k} = 0$  to  $N_s - 1$  do
         $t = x\cos\theta + y\sin\theta$ ;  $s = -x\cos\theta + y\cos\theta$ ;
         $p = \frac{D_{so}t}{D_{so}-s}$ ;  $q = \frac{D_{so}(z-z_s)}{D_{so}-s}$ ;
         $\mathbf{p} = (p - z_{d,\min} + z_s)/\Delta_d$ ;  $\mathbf{q} = (q - y_{d,\min})/\Delta_d$ ;
        if ( $0 \leq \mathbf{p} < N_{d,W}$  and  $0 \leq \mathbf{q} < N_{d,H}$ )
             $w = \text{fabs}(z - z_s)$ ;
             $\Sigma += w \frac{D_{so}^2}{(D_{so}-s)^2} \tilde{\mathbf{G}}[\mathbf{p}][\mathbf{q}][\mathbf{k}][\mathbf{v}]\Delta_\theta$ ; (fetch interpolated data from texture memory)
            totalWeight+=  $w$ ;
        end if
    end for
end for
if totalWeight $\neq 0$ 
     $\mathbf{f}[\text{threadIdx.x}][\text{blockIdx.x}][\text{blockIdx.y}] = \Sigma/\text{totalWeight}$ ;
end if

```

reflected in the GPU kernel configuration $\langle\langle\langle (N_x, 1, 1), (N_y, N_z) \rangle\rangle\rangle$ where the contents in the parentheses describe the assigned dimensions of the grid and blocks. The input $\tilde{\mathbf{G}}$ is the cosine weighted, row-wise ramp-filtered projection data that has been pre-processed following the routine of the conventional FDK. Before launching the kernel function, $\tilde{\mathbf{G}}$ is imported into texture memory in GPU which is read-only and optimized for interpolation operations.

5.3.3 Implementation of the forward / backprojection operator

Comparison of the existing forward / backprojection models

For computed tomography, the discrete transform \mathbf{H} , in which line integrals of a known image are calculated, is known as the projection operation. The reverse model \mathbf{H}^T , generally defined as the transpose (or adjoint) of the forward model, is known as the backprojection operation. In iterative reconstruction, repeated applications of the forward and backprojection actions are needed to solve for the image that minimizes an appropriate objective function.

Many methods exist for X-ray transform projection and backprojection, like voxel-driven, ray-driven, and distance-driven, all of which provide some compromise between computational complexity and accuracy. In the voxel-driven approach, a ray is defined by connecting a line from the source through the center of the voxel of interest to the detector. Once a location of intersection on the detector is determined, a value is obtained from the detector by (typically linear) interpolation, and it is used for backprojection to update this voxel. This is exactly what the FDK algorithm is doing. Voxel-driven backprojection is easy for fast hardware implementation and therefore the FDK algorithm is widely employed in commercialized CT systems. Note that the FDK algorithm does not involve the forward projection. The matched forward model \mathbf{H} can be computed as the adjoint operator of the backprojection process, namely by a “reverse interpolation” to determine the contribution from the specific voxel to the detector elements surrounding the intersection point. However, this type of voxel-driven forward model is less effective and rarely used for iterative reconstruction. Because when the detector element size is small enough compared to the image voxel size, this model cannot get every pixel projected and hence will introduce Moire pattern artifacts in the projection data[39, 189].

In the ray-driven approach, a ray is defined by connecting a line from the source through the image to the center of the detector element of interest. The contribution from a voxel to a ray, i.e. the forward process, can be calculated based on the intersection length of the ray within the voxel (Siddon’s method[138]). Another ray-driven model (interpolation method) uniformly samples the ray and each sampling point takes the value using tri-linear interpolation of surrounding voxels; all sampled intensities are then integrated to obtain the projected value. In practice, the Siddon’s method is more popular in which both the forward and backprojection process are easy to implement, because the system matrix element $h_{i,j}$ has a very clear physical meaning: the intersection length of the i -th ray within the j -th voxel. In terms of the interpolation method, the forward process may produce a more smooth projection image if one can densely sample along the ray, however the drawback is also significant. First, the tri-linear interpolation operations in a 3D volume are time-consuming. Second, the matched backprojection process, requiring a “reverse interpolation”, lacks an efficient algorithm to compute. As opposed to the voxel-driven approach, the ray-driven approach should be used with caution in the cases when the projection data are too coarse compared to the desired image resolution, because during the backprojection process some image voxels may not get backprojected by any passing rays. This will result in a few “void” voxels in the image volume. However, such an insufficient-data-caused reconstruction problem can be mitigated by using advanced iterative methods, e.g. PWLS-TV, which incorporate prior knowledge and proper regularizations applied in the image domain.

A more emerging strategy called distance-driven approach has been proposed over the last few years[39, 40]. In this method, the detector pixel of interest and the image voxel of interest are mapped onto a common plane. The overlapped areas are calculated as the weights to determine the contribution from the voxel to the pixel (forward-projection process) or the contribution from the pixel to the voxel (back-projection process). Such a weight-calculating

kernel is self-adjoint. The most promising benefit of the distance-driven approach is that it can eliminate those concerns raised when the pixel size is too large compared to the voxel size or vice versus. In no case will there be void pixels or void voxels produced. However, the cost is the computational efficiency. A typical implementation has an inner loop that adjusts the calculation with an if-else branch depending on the relative positions between voxel and detector element boundaries. For 3D image reconstruction, the patterns of voxel and detector element boundaries are generally non-uniform when they are mapped onto a common plane, resulting in irregularity and poor predictability of the branch behavior and making it difficult to effectively implement on GPUs.

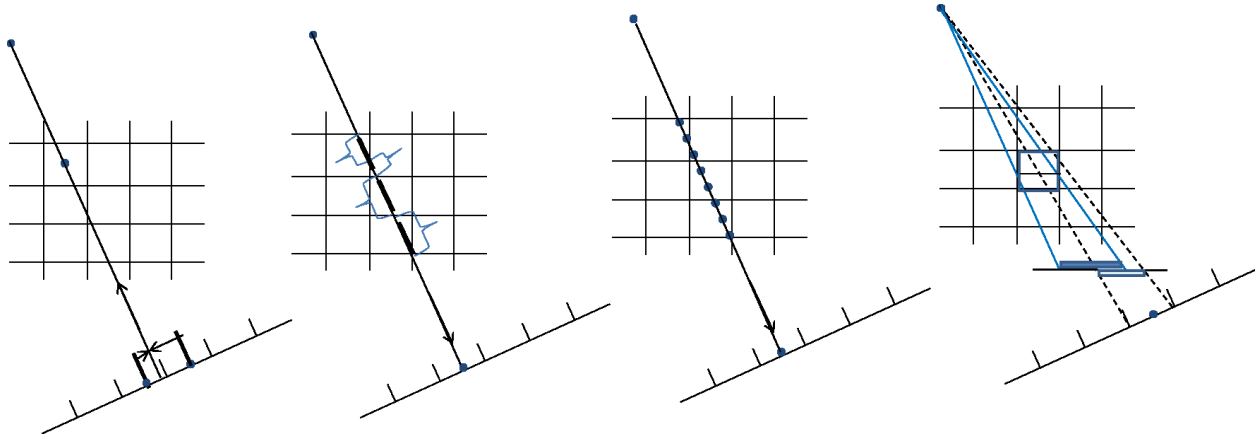


Figure 5.8: The schematics for (a) voxel-driven backprojection, (b) ray-driven (Siddon's method) projection, (c) ray-driven (interpolation method) projection, (d) distance-driven forward/backprojection.

For the purpose of easy comparison, the schematics of voxel-driven backprojection, ray-driven (Siddon's method and interpolation method) projection, and distance-driven forward/backprojection for 2D X-ray transform are illustrated in Fig. 5.8. The 3D case can be similarly understood by extending those ideas in the third dimension.

After a careful investigation and a comprehensive comparison, we chose Siddon's method to implement the forward and backprojection operators in TBCT. The most important

motivation is the need for high computational efficiency. Since a typical TBCT imaging system may have ten or up to one hundred sources, theoretically the computational burdens for all these models are thus increased by N_v times. So far the distance-driven approach has not been fully optimized for GPU implementation with an efficient algorithm to handle the irregular branch behavior, so it can be very slow compared to the other models. Though distance-driven model can avoid artifacts in some extreme cases when the detector element size and image voxel size are not comparable, it is not a necessary demand for image reconstruction as long as we can carefully design the geometry parameters, or using sparsity-driven regularizations incorporated in the iterative algorithm. Siddon's ray-driven method possesses a good balance between computational complexity and accuracy. Also it is naturally suitable for GPU parallelism and has been widely used in CBCT reconstruction applications[171, 71, 125]. However, it should be kept in mind that, the development of X-ray transform modeling and implementation, including the distance-driven approach, is still in progress and the current method may be supplanted by more advanced techniques in the future.

Implementation of the forward operator \mathbf{H}

In the ray-driven approach, the projection value of a ray is considered as the weighted sum of the voxel values that the ray passes through. The weight is exactly the system matrix element $h_{i,j}$ which describes the intersection length of the i -th ray and the j -th voxel. Siddon's method provides a very efficient algorithm to compute the intersection length[138, 73].

Without loss of generality, Fig. 5.9 illustrates a two-dimensional case, where the ray is not considered passing through voxels. Instead, from another perspective of view, the ray is passing by a series of horizontal and vertical lines. Suppose the source position (x_s, y_s, z_s) and

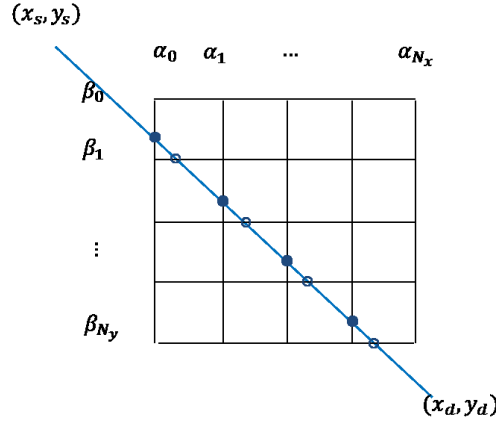


Figure 5.9: A 2D illustration of Siddon's ray-tracing strategy in which intersections of the ray with lines are considered.

detector element position (x_d, y_d, z_d) determine a specific ray. Denote two sets of parameters $\{\alpha_i\}$ ($i = 0, 1, \dots, N_x$) and $\{\beta_j\}$ ($j = 0, 1, \dots, N_y$), where $\alpha_i = \frac{x_i - x_s}{x_d - x_s}$ is the distance from the i -th x -plane to the source normalized by the source-detector distance. Similar definition can be obtained for $\beta_j = \frac{y_j - y_s}{y_d - y_s}$. Since all the x -planes and y -planes are parallel and equally spaced, $\{\alpha_i\}$ and $\{\beta_j\}$ can be easily computed.

The general idea of Siddon's method is to trace the given ray starting from the source. At each time encountering an intersection, the next smallest parametric value from $\{\alpha_i\}$ and $\{\beta_j\}$ determines the next intersection. Obviously, the length of the ray contained within the current voxel is simply the difference between the two adjacent parametric values. The contributions from every voxel accumulate along the ray until the detector element is reached, which determines the corresponding projection value.

It can be found that the ray-driven approach naturally can be implemented in a highly parallelized fashion. Algorithm 5.4 lists the pseudo code of the GPU kernel function for the forward operator \mathbf{H}_v responsible for generating the projection corresponding to the v -th

Table 5.4: The flowchart of the algorithm for ray-driven forward operator (on kernel)

Algorithm 5.4	
<hr/>	
kernek.forward<<< $(N_{d,W}, 1, 1), (N_{d,H}, N_s, 1) >>> (\mathbf{f}, \theta, \mathbf{g}_v, \mathbf{L}_v)$	
Input: the image volume \mathbf{f} , the view angle at the v -th subset θ	
Output: the generated projection \mathbf{g}_v , the ray length \mathbf{L}_v	
Initialization:	
$x'_s = D_{so}; \quad y'_s = 0; \quad z_s = z_{s,\min} + (\text{blockIdx.y})\Delta_s;$ $x'_d = -D_{od}; \quad y'_d = y_{d,\min} + (\text{threaIdx.x})\Delta_d; \quad z_d = z_{d,\min} + (\text{blockIdx.x})\Delta_d;$ $x_s = x'_s \cos\theta + y'_s \sin\theta; \quad y_s = -x'_s \cos\theta + y'_s \cos\theta;$ $x_d = x'_d \cos\theta + y'_d \sin\theta; \quad y_d = -x'_d \cos\theta + y'_d \cos\theta;$	
Define: $\alpha_x(i) \equiv \frac{(x_{\min} + i\Delta_v) - x_s}{x_d - x_s}; \quad \alpha_y(i) \equiv \frac{(y_{\min} + j\Delta_v) - y_s}{y_d - y_s}; \quad \alpha_z(k) \equiv \frac{(z_{\min} + k\Delta_v) - z_s}{z_d - z_s};$ $\alpha_{x,\min} = \min(\alpha_x(0), \alpha_x(N_x)); \quad \alpha_{y,\min} = \min(\alpha_y(0), \alpha_y(N_y)); \quad \alpha_{z,\min} = \min(\alpha_z(0), \alpha_z(N_z));$ $\alpha_{x,\max} = \max(\alpha_x(0), \alpha_x(N_x)); \quad \alpha_{y,\max} = \max(\alpha_y(0), \alpha_y(N_y)); \quad \alpha_{z,\max} = \max(\alpha_z(0), \alpha_z(N_z));$ $\alpha_{\min} = (\alpha_{x,\min}, \alpha_{y,\min}, \alpha_{z,\min}); \quad // \text{entry point}$ $\alpha_{\max} = (\alpha_{x,\max}, \alpha_{y,\max}, \alpha_{z,\max}); \quad // \text{exit point}$	
if $\alpha_{\min} < \alpha_{\max}$	
exit; // the ray does not fall into the range of the detector	
end if	
if $x_s < x_d$	
$i_{\min} = [\phi_x(\alpha_{\min})]; \quad j_{\min} = [\phi_y(\alpha_{\min})]; \quad k_{\min} = [\phi_z(\alpha_{\min})]$ $i_{\max} = [\phi_x(\alpha_{\max})]; \quad j_{\max} = [\phi_y(\alpha_{\max})]; \quad k_{\max} = [\phi_z(\alpha_{\max})]$	
else	
$i_{\min} = [\phi_x(\alpha_{\max})]; \quad j_{\min} = [\phi_y(\alpha_{\max})]; \quad k_{\min} = [\phi_z(\alpha_{\max})]$ $i_{\max} = [\phi_x(\alpha_{\min})]; \quad j_{\max} = [\phi_y(\alpha_{\min})]; \quad k_{\max} = [\phi_z(\alpha_{\min})]$	
end if	
Define: $\alpha_{lu} \equiv \frac{\Delta_v}{\ (l_d - l_s)\ }; \quad l_u \equiv \begin{cases} 1 & \text{if } l_s < l_d \\ -1 & \text{else,} \end{cases}; \quad (l = x, y, z)$	
$i = i_{\min}; \quad j = j_{\min}; \quad k = k_{\min};$	
$p = 0; l = 0; \quad \alpha_c = \alpha_{\min}; \quad L = \ (x_s, y_s, z_s) - (x_d, y_d, z_d)\ ;$	
while $(\alpha_c < \alpha_{\max})$	
if $\min(\alpha_x, \alpha_y, \alpha_z) = \alpha_x$	
$p = p + (\alpha_x - \alpha_c)L\mathbf{f}[i][j][k]; \quad l = l + (\alpha_x - \alpha_c)L; \quad i = i + i_u; \quad \alpha_c = \alpha_x; \quad \alpha_x = \alpha_x + \alpha_{xu};$	
if $\min(\alpha_x, \alpha_y, \alpha_z) = \alpha_y$	
$p = p + (\alpha_y - \alpha_c)L\mathbf{f}[i][j][k]; \quad l = l + (\alpha_y - \alpha_c)L; \quad j = j + j_u; \quad \alpha_c = \alpha_y; \quad \alpha_y = \alpha_y + \alpha_{yu};$	
if $\min(\alpha_x, \alpha_y, \alpha_z) = \alpha_z$	
$p = p + (\alpha_z - \alpha_c)L\mathbf{f}[i][j][k]; \quad l = l + (\alpha_z - \alpha_c)L; \quad k = k + k_u; \quad \alpha_c = \alpha_z; \quad \alpha_z = \alpha_z + \alpha_{zu};$	
end while	
$\mathbf{g}_v[\text{threadIdx.x}][\text{blockIdx.x}][\text{blockIdx.y}] = p;$	
$\mathbf{L}_v[\text{threadIdx.x}][\text{blockIdx.x}][\text{blockIdx.y}] = l;$	

view. Each GPU thread is assigned to execute one ray-tracing process, and therefore the total number of threads required equals to the data size $N_d \times N_s$.

Note that there is a second output \mathbf{L}_v in the algorithm whose element corresponds to the total ray length within the whole image volume, i.e. $L_{i,v} = \sum_{j=1}^N h_{ij,v}$. The vector \mathbf{L}_v acts as the divisor required in OS-SART algorithm for computing the corrective value $c_{i,v}$ as shown in Eq. (5.14).

Voxel-wise implementation of the backprojection operator \mathbf{H}^T

Unlike the forward process, ray-driven backprojection algorithms are not straightforward to parallelize. Recall that the backprojection value for the j -th voxel from the v -th view is the sum of all detector elements reweighted by their intersection lengths between the voxel and the corresponding X-ray paths, or mathematically speaking, $bp[j] = \sum_{i=1}^{M_v} c_{i,v} h_{ij,v}$, where all the notations can be referred to Sec. 5.2.4.

Obviously it is not wise to traverse all the detector elements since the number of which are huge and most of $h_{ij,v}$ are zeros. One technique to facilitate the ray-driven backprojection is the boundary box or “shadow formation” technique [197, 123], where the eight corners of the perspective projected voxel form a convex shadow on the detector. The basic idea is illustrated in Fig. 5.10. The backprojection value for this voxel must come from the detector elements bounded by the convex shadow, which significantly reduces the number of projection data to query. Since we determine the shadows voxel by voxel, this method is referred to the “voxel-wise” implementation of the backprojection operator \mathbf{H}^T . Note that \mathbf{H}^T is the matched adjoint of the ray-driven forward-projection operator (Siddon’s method),

and should not be mistaken for the aforesaid “voxel-driven” backprojection approach which is used in FDK algorithm.

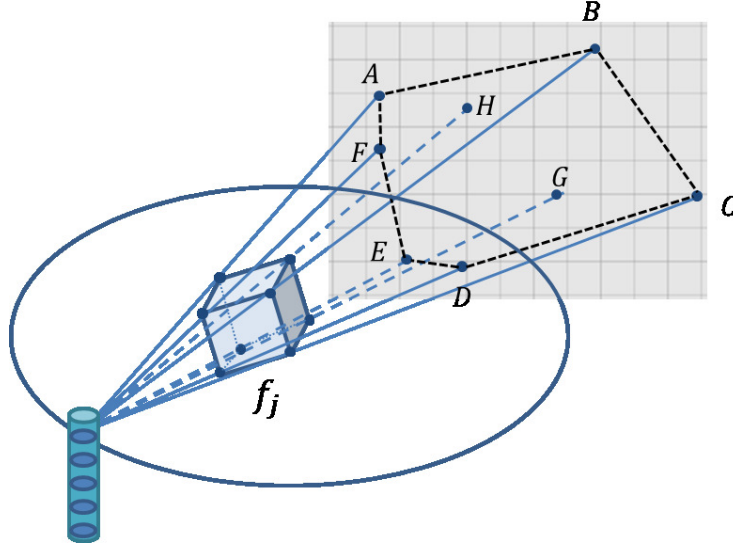


Figure 5.10: An illustration of the “shadow formation” which is used to determine the range of pixels for backprojection with respect to a given voxel.

However, this method still requires the traversal of detector elements inside the shadow. It is time consuming because the “shadow formation” is voxel-dependent and varies by voxels, thus the traversal cannot be configured in a parallel fashion. Particularly for TBCT reconstruction, there is an outer loop needed over the source array. The “shadow formation” for a specific voxel should be implemented every time when a source is on, which theoretically increases the computational burden by N_s times. In order to mitigate this problem, a prediction statement is needed to exclude those sources that won’t project the voxel within the range of the detector. An example is provided in Fig. 5.11, in which the upper and lower boundaries of the beams tell that only the source c and d can get the voxel projected within the detector range. All the other sources can be skipped before the “shadow formation” process starts, which can reduce the computational burden.

Table 5.5: The flowchart of the algorithm for voxel-wise backprojection operator (on kernel)

Algorithm 5.5	
kernel_backprojection<<< $(N_x, 1, 1), (N_y, N_z, N_s) >>> (\mathbf{c}_v, \theta, \tilde{\mathbf{f}}_v, \mathbf{w}_v)$	
Input: the view angle at the v -th subset θ , the corresponding corrective projection \mathbf{c}_v	
Output: the backprojected volume $\tilde{\mathbf{f}}_v$, the weight matrix \mathbf{w}_v	
Initialization: $x = x_{\min} + (\text{threadIdx.x})\Delta_v; \quad y = y_{\min} + (\text{blockIdx.x})\Delta_v; \quad z = z_{\min} + (\text{blockIdx.y})\Delta_v;$	
//***** exclude non-eligible sources *****	
$x_s = D_{so}; \quad y_s = 0; \quad z_s = z_{s,\min} + (\text{blockIdx.z})\Delta_v;$	
$z_{s,\text{lower}} = (z' - z_{d,\min})(D_{so} + D_{od})/D_{od} + z_{d,\min}$	
$z_{s,\text{upper}} = (z' - z_{d,\max})(D_{so} + D_{od})/D_{od} + z_{d,\max}$	
if $z_s < z_{s,\text{lower}}$ or $z_s > z_{s,\text{upper}}$	
exit;	
end if	
//***** shadow formation *****	
for $i = 0$ to 1	
for $j = 0$ to 1	
for $k = 0$ to 1	
$x' = x + (i - 0.5)\Delta_v; \quad y' = y + (j - 0.5)\Delta_v; \quad z' = z + (k - 0.5)\Delta_v;$	
$t = x' \cos \theta + y' \sin \theta; \quad s = -x' \cos \theta + y' \cos \theta;$	
$\min Y = \min(\min Y, (y' - y_s)(D_{od} + t)/(D_{so} - t) + s);$	
$\max Y = \max(\max Y, (y' - y_s)(D_{od} + t)/(D_{so} - t) + s);$	
$\min Z = \min(\min Z, (z' - z_s)(D_{od} + t)/(D_{so} - t) + z');$	
$\max Z = \max(\max Z, (z' - z_s)(D_{od} + t)/(D_{so} - t) + z');$	
end for	
end for	
end for	
$\min Y_index = \lceil (\min Y - y_{d,\min})/\Delta_d \rceil; \quad \max Y_index = \lceil (\max Y - y_{d,\min})/\Delta_d \rceil;$	
$\min Z_index = \lceil (\min Z - y_{d,\min})/\Delta_d \rceil; \quad \max Z_index = \lceil (\max Z - y_{d,\min})/\Delta_d \rceil;$	
//***** shadow traversal *****	
for $i = \min Y_index$ to $\max Y_index$	
for $j = \min Z_index$ to $\max Z_index$	
$x' = x \cos \theta + y \sin \theta; \quad y' = -x \cos \theta + y \cos \theta; \quad z' = z_{d,\min} + j\Delta_d;$	
$\alpha_{x0} = (x - 0.5\Delta_v - x')/(x_s - x'); \quad \alpha_{x1} = (x + 0.5\Delta_v - x')/(x_s - x');$	
$\alpha_{y0} = (y - 0.5\Delta_v - y')/(y_s - x'); \quad \alpha_{y1} = (y + 0.5\Delta_v - y')/(y_s - y');$	
$\alpha_{z0} = (z - 0.5\Delta_v - z')/(z_s - x'); \quad \alpha_{z1} = (z + 0.5\Delta_v - z')/(z_s - z');$	
$\alpha_{\min} = \max(\min(\alpha_{x0}, \alpha_{x1}), \min(\alpha_{y0}, \alpha_{y1}), \min(\alpha_{z0}, \alpha_{z1}))$	
$\alpha_{\max} = \min(\max(\alpha_{x0}, \alpha_{x1}), \max(\alpha_{y0}, \alpha_{y1}), \max(\alpha_{z0}, \alpha_{z1}))$	
if $\alpha_{\min} < \alpha_{\max}$	
$L = \ (x_s, y_s, z_s) - (x', y', z')\ ;$	
$bp = bp + (\alpha_{\max} - \alpha_{\min})L\mathbf{c}_v[i][j][\text{blockIdx.z}];$	
$l = l + (\alpha_{\max} - \alpha_{\min})L; \quad 111$	
end if	
end for	
end for	
$\tilde{\mathbf{f}}_v[\text{threadIdx.x}][\text{blockIdx.x}][\text{blockIdx.y}] = bp;$	
$\mathbf{w}_v[\text{threadIdx.x}][\text{blockIdx.x}][\text{blockIdx.y}] = l;$	

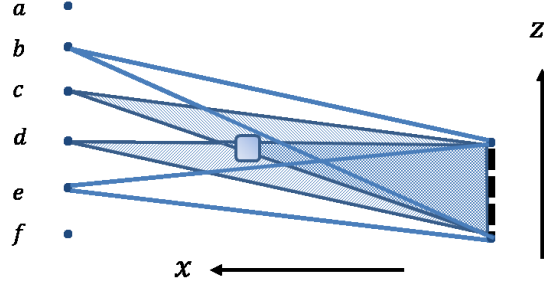


Figure 5.11: A prediction can be made to exclude those sources not involved in the back-projections for a specific voxel.

Algorithm 5.5 lists the pseudo code of TBCT backprojection kernel function by voxel-wise implementation on GPU devices. The outputs $\tilde{\mathbf{f}}_v$ and \mathbf{w}_v correspond to the two terms in Eq. (5.15) whose elements are expressed as:

$$\tilde{f}_{j,v} = \sum_{i=1}^{M_v} c_{i,v} h_{ij,v} \quad (j = 1, 2, \dots, N); \quad (5.19)$$

$$w_{j,v} = \sum_{i=1}^{M_v} h_{ij,v} \quad (j = 1, 2, \dots, N). \quad (5.20)$$

Due to the loop over the source array, the total number of threads required is the product of the number of voxels and the number of sources, which is almost larger by one order of magnitude than the number needed in CBCT backprojection. Consequently, as the number of sources increases, the computational burden linearly goes up regardless of the actual data size, i.e. the number of rays collected. In realistic TBCT system designs, the number of detector rows actually can be greatly reduced due to the use of multiple sources, so the data dimension is usually comparable to CBCT. In order to save reconstruction times especially when the source array is large, an alternative implementation strategy whose computing times depend on data size ($N_d N_s$) rather than the product of image size and source array size ($N_x N_y N_z N_s$) is highly desirable.

Pixel-wise implementation of the backprojection operator \mathbf{H}^T

Recall the backprojection formula $bp[j] = \sum_{i=1}^{M_v} c_{i,v} h_{ij,v}$, where j represents the index of voxel to be updated, v indicates the v -th view angle, and $c_{i,v}$ is the corrective value corresponding to the i -th ray or projection data. Since the system matrix \mathbf{H}_v is sparse, the brutal summation involves a lot of zero-valued $h_{ij,v}$, which is unrealistic for computing. The aforesaid boundary box technique is one of the methods used to efficiently determine those non-trivial i when the voxel index j is fixed. Now we are looking for an alternative strategy so that the non-trivial voxel index j can be efficiently determined when the i -th ray is fixed.

The ray-driven forward-projection operation (Siddon's method) has such an attractive property that when tracing the i -th ray we are finding out all the voxels j that provide non-trivial contributions to this ray, or mathematically $h_{i,j,v} \neq 0$. More importantly, all the $h_{ij,v}$ are readily available during the forward process. So it is straightforward and should be an efficient way to directly backproject $c_{i,v}$ along the i -th ray path to update all the voxels involved. Then a loop over all the collected rays can ensure every voxel completely updated by all non-trivial $h_{ij,s}$.

This new backprojection strategy is illustrated in Fig. 5.12 in which with the given i -th ray and the corresponding $c_{i,v}$, a similar ray-tracing process is conducted. But this time, we do not read from the image volume but write to it by adding each voxel value along the ray path with $c_{i,v} h_{ij,v}$. Since this method can be parallelly launched for all the rays, or equivalently driven by pixels on the detector, it is referred to as the pixel-wise implementation of the backprojection operator. Unlike the voxel-wise implementation, if the data size $N_d N_s$ is fixed, the computational burden of pixel-wise implementation won't go up with the increase of number of sources N_s .

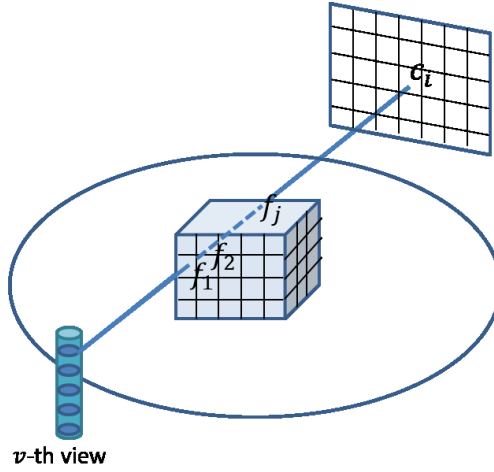


Figure 5.12: An illustration of the pixel-wise implementation of the backprojection. A similar ray-tracing process is conducted to update all the voxels along the ray.

Though Siddon’s ray-tracing model is optimal for GPU implementation, however, there is a significant limitation that prevents the backprojection from running as fast as the forward process. Since thousands of GPU threads are assigned to parallelly execute the ray tracing, there are high probabilities that one voxel is being updated simultaneously by multiple threads during the GPU runtime. This is called “race condition” in parallel programming and considered as a computational hazard that arises when multiple threads attempt to access the same memory location concurrently and at least one access is a write. Programs with race conditions may produce unexpected, seemingly arbitrary results. CUDA provides atomic functions (commonly called atomic memory operations) to enforce atomic accesses to device variables that may be accessed by multiple threads, which means all parallel threads are forced into a bottleneck executing the operation one at a time. Note that atomics are much slower than normal accesses, so the computing performance may degrade significantly when many threads attempt to perform atomic operations on a small number of memories.

Table 5.6: The flowchart of the algorithm for pixel-wise backprojection operator (on kernel)

Algorithm 5.6	
kernel_backprojection<<< $(N_{d,W}, 1, 1), (N_{d,W}, N_s, 1) >>> (\mathbf{c}_v, \theta, \tilde{\mathbf{f}}_v, \mathbf{w}_v)$	
Input: the view angle at the v -th subset θ , the corresponding corrective projection \mathbf{c}_v	
Output: the backprojected volume $\tilde{\mathbf{f}}_v$, the weight matrix \mathbf{w}_v	
Initialization:	
$x'_s = D_{so}; \quad y'_s = 0; \quad z_s = z_{s,\min} + (\text{blockIdx.y})\Delta_s;$ $x'_d = -D_{od}; \quad y'_d = y_{d,\min} + (\text{threaIdx.x})\Delta_d; \quad z_d = z_{d,\min} + (\text{blockIdx.x})\Delta_d;$ $x_s = x'_s \cos\theta + y'_s \sin\theta; \quad y_s = -x'_s \cos\theta + y'_s \sin\theta;$ $x_d = x'_d \cos\theta + y'_d \sin\theta; \quad y_d = -x'_d \cos\theta + y'_d \sin\theta;$ $c = \mathbf{c}_v[\text{threadIdx.x}][\text{blockIdx.x}][\text{blockIdx.y}]$	
Define: $\alpha_x(i) \equiv \frac{(x_{\min} + i\Delta_v) - x_s}{x_d - x_s}; \quad \alpha_y(i) \equiv \frac{(y_{\min} + j\Delta_v) - y_s}{y_d - y_s}; \quad \alpha_z(k) \equiv \frac{(z_{\min} + k\Delta_v) - z_s}{z_d - z_s};$ $\alpha_{x,\min} = \min(\alpha_x(0), \alpha_x(N_x)); \quad \alpha_{y,\min} = \min(\alpha_y(0), \alpha_y(N_y)); \quad \alpha_{z,\min} = \min(\alpha_z(0), \alpha_z(N_z));$ $\alpha_{x,\max} = \max(\alpha_x(0), \alpha_x(N_x)); \quad \alpha_{y,\max} = \max(\alpha_y(0), \alpha_y(N_y)); \quad \alpha_{z,\max} = \max(\alpha_z(0), \alpha_z(N_z));$ $\alpha_{\min} = (\alpha_{x,\min}, \alpha_{y,\min}, \alpha_{z,\min}); \quad // \text{entry point}$ $\alpha_{\max} = (\alpha_{x,\max}, \alpha_{y,\max}, \alpha_{z,\max}); \quad // \text{exit point}$	
if $\alpha_{\min} < \alpha_{\max}$ exit; // the ray does not fall into the range of the detector end if	
if $x_s < x_d$ $i_{\min} = [\phi_x(\alpha_{\min})]; \quad j_{\min} = [\phi_y(\alpha_{\min})]; \quad k_{\min} = [\phi_z(\alpha_{\min})]$ $i_{\max} = [\phi_x(\alpha_{\max})]; \quad j_{\max} = [\phi_y(\alpha_{\max})]; \quad k_{\max} = [\phi_z(\alpha_{\max})]$ else $i_{\min} = [\phi_x(\alpha_{\max})]; \quad j_{\min} = [\phi_y(\alpha_{\max})]; \quad k_{\min} = [\phi_z(\alpha_{\max})]$ $i_{\max} = [\phi_x(\alpha_{\min})]; \quad j_{\max} = [\phi_y(\alpha_{\min})]; \quad k_{\max} = [\phi_z(\alpha_{\min})]$ end if	
Define: $\alpha_{lu} \equiv \frac{\Delta_v}{\ (l_d - l_s)\ }; \quad l_u \equiv \begin{cases} 1 & \text{if } l_s < l_d \\ -1 & \text{else,} \end{cases}; \quad (l = x, y, z)$	
$i = i_{\min}; \quad j = j_{\min}; \quad k = k_{\min};$ $\alpha_c = \alpha_{\min}; \quad L = \ (x_s, y_s, z_s) - (x_d, y_d, z_d)\ ;$	
while $(\alpha_c < \alpha_{\max})$ if $\min(\alpha_x, \alpha_y, \alpha_z) = \alpha_x$ atomicAdd($\tilde{\mathbf{f}}[i][j][k], (\alpha_x - \alpha_c)Lc$); atomicAdd($\mathbf{w}[i][j][k], (\alpha_x - \alpha_c)L$); $i = i + i_u; \alpha_c = \alpha_x; \alpha_x = \alpha_x + \alpha_{xu};$ if $\min(\alpha_x, \alpha_y, \alpha_z) = \alpha_y$ atomicAdd($\tilde{\mathbf{f}}[i][j][k], (\alpha_y - \alpha_c)Lc$); atomicAdd($\mathbf{w}[i][j][k], (\alpha_y - \alpha_c)L$); $j = j + j_u; \alpha_c = \alpha_y; \alpha_y = \alpha_y + \alpha_{yu};$ if $\min(\alpha_x, \alpha_y, \alpha_z) = \alpha_z$ atomicAdd($\tilde{\mathbf{f}}[i][j][k], (\alpha_z - \alpha_c)Lc$); atomicAdd($\mathbf{w}[i][j][k], (\alpha_z - \alpha_c)L$); $k = k + k_u; \alpha_c = \alpha_z; \alpha_z = \alpha_z + \alpha_{zu};$ end while	

Because the execution order of threads on GPU is unpredictable and uncontrollable, it is difficult to estimate the severity of race condition or the time cost for atomic operations during the pixel-wise backprojection. One has to test the computational performance case by case in order to compare with the alternative implementation strategy, which will be discussed in the following sections. Algorithm 5.6 shows the pseudo code of TBCT backprojection kernel function by pixel-wise implementation on GPU devices. The definitions of the input and output are the same as those in Algorithm 5.5. One should keep in mind that the two algorithms execute exactly the same backprojection operation \mathbf{H}^T , but implemented with different strategies.

5.3.4 Multi-GPU implementation of the reconstruction algorithms

Along with the efforts to improve the structural aspects of the parallel reconstruction algorithms, there is also an overwhelming trend shifting toward multi-GPU implementations for improved time performance. When the computational load is large or when the working set exceeds a single GPU's memory, the multi-GPU solution is preferred. CUDA programming and the NVIDIA GPU architecture support host/device concurrency, which means the codes on CPU and on GPU, and the codes on different GPUs, are executed simultaneously. Current GPU under control can be freely switched while asynchronous calls (kernels, memcpy) are running. This technique holds great promise of further speeding up the computation if the work load can be evenly distributed among multiple GPUs.

As discussed in Sec. 5.3.3 and Sec. 5.3.3, for TBCT reconstruction, both the single-GPU-enabled voxel- and pixel-wise backprojections are still anticipated to be computationally burdensome. In order to achieve even faster reconstruction speed, a multi-GPU scheme is

proposed in this section. Without loss of generality, the original 3D vector \mathbf{f} is equally divided into four sub-volumes that are distributed among four GPUs ($id = 0, 1, 2, 3$), respectively, denoted as \mathbf{f}^{id} . Typically for TBCT, dividing the volume along the z -axis is an optimal plan. The reason is that the source array also stretches along z direction, so this plan minimizes the number of rays intersecting with each individual sub-volume. Note that the number of GPUs can be any quantity not limited to four. The scheme can be readily extended by using additional GPUs.

A flowchart illustrating the multi-GPU-based TBCT reconstruction algorithm is shown in Fig. 5.13. It describes the details regarding the implementation of Eq. (5.16) which is the most important step in the OS-SART-FISTA-TV framework.

- **Projection step:** At the v -th view angle, each GPU launches *forward_kernel* to project the corresponding 1/4 sub-volume \mathbf{f}^{id} , simultaneously computing the projection $\mathbf{g}_v^{id} \in \mathbb{R}^{M_v}$, as well as the ray length matrix $\mathbf{L}_v^{id} \in \mathbb{R}^{M_v}$.
- **Correction step:** All \mathbf{g}_v^{id} and \mathbf{L}_v^{id} are transferred to the host memory and sum up, respectively, thus forming the complete vectors

$$\begin{aligned}\mathbf{g}_v &= \mathbf{g}_v^0 + \mathbf{g}_v^1 + \mathbf{g}_v^2 + \mathbf{g}_v^3, \\ \mathbf{L}_v &= \mathbf{L}_v^0 + \mathbf{L}_v^1 + \mathbf{L}_v^2 + \mathbf{L}_v^3.\end{aligned}\tag{5.21}$$

Therefore based on Eq. (5.14), the 2D corrective matrix \mathbf{c}_v is computed as

$$c_{i,v} = \frac{g_{i,v}^{\text{data}} - g_{i,v}}{L_{i,v}}, \quad (i = 1, 2, \dots, M).\tag{5.22}$$

Then, \mathbf{c}_v is copied to the global memory of all GPUs for the next step.

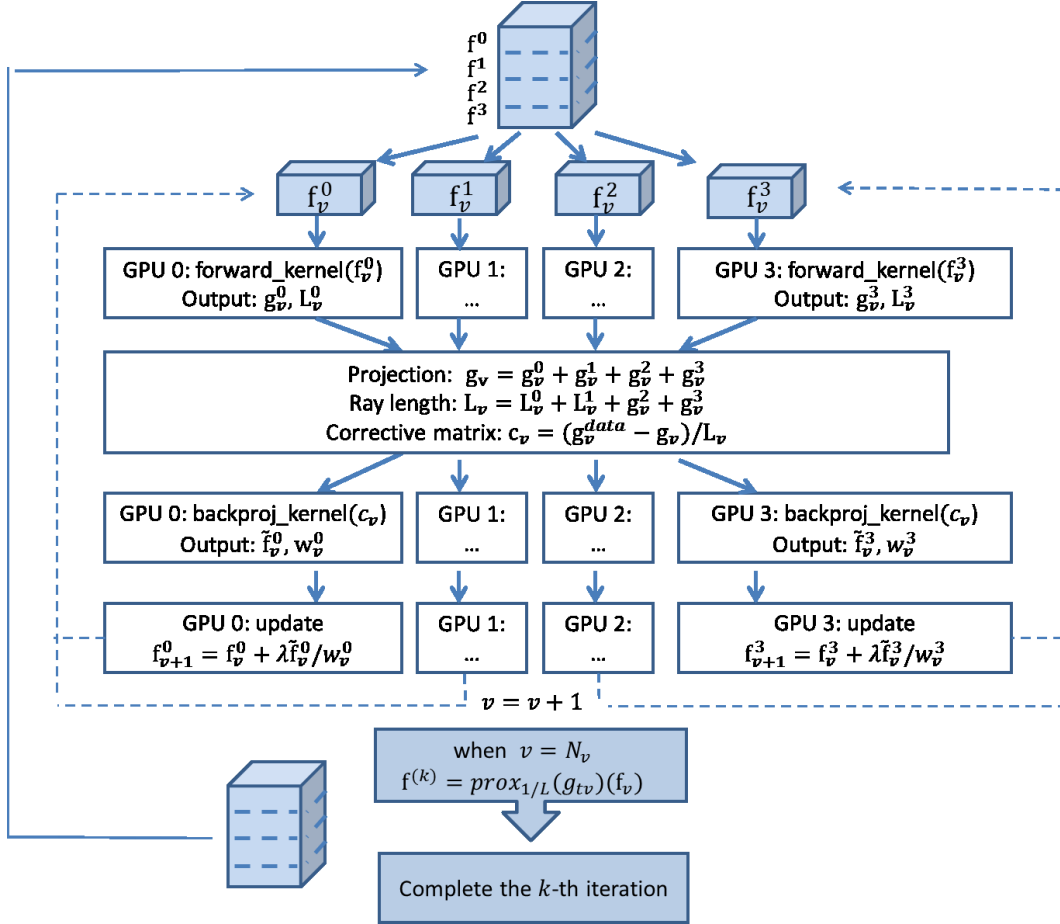


Figure 5.13: A schematic of 4-GPU implementation for OS-SART-FISTA-TV algorithm.

- **Backprojection-update step:** Each GPU launches *backprojection_kernel* to simultaneously compute the backprojected sub-volume $\tilde{\mathbf{f}}_v^{id} \in \mathbb{R}^{N/4}$ and the weight matrix $\mathbf{w}_v^{id} \in \mathbb{R}^{N/4}$, whose elements are mathematically described as

$$\begin{aligned}\tilde{f}_{j,v}^{id} &= \sum_{i=1}^{M_v} c_{i,v} h_{ij,v}^{id}, \\ w_{j,v}^{id} &= \sum_{i=1}^{M_v} h_{ij,v}^{id}, \quad (j = 1, 2, \dots, N/4).\end{aligned}\tag{5.23}$$

Then based on Eq. (5.15), the id -th sub-volume needs to be updated as

$$f_{j,v+1}^{id} = f_{j,v}^{id} + \gamma_v \frac{\tilde{f}_{j,v}^{id}}{w_{j,v}^{id}}.\tag{5.24}$$

Then it requires to check if all subsets have been accessed. If not, then update $v = v + 1$ and repeat the projection-correction-backprojecion-update procedure until v reaches N_v . If so, move on for the rest steps listed in Algorithm 5.2 to complete one iteration.

- **TV-regularization step:** When all the data subsets have been accessed for updating the image volume, the obtained sub-volumes are combined to form a whole volume \mathbf{f} as the input of the TV-proximal problem defined in Eq. (5.10) and Algorithm 5.2. The output will be a TV-regularized image with sharper boundaries and less noise. The FGP algorithm[111, 176] used for solving TV-proximal problem is also suitable for parallel computing due to the desirable property that all the operations in FGP are performed in an element-wise manner. That indicates that each element of the input image can be updated independently by use of a GPU thread, which efficiently exploits GPU parallelism and can be implemented in a minimal time compared with the forward-projection and back-projection operators.

The computation time for the ray-driven forward-projection operator when four GPUs are employed is approximately reduced by one quarter compared with that by single GPU implementation. This is because for an individual sub-volume with one fourth of the original size, the number of rays that pass through the sub-volume can be approximately reduced by half; moreover, the average intersection length of a ray within the sub-volume can also be approximately reduced by half. Similar analysis and conclusion can be applied to the pixel-wise backprojection which almost follows the same steps as the forward process. In terms of the voxel-wise backprojection, since the number of voxels for a sub-volume is only one quarter left, it is natural to expect a reduction in time by one fourth. The computation time for the correction step is negligible as only simple arithmetic operations are involved for a small 2D matrix. Other overhead and communication time between the host and the device is minimal.

As a conclusion, the time reduction factor by adopting a multi-GPU scheme to solve the proposed PWLS-TV problem in the context of TBCT reconstruction is approximately equal to the number of GPUs employed, no matter what type of backprojection implementation involved. This feature is highly attractive and suggests that reconstruction times can be further reduced by using additional GPUs, thus able to promote the applications of TBCT imaging system.

5.4 Computer simulation studies

5.4.1 Numerical phantom and system geometries

Numerical simulations were conducted to investigate the performance of TBCT reconstruction algorithms. In our numerical simulations, a modified Shepp-Logan phantom was employed, and the image volume size is $512 \times 512 \times 512$. The source-object distance D_{so} and the object-detector distance D_{od} are assigned the same so that the magnification factor is 2. A monochromatic x-ray source array and equal-spacing detector was assumed. The full scan projection data set was evenly acquired with $N_v = 360$ views on a circular scanning trajectory. The geometrical illustration and parameter notations are the same as those in Fig. 5.4.

At each view angle and for a given source, a ray-tracing model was applied to analytically compute the exact projection of the phantom in size $N_{d,W} \times N_{d,H}$ which is the product of the number of element columns and number of element rows. In this study, $N_{d,W} = 1024$ is fixed, but $N_{d,H}$ varies as the number of sources N_s by keeping $N_{d,H} \times N_s = 1024$. For example, when $N_s = 1$ the element rows will be 1024, which is equivalent to a CBCT setup; when $N_s = 2$ the element rows will be 512; when $N_s = 64$ the element rows will be 16. As a result, the dimension of a whole TBCT dataset $\mathbf{g} \in \mathbb{R}^M$ remains unchanged throughout since $M = N_{d,W}N_{d,H}N_sN_v$ is fixed.

The specification of N_s will be provided along with the descriptions of each individual numerical study in the following sections. The z -axis range of the source array is specified by the top source position $z_{s,\max}$ and the bottom source position $z_{s,\min}$. All the sources were evenly distributed along z -axis between $z_{s,\max}$ and $z_{s,\min}$. The top and bottom positions

determined the minimum source range while the whole reconstructed volume can still fit within the tetrahedrons formed by all valid rays.

5.4.2 Hardware specifications

All implementations were tested on the platform consisted of dual quad-core Intel(R) Xeon(R) CPUs with a clock speed 1.2 GHz. The GPU-based implementations of the FDK and iterative algorithms were tested on NVIDIA Tesla K20c GPUs.

5.4.3 Computational accuracy for full-view datasets

Considering the reconstruction of horizontal (transverse) planes is trivial since TBCT's scanning geometry is almost equivalent to CBCT, we are particularly interested in the reconstructed vertical (sagittal or coronal) planes as the elongated distribution of X-ray sources may bring different reconstruction performances along z -axis. It is well known that CBCT may suffer from the large cone-angle artifacts that usually appear in the top and bottom regions of the reconstructed images. This can be explained by the Fourier slice theorem that predicts that a large projection angle leads to the information loss in the measurements along k_z , where k_z denotes the spatial frequency axis that is conjugate to z . Though TBCT also has the cone-angle problem, the situation may vary depending on the number of sources and their positions. Figure (5.14) illustrates four TBCT systems which employ a 1-, 2-, 8- and 64-source array, respectively. As pointed previously, the number of detector element rows correspondingly changes so that the dimensions of system matrices \mathbf{H} and the sizes of measurements \mathbf{g} , as well as all the other geometrical parameters, are kept the same among

the four cases in order to conduct a fair comparison. It can be observed from Fig. 5.14 that the cone-beam angles of TBCT are different ray by ray, and case by case.

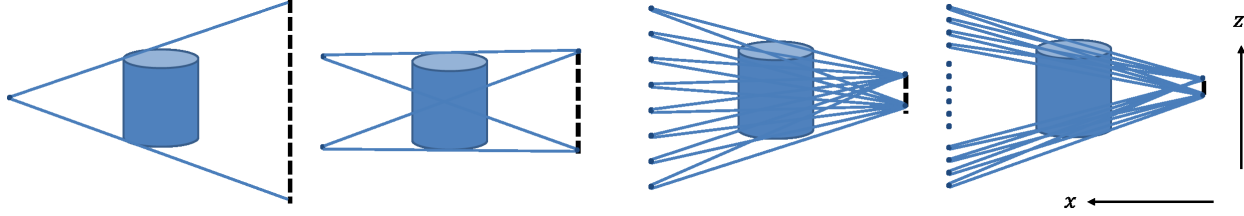


Figure 5.14: Four different TBCT system designs with $N_s = 1, 2, 8$ and 64 , respectively.

In the simulation study, the values of D_{so} and D_{od} were set by making the cone angle around 20 degree for the case $N_s = 1$ (i.e. CBCT), and the same D_{so} and D_{od} values were applied to the other designs. Images of the central sagittal plane reconstructed by use of FDK w/o weights, FDK w/ inverse weights, non-regularized iterative algorithm (PLS) and TV-regularized iterative algorithm (PWLS-TV), are displayed in Fig (5.15). The colormap and colorbar were adjusted so that the artifacts are visible and prominent in an exaggerated way. The relative error (RE) defined by $E(\mathbf{f}) = \|\mathbf{f}^{\text{recon}} - \mathbf{f}^{\text{true}}\|_2 / \|\mathbf{f}^{\text{true}}\|_2$, where $\mathbf{f}^{\text{recon}}$ and \mathbf{f}^{true} denote the reconstructed and true phantom image, was also computed and labeled along with the corresponding image. The small values of REs indicate that the reconstructed image is close to the true phantom. Generally, the four methods rank higher one by one in terms of RE approximately by one order of magnitude. The following observations will be discussed:

- The conventional FDK algorithm without proper weighting functions leads to a severe data redundancy problem. The abnormal stripes correspond to those overlapping regions being updated by more rays than the surrounding areas. The proposed simple weighting method in the image domain significantly alleviates this problem and produces normal reconstructed images.

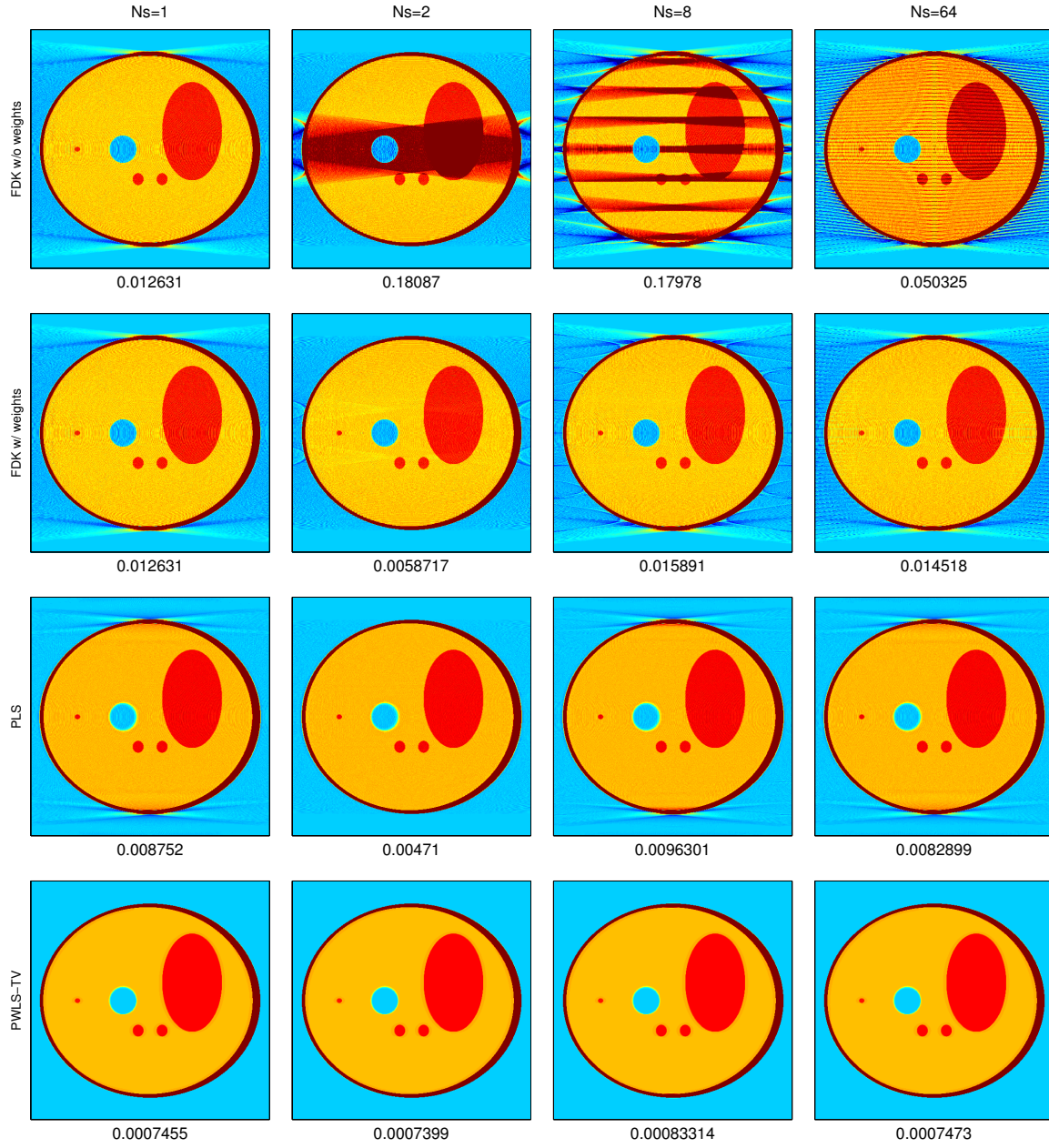


Figure 5.15: The central vertical slices of the reconstructed images for full-view dataset $N_v = 360$

- The cone-angle artifacts can also occur in reconstructed TBCT images when the incident beam angles are large enough, typically in the top and bottom of the volume. It is interesting to note that when $N_s = 2$ the artifacts disappear from the two poles but instead appear around the equator. When the number of sources keeps increasing, the z -axis reconstruction performance approaches to CBCT again. All of these observations are consistent with the Fourier slice theorem and can be predicted from the geometrical illustrations of the irradiating beams shown in Fig. 5.14. This finding also implies that one can adjust the local reconstruction performance by manipulating the sources' positions in order to minimize cone-angle artifacts at selected elevations. This is a useful feature and a potential advantage of TBCT, however, beyond the scope of this study.
- The images reconstructed by use of the non-regularized iterative algorithm contain fewer artifacts, less noise and better accuracy than those reconstructed by use of the FDK algorithm both inside and outside the phantom. The images produced by iterative algorithm without regularizations correspond to the solutions of a penalized least squares (PLS) estimator as shown in Eq. (5.2) in which the regularization parameter is set as zero. However, the PLS estimator cannot eliminate the cone-angle artifacts because the linear operator theory reveals that the estimate must lie in the measurable space of the image domain, while the cone-angle artifacts originate from the k_z information loss in the measurements. That means there is a part of the object referred to as “null component”, from the perspective of linear operator theory, that can never be recovered from the knowledge of system matrix \mathbf{H} only.
- The images reconstructed by use of the TV-regularized iterative algorithm contain even fewer artifacts, smoother background and higher structure contrast, outperforming all the other algorithms. Most importantly, the cone-angle artifacts are also eliminated by use

of this method. These images correspond to the solutions of the PWLS-TV estimator as shown in Eq. (5.2) by empirically choosing a proper regularization parameter. Because reconstructing the structures with insufficient k_z measurements corresponds to an ill-conditioned inverse problem, a regularized solution has to be computed. Regularization methods that promote object sparsity are ubiquitous in the modern image reconstruction literature, among them the total variation (TV) is a most effective one that has been employed widely, especially in the cases when the gradient map of the image is considered sparse. Note that the design of a working regularization strategy is influenced by many factors, including the characteristics of the object to be estimated or other prior knowledge. So for different imaging tasks, alternative regularizations other than TV may apply.

5.4.4 Computational accuracy for few-view datasets

The datasets with progressively reduced number of views $N_v = 360, 180, 90, 45$ are tested in this study. All the projections were evenly distributed over $[0, 2\pi)$. The number of sources was fixed as $N_s = 64$, and all the other geometrical parameters were the same as described in Sec 5.4.1. Images of the same vertical plane reconstructed by use of FDK, the non-regularized iterative algorithm (PLS) and the TV-regularized iterative algorithm (PWLS-TV) are shown in Fig. 5.16, along with the corresponding relative error labeled under each image.

As expected, when the amount of measurement data are reduced, the reconstruction accuracy decreases in terms of RE in all cases. The image quality corresponding to the first two algorithms degraded significantly, but presented quite different features. The FDK algorithm tends to produce high-frequency streaking artifacts, while the PLS estimator tends

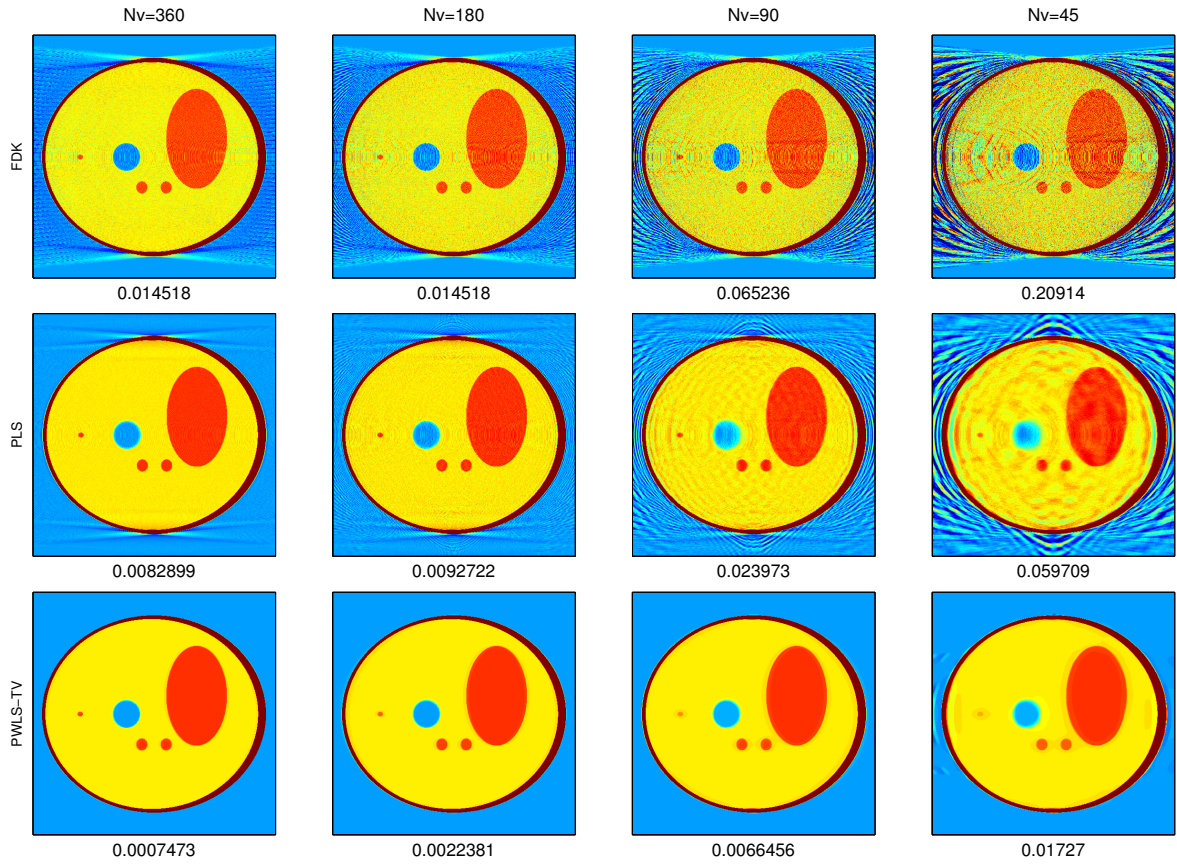


Figure 5.16: The central vertical slices of the reconstructed images for few-view dataset $N_v=360, 180, 90$ and 45 .

to generate blurry structures. More analysis regarding the few-view image reconstruction of the FBP-type algorithm and iterative algorithm can be found in the previous work[59]. However, the images reconstructed by use of TV-regularized iterative algorithm did not suffer from an obvious degradation even the dataset was reduced by one eighth, suggesting the promising potential of lowering the radiation dose during the data acquisition by minimizing the projections required for a specific imaging task. The reduction in imaging times is particularly important for TBCT as the sequential emission of X-ray sources takes longer time than other imaging setups like CBCT.

5.4.5 Computational efficiency for GPU implementation

Fixing the image size $N = 512^3$ and the data size $M = 1024^2 \times 360$, the computational performances of the FDK algorithm and iterative algorithm with different backprojection implementations were evaluated by varying the number of sources N_s , and correspondingly with a varying number of detector element rows $N_{d,H}$. Consistent with the previous settings, the product of $N_{d,H}$ and N_s was set as 1024.

The FDK algorithm invokes just a one-time backprojection step which is implemented in a “voxel-wise” manner. However, there is another outer loop over the source array, so the computational time is proportional to the number of sources. Figure 5.17 plots the image reconstruction times by use of the FDK algorithm and single-GPU implementation for different values of N_s . When $N_s = 1$, which corresponds to a special case equivalent to CBCT, the reconstruction can be done in 3.6 seconds. When N_s increases to 128, the computational performance degenerates to as slow as 186 seconds.

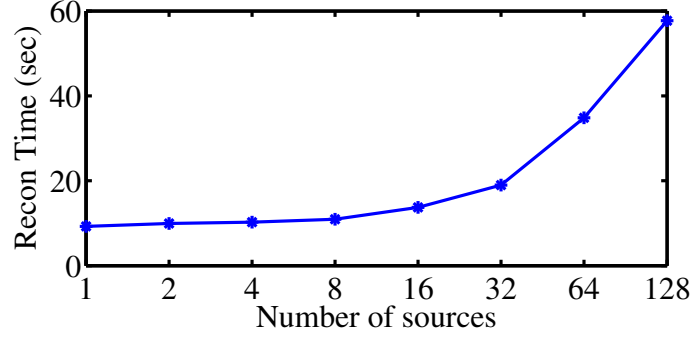


Figure 5.17: single-GPU FDK reconstruction times. $N = 512^3$; $M = 1024^2 \times 360$.

For iterative algorithm, the forward and backprojection computational times using a single GPU are plotted in Fig. 5.18. The forward operator \mathbf{H} is considered efficient and takes a constant time (around 16 seconds) because the computational performance of Siddon's ray-tracing method just depends on the data size M . The two implementations of the back-projection operator \mathbf{H}^T , as expected, behave quite differently. The voxel-wise implementation runs fast when the number of sources is small but the time linearly grows as N_s increases, similarly to the behavior of FDK. Alternatively, the pixel-wise implementation runs slowly as it has to employ atomic memory access in order to avoid race condition, but the computational performance does not change with N_s . So the pixel-wise backprojection times are almost constant over different N_s , which is similar to the behavior of the forward projection. The whole computational time for a complete iteration can be considered as the sum of the times for forward projection and backprojection, while the other steps can be negligible.

Computational performance improvement for iterative algorithm using a multi-GPU scheme is plotted in Fig. 5.19. As anticipated in Sec. 5.3.4, the time reduction factor by adopting a multi-GPU scheme is approximately equal to the number of GPU employed, no matter what type of backprojection implementation is used. For example, when the source number is 64,

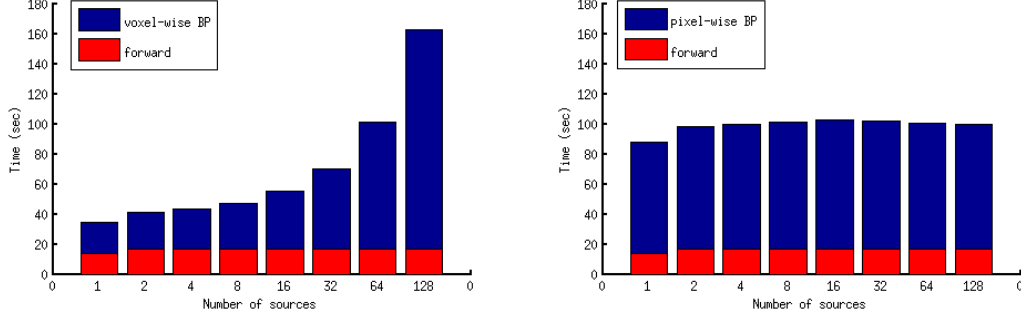


Figure 5.18: single-GPU forward and backprojection times (per iteration)

the 4-GPU configuration can reduce the reconstruction time per iteration from 100 seconds to around 25 seconds for both backprojection implementations. Note that $N_s = 64$ is observed as a threshold, beyond which the pixel-wise backprojection implementation is preferred in terms of computational efficiency and under which the voxel-wise version is preferred. For other image and data scales, the iterative algorithm presents similar computational properties and trends. Figure 5.20 shows the reconstruction times for the system matrix dimension $N = 256^3$ and $M = 512^2 \times 360$. All the times are approximately one eighth of those in Fig. 5.19, and the threshold for choosing a faster backprojection implementation is around $N_s = 32$.

The total reconstruction times by use of iterative algorithm can be estimated from the reconstruction time per iteration multiplying the number of iterations needed for achieving convergence. In order to investigate the convergence rate yielded by the OS-SART-FISTA-TV algorithm, the relative error (RE) values were plotted as a function of iteration number. The SL phantom datasets with 360, 180, 90 and 45 projections were selected, for all of which $N_s = 64$. A few conclusions can be drawn from Fig. 5.21. First, the reconstruction with full-view data can converge to a more accurate image (i.e. lower RE) than those with fewer data. Second, the reconstruction with full-view data converges more quickly than those with

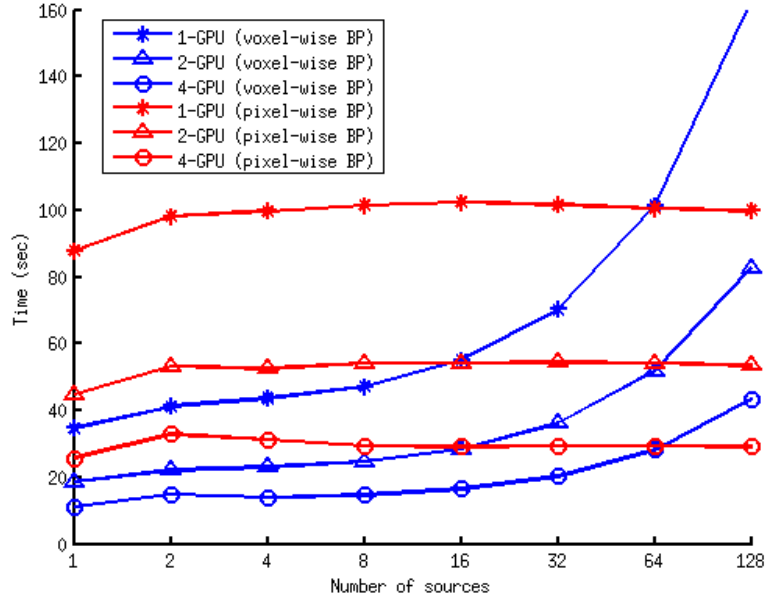


Figure 5.19: Multi-GPU reconstruction times for iterative algorithm (per iteration). $N = 512^3$; $M = 1024^2 \times 360$.

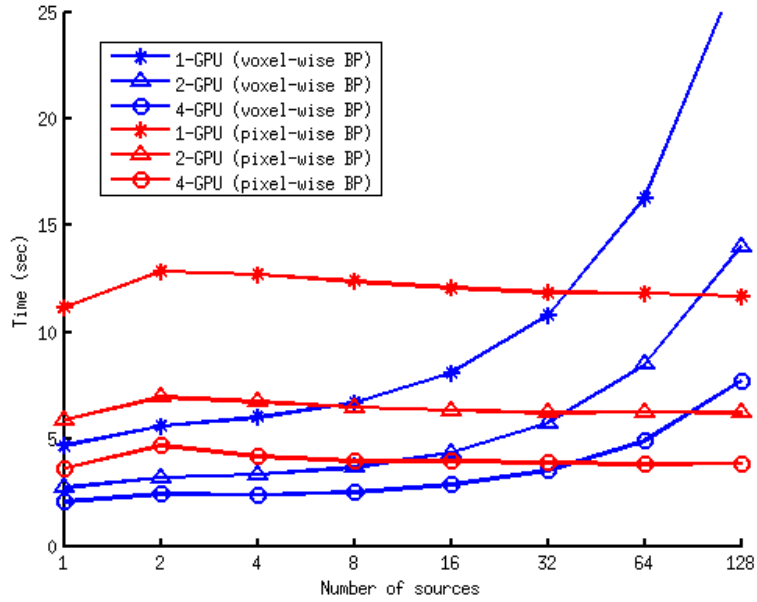


Figure 5.20: Multi-GPU reconstruction times for iterative algorithm (per iteration). $N = 256^3$; $M = 512^2 \times 360$.

fewer data. Typically, the convergence can be approximately achieved in 10 iterations for the dataset with 360 projections, while more than 20 iterations are required for the dataset with 45 projections. Third, the use of TV regularization does not change the convergence rate but can significantly improve the converged results.

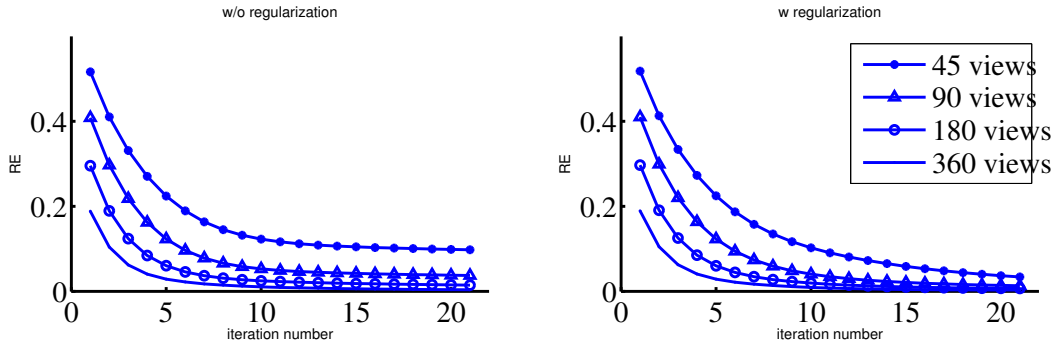


Figure 5.21: Relative error as a function of iteration numbers for OS-SART-FISTA-TV algorithm

5.5 Experimental studies

A bench-top TBCT system was previously developed by Zhang, et al[178]. Figure 5.22 shows a picture of the whole system which comprises a multi-pixel field emission x-ray tube (MPFEX), a multi-slot collimator, a 5-row curved CT detector and a rotation stage. The MPFEX tube is placed vertically, and the detector assembly is placed horizontally. The distances from the stage rotation center to the central emitter of the tube and to the center of the detector array are 82.5 cm and 62.5 cm, respectively.

Figure. 5.23 shows the geometrical and electrical diagram of the system. The source tube contains 75 cathodes, and all the source elements are aligned vertically with 4 mm spacing. The MPFEX tube can provide a very high source switching frequency of approximately 1

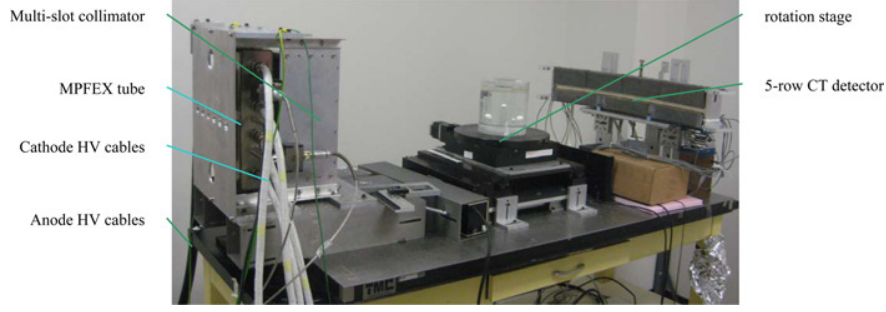


Figure 5.22: A picture of the bench-top TBCT system.

MHz[180]. The detector array consists of 11 detector boards and each board includes five 5×5 photodiode arrays and matching scintillator arrays. So the detector is considered to contain 275 columns in width and 5 rows in height. Each pixel size is $2.54 \times 2.54 \text{ mm}^2$. The reconstruction code is slightly modified to match the profile of the curved detector in the beam's-eye-view (BEV) direction.

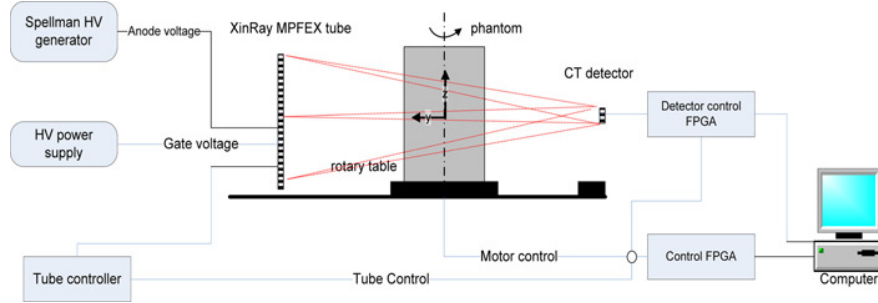


Figure 5.23: A diagram of the bench-top TBCT system illustrating the geometry and electrical connection.

A pig's head was scanned using the TBCT bench top system described above[81]. 360 projections over $[0, 2\pi)$ were acquired. The reconstructed images of a sagittal, a coronal and a transverse plane are displayed in Fig. 5.24 by use of FDK and iterative algorithm. For iterative algorithm, the iteration number was set as 20 and the TV regularization parameter was empirically selected as $\lambda = 50$. The reconstructed volume was $256 \times 256 \times 128$ with the voxel size 1.5 mm. Based on the analysis in Sec. 5.4.5, the pixel-wise backprojection

implementation is more computational efficient. The total reconstruction time to achieve convergence was therefore approximately two minutes for 360-view dataset and 30 seconds for 90-view dataset.

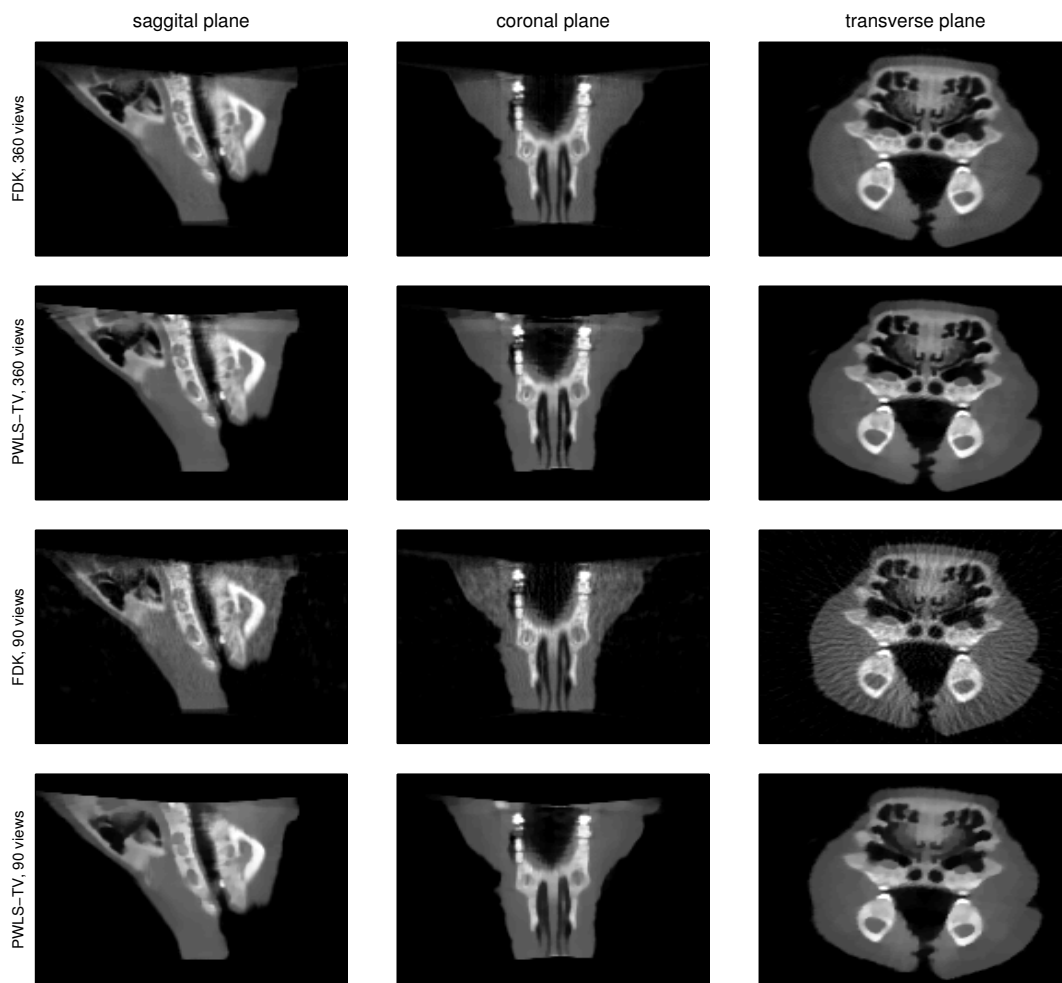


Figure 5.24: Reconstructed pig-head images for an experimental dataset.

With no image to use as a ground truth, the reconstructions were qualitatively evaluated. For the full-view dataset, the two algorithms produce close results, with slightly better contrast seen in the iterative reconstruction. When the amount of data was reduced to one quarter,

FDK produced significant streaking artifacts, while the iterative algorithm was still able to reconstruct reliable images with most structural features preserved.

5.6 Conclusion

Tetrahedron beam computed tomography (TBCT) is a novel volumetric imaging system with a modified geometrical design compared to the commonly used cone-beam computed tomography (CBCT). It holds great promise of mitigating the photon-scattering problem, and features flexible geometrical settings that can facilitate imaging guided radiation therapy (IGRT). Though a few preliminary image reconstruction results came along with the invention of TBCT, however, a careful investigation of the reconstruction algorithms specific to the TBCT geometries has not been conducted.

The analytical reconstruction method can be derived from the conventional FDK algorithm that is widely used for CBCT. However, the previously published TBCT-FDK results presented exaggerated cone-angle artifacts, implying that the data redundancy problem might not have been carefully addressed. In this work, we improved the analytical reconstruction method by introducing proper weighting functions in the TBCT image domain. More specifically, for a given image voxel, the only source-voxel ray that corresponds to the minimum cone angle should be given the priority weight among all the rays that contribute to the backprojection process. The weighting function can be fine tuned based on this rule of thumb and therefore achieves the balance between image accuracy and smoothness.

We also have implemented an advanced optimization-based approach to TBCT image reconstruction, which iteratively solves an optimization problem that minimizes the cost function

as indicated in Eq. 5.2. The developed reconstruction method utilizes the "FISTA" framework that assures fast convergence, and the incorporated total-variation regularization has the capability of suppressing data noise and mitigating data incompleteness. In terms of the forward imaging operator, a classical "ray-tracing" model was employed to implement the X-ray transform. In order to efficiently exploit the parallelism in GPU computing, we proposed different parallelization strategies for backprojection process in which the assignment of threads may vary depending on the number of sources employed in the system.

The reconstructed results from numerical and experimental dataset have demonstrated the good performances of the proposed TBCT reconstruction algorithms, in terms of both the image quality and computational efficiency. Basically, the regularized iterative algorithm outperforms the other methods in the cases when tomographic data is considerably noisy or incomplete. By use of the sufficiently-parallelized GPU code, the iterative reconstruction algorithm can be super fast, achieving a full convergence within 1 minute for reconstructing a 256^3 volumetric image.

Chapter 6

Summary

In this dissertation, we reviewed four different X-ray based imaging technologies: propagation-based phase-contrast (PB-XPC) tomosynthesis, differential X-ray phase-contrast tomography (D-XPCT), projection-based dual-energy computed radiography (DECR), and tetrahedron beam computed tomography (TBCT). System characteristics or optimized reconstruction methods were investigated for these novel imaging modalities. The contributions are summarized as following.

- We investigated a unique properties of propagation-based phase-contrast imaging technique when combined with the X-ray tomosynthesis. It can be derived from Fourier slice theorem that the XPC-induced high frequency components collected in the phase-contrast tomosynthesis data can be more reliably reconstructed. We have demonstrated that the fringes or boundary enhancement introduced by the phase-contrast effects can serve as an accurate indicator of the true depth position in the tomosynthesis in-plane image.
- We derived a sub-space framework to reconstruct resolution-enhanced images from few-view differential phase-contrast tomography data set. It was derived from Logan's

theorem that by introducing a proper mask, the high frequency contents of the image can be reliably reconstructed in a certain region of interest. A novel two-step reconstruction strategy was proposed in the work that can mitigate the risks of subtle structures being oversmoothed when the commonly used total-variation regularization is employed in the conventional iterative framework.

- We proposed a useful method to improve the quantitative accuracy of the projection-based dual-energy material decomposition. It was demonstrated in this work that applying a total-projection-length constraint along with the dual-energy measurements can achieve a stabilized numerical solution of the decomposition problem, thus overcoming the disadvantages of the conventional approach that was extremely susceptible to noise corruption. We also proposed two feasible water-bath and scout-scan ideas that can be used to practically implement the desired constraint.
- We described a modified filtered backprojection and iterative image reconstruction algorithms specifically developed for tetrahedron beam computed tomography. As opposed to the conventional CBCT geometry, the use of multiple X-ray sources in TBCT requires extra attentions to handle the data redundancy issue and the increased computational burden. Special parallelization strategies were designed to facilitate the use of multi-GPU computing, showing demonstrated capability of producing high quality reconstructed volumetric images with a super fast computational speed.

Appendix A

The derivation of the high-frequency subspace

Below we describe how Eq. (3.13) is derived, in which we claim $Wf_1 = Wf_{\text{null}} + \epsilon$, where f_1 is the solution of the optimization problem stated in Eq. (3.12), f_{null} is denoted as the null component of the object with respect to the D-XPCT imaging operator $\mathcal{H} = \mathcal{DR}$, and ϵ is the same error term as presented in Eq. (3.11).

Consider the optimization problem proposed in Eq. (3.12)

$$\begin{aligned} f_1 &= \underset{f}{\operatorname{argmin}} \|f\|^2 \\ \text{s.t. } \mathcal{H}f &= (C - 1)g. \end{aligned}$$

By use of the pseudo-inverse of the imaging operator, denoted as $\mathcal{H}^\#$, the solution of the above optimization problem can be expressed analytically as

$$\begin{aligned} f_1 &= \mathcal{H}^\#(C - 1)g \\ &= \mathcal{H}^\#Cg - \mathcal{H}^\#g. \end{aligned}$$

By use of the filter $C = \mathcal{H}\mathcal{R}^\dagger C_h$, as specified in Eq. (3.12), and the defined forward operator $\mathcal{H} = \mathcal{D}\mathcal{R}$, we can expand the above equation

$$\begin{aligned} f_1 &= \mathcal{H}^\# \mathcal{H} \mathcal{R}^\dagger C_h g - \mathcal{H}^\# g \\ &= (\mathcal{D}\mathcal{R})^\# (\mathcal{D}\mathcal{R}) \mathcal{R}^\dagger C_h g - \mathcal{H}^\# g \\ &= \mathcal{R}^\# \mathcal{D}^\# \mathcal{D} \mathcal{R} \mathcal{R}^\dagger C_h g - \mathcal{H}^\# g. \end{aligned}$$

In common situations where there is no truncation in the projection data, the derivative operator \mathcal{D} is actually invertible with the properly defined boundary conditions. Therefore, $\mathcal{D}^\# \mathcal{D}$ can be cancelled such that

$$\begin{aligned} f_1 &= \mathcal{R}^\# \mathcal{R} \mathcal{R}^\dagger C_h g - \mathcal{H}^\# g \\ &= \mathcal{R}^\dagger C_h g - \mathcal{H}^\# g, \end{aligned}$$

in which the identity $\mathcal{R}^\# \mathcal{R} \mathcal{R}^\dagger = \mathcal{R}^\dagger$ is a property for linear operators[12]. Note that $\mathcal{R}^\dagger C_h g$ is exactly the FBP image as indicated in Eq. (3.4). This establishes that

$$f_1 = \hat{f}_{\text{FBP}} - \mathcal{H}^\# g.$$

By applying the mask W to f_1 and using the conclusion $W \hat{f}_{\text{FBP}} = W f + \epsilon$ stated in Eq. (3.11),

$$\begin{aligned} W f_1 &= W \hat{f}_{\text{FBP}} - W \mathcal{H}^\# g \\ &= W f - W \mathcal{H}^\# g + \epsilon \\ &= W(f - \mathcal{H}^\# g) + \epsilon. \end{aligned}$$

Since the measurable component of the object f_{meas} is equivalent to $\mathcal{H}^\#g$,

$$\begin{aligned} Wf_1 &= W(f - f_{\text{meas}}) + \epsilon \\ &= Wf_{\text{null}} + \epsilon, \end{aligned}$$

which yields the conclusion in Eq. (3.13).

Appendix B

Conversion of linear attenuation coefficient to the combination of two basis materials

Deadlines Alvarez and Macovsky[5] stated that the linear attenuation coefficient μ of a given material and a photon energy E in the diagnostic range between 30 to 100 KeV can be expressed approximately as a linear combination of Compton scatter and photoelectric effect[5]:

$$\mu(E) = a_c f_{KN}(E) + a_p f_p(E). \quad (\text{B.1})$$

The material-dependent Compton coefficient $a_c = k_1 \rho Z/A$, where ρ is the mass density, Z and A are the atomic number and atomic weight, respectively, k_1 is a proportional constant. The material-dependent photoelectric coefficient $a_p = k_2 \rho Z^4/A$, where k_2 is another proportional constant. $f_{KN}(E)$ is the Klein-Nishana formula for Compton scatter, and $f_p(E) \approx (1/E)^3$, both of which are energy-dependent only.

Suppose there are two basis materials that have

$$\mu_{b1}(E) = a_{c1}f_{KN}(E) + a_{p1}f_p(E) \quad (\text{B.2})$$

$$\mu_{b2}(E) = a_{c2}f_{KN}(E) + a_{p2}f_p(E). \quad (\text{B.3})$$

By substituting Eq. (B.2) and (B.3) into Eq. (B.1), it comes to a useful conclusion that any material can be expressed as a linear combination of the two basis materials in terms of the linear attenuation coefficient:

$$\mu(E) = \alpha_1\mu_{b1}(E) + \alpha_2\mu_{b2}(E), \quad (\text{B.4})$$

where the two coefficients α_1 and α_2 are uniquely determined and do not depend on the energy:

$$\alpha_1 = (\alpha_c\alpha_{p2} - \alpha_p\alpha_{c2})/(\alpha_{c1}\alpha_{p2} - \alpha_{c2}\alpha_{p1}) \quad (\text{B.5})$$

$$\alpha_2 = (\alpha_c\alpha_{p1} - \alpha_p\alpha_{c1})/(\alpha_{p1}\alpha_{c2} - \alpha_{p2}\alpha_{c1}). \quad (\text{B.6})$$

References

- [1] Nist physical reference data library. <http://physics.nist.gov/PhysRefData/FFast/html/form.html>.
- [2] An online tool for the simulation of x-ray spectra. <http://www.oem-products.siemens.com/x-ray-spectra-simulation>.
- [3] Raymond J Acciavatti and Andrew DA Maidment. Oblique reconstructions in tomosynthesis. i. linear systems theory. *Medical physics*, 40(11):111911, 2013.
- [4] S. Akazawa. The scope of the Japanese information industry in the 1980s. In K. R. Brown, editor, *The challenge of information technology: Proceedings of the forty-first FID (Federation Internationale de Documentation) congress held in Hong Kong 13-16 September 1982*, pages 19–22, Amsterdam, New York, and Oxford, 1983. North Holland.
- [5] Robert E Alvarez and Albert Macovski. Energy-selective reconstructions in x-ray computerised tomography. *Physics in medicine and biology*, 21(5):733, 1976.
- [6] American Library Association, Young Adult Services Division, Services Statement Development Committee. Directions for library service to young adults. Chicago, 1978.
- [7] Mark A Anastasio, Daxin Shi, Francesco De Carlo, and Xiaochuan Pan. Analytic image reconstruction in local phase-contrast tomography. *Physics in Medicine and biology*, 49(1):121, 2004.
- [8] Anders H Andersen and Avinash C Kak. Simultaneous algebraic reconstruction technique (sart): a superior implementation of the art algorithm. *Ultrasonic imaging*, 6(1):81–94, 1984.
- [9] Alyssa A Appel, Jeffery C Larson, Alfred B Garson, Huifeng Guan, Zhong Zhong, Bao-Ngoc B Nguyen, John P Fisher, Mark A Anastasio, and Eric M Brey. X-ray phase contrast imaging of calcified tissue and biomaterial structure in bioreactor engineered tissues. *Biotechnology and bioengineering*, 112(3):612–620, 2015.
- [10] Gilberto Artioli. *Structural studies of the water molecules and hydrogen bonding in zeolites*. PhD thesis, University of Chicago, 1985.

- [11] Gary T Barnes, Richard A Sones, Mike M Tesic, Douglas R Morgan, and John N Sanders. Detector for dual-energy digital radiography. *Radiology*, 156(2):537–540, 1985.
- [12] Harrison H Barrett and Kyle J Myers. *Foundations of image science*. John Wiley & Sons, 2013.
- [13] Amir Beck and Marc Teboulle. Fast gradient-based algorithms for constrained total variation image denoising and deblurring problems. *Image Processing, IEEE Transactions*, 18.11:2419–2434, 2009.
- [14] Amir Beck and Marc Teboulle. A fast iterative shrinkage-thresholding algorithm for linear inverse problems. *SIAM journal on imaging sciences*, 2(1):183–202, 2009.
- [15] Junguo Bian, Jeffrey H Siewerdsen, Xiao Han, Emil Y Sidky, Jerry L Prince, Charles A Pelizzari, and Xiaochuan Pan. Evaluation of sparse-view reconstruction from flat-panel-detector cone-beam ct. *Physics in medicine and biology*, 55(22):6575, 2010.
- [16] Junguo Bian, Jiong Wang, Xiao Han, Emil Y Sidky, Lingxiong Shao, and Xiaochuan Pan. Optimization-based image reconstruction from sparse-view data in offset-detector cbct. *Physics in medicine and biology*, 58(2):205, 2012.
- [17] Francois Bochud, Craig Abbey, and Miguel Eckstein. Statistical texture synthesis of mammographic images with super-blob lumpy backgrounds. *Optics express*, 4(1):33–42, 1999.
- [18] Charles A Bouman and Ken Sauer. A unified approach to statistical tomography using coordinate descent optimization. *IEEE Transactions on image processing*, 5(3):480–492, 1996.
- [19] Jovan G Brankov, Miles N Wernick, Yongyi Yang, Jun Li, Carol Muehleman, Zhong Zhong, and Mark A Anastasio. A computed tomography implementation of multiple-image radiography. *Medical physics*, 33(2):278–289, 2006.
- [20] Alberto Bravin, Paola Coan, and Pekka Suortti. X-ray phase-contrast imaging: from pre-clinical applications towards clinics. *Physics in medicine and biology*, 58(1):R1, 2012.
- [21] Alberto Bravin, Paola Coan, and Pekka Suortti. X-ray phase-contrast imaging: from pre-clinical applications towards clinics. *Physics in medicine and biology*, 58(1):R1, 2013.
- [22] DS Brettelle and AR Cowen. Dual-energy digital mammography utilizing stimulated phosphor computed radiography. *Physics in medicine and biology*, 39(11):1989, 1994.

- [23] William R Brody, Glenn Butt, Anne Hall, and Albert Macovski. A method for selective tissue and bone visualization using dual energy scanned projection radiography. *Medical physics*, 8(3):353–357, 1981.
- [24] William R Brody, Douglas M Cassel, F Graham Sommer, LA Lehmann, Albert Macovski, Robert E Alvarez, Norbert J Pelc, Stephen J Riederer, and Anne L Hall. Dual-energy projection radiography: initial clinical experience. *American Journal of Roentgenology*, 137(2):201–205, 1981.
- [25] Karin Burger, Thomas Koehler, Michael Chabior, Sebastian Allner, Mathias Marschner, Andreas Fehringer, Marian Willner, Franz Pfeiffer, and Peter Noël. Regularized iterative integration combined with non-linear diffusion filtering for phase-contrast x-ray computed tomography. *Optics express*, 22(26):32107–32118, 2014.
- [26] Weixing Cai. *Feasibility study of phase-contrast cone beam CT imaging systems*. PhD thesis, University of Rochester, 2009.
- [27] Emmanuel J Candès and Michael B Wakin. An introduction to compressive sampling. *IEEE Signal Processing Magazine*, 25(2):21–30, 2008.
- [28] A Caponnetto and M Bertero. Tomography with a finite set of projections: singular value decomposition and resolution. *Inverse problems*, 13(5):1191, 1997.
- [29] H Neale Cardinal and Aaron Fenster. An accurate method for direct dual-energy calibration and decomposition. *Medical physics*, 17(3):327–341, 1990.
- [30] Dean Chapman, W Thomlinson, RE Johnston, D Washburn, E Pisano, N Gmür, Z Zhong, R Menk, F Arfelli, and D Sayers. Diffraction enhanced x-ray imaging. *Physics in medicine and biology*, 42(11):2015, 1997.
- [31] Jian-wen Chen, Hong-yi Gao, Ru-xian Li, Hui-jing Gan, Hua-feng Zhu, Hong-lan Xie, and Zhi-zhan Xu. X-ray phase contrast imaging. *PROGRESS IN PHYSICS-NANJING-*, 25(2):175, 2005.
- [32] Yujia Chen, Huifeng Guan, Charlotte K Hagen, Alessandro Olivo, and Mark A Anastasio. Single-shot edge illumination x-ray phase-contrast tomography enabled by joint image reconstruction. *Optics Letters*, 42(3):619–622, 2017.
- [33] Kihwan Choi, Jing Wang, Lei Zhu, Tae-Suk Suh, Stephen Boyd, and Lei Xing. Compressed sensing based cone-beam computed tomography reconstruction with a first-order method. *Medical physics*, 37(9):5113–5125, 2010.
- [34] Cheng-Ying Chou, Mark A Anastasio, Jovan G Brankov, Miles N Wernick, Eric M Brey, Dean M Connor Jr, and Zhong Zhong. An extended diffraction-enhanced imaging method for implementing multiple-image radiography. *Physics in medicine and biology*, 52(7):1923, 2007.

- [35] Keh-Shih Chuang and HK Huang. Comparison of four dual energy image decomposition methods. *Physics in Medicine and Biology*, 33(4):455, 1988.
- [36] B. G. F. Cohen. Human aspects in office automation. Technical Report NTIS, PB84-240738, National Institute for Occupational Safety and Health, Division of Biomedical and Behavioral Science, Cincinnati, 1984.
- [37] Mini Das and Zhihua Liang. Spectral x-ray phase contrast imaging for single-shot retrieval of absorption, phase, and differential-phase imagery. *Optics letters*, 39(21):6343–6346, 2014.
- [38] TJ Davis, D Gao, TE Gureyev, AW Stevenson, and SW Wilkins. Phase-contrast imaging of weakly absorbing materials using hard x-rays. *Nature*, 373(6515):595–598, 1995.
- [39] Bruno De Man and S Basu. Distance-driven projection and backprojection. In *Nuclear Science Symposium Conference Record, 2002 IEEE*, volume 3, pages 1477–1480. IEEE, 2002.
- [40] Bruno De Man and Samit Basu. Distance-driven projection and backprojection in three dimensions. *Physics in medicine and biology*, 49(11):2463, 2004.
- [41] Kai Deng, Cong Sun, Cheng Liu, and Rui Ma. Initial experience with visualizing hand and foot tendons by dual-energy computed tomography. *Clinical imaging*, 33(5):384–389, 2009.
- [42] PC Diemoz, M Endrizzi, CK Hagen, C Rau, A Bravin, RD Speller, IK Robinson, and A Olivo. Edge illumination x-ray phase-contrast imaging: nanoradian sensitivity at synchrotrons and translation to conventional sources. In *Journal of Physics: Conference Series*, volume 499, page 012006. IOP Publishing, 2014.
- [43] James T. Dobbins. Tomosynthesis imaging: at a translational crossroads. *Medical physics*, 36:1956, 2009.
- [44] James T Dobbins III and Devon J Godfrey. Digital x-ray tomosynthesis: current state of the art and clinical potential. *Physics in medicine and biology*, 48(19):R65, 2003.
- [45] Edwin F. Donnelly and Ronald R. Price. Quantification of the effect of kvp on edge-enhancement index in phase-contrast radiography. *Medical physics*, 29:999, 2002.
- [46] Hakan Erdogan and Jeffrey A Fessler. Ordered subsets algorithms for transmission tomography. *Physics in medicine and biology*, 44(11):2835, 1999.
- [47] Gregory W Faris and Robert L Byer. Three-dimensional beam-deflection optical tomography of a supersonic jet. *Applied Optics*, 27(24):5202–5212, 1988.

- [48] LA Feldkamp, LC Davis, and JW Kress. Practical cone-beam algorithm. *JOSA A*, 1(6):612–619, 1984.
- [49] Jeffrey A Fessler and Scott D Booth. Conjugate-gradient preconditioning methods for shift-variant pet image reconstruction. *IEEE transactions on image processing*, 8(5):688–699, 1999.
- [50] Jian Fu, Renbo Tan, and Liyuan Chen. Analysis and accurate reconstruction of incomplete data in x-ray differential phase-contrast computed tomography. *Analytical and bioanalytical chemistry*, 406(3):897–904, 2014.
- [51] AB Garson III, EW Izaguirre, SG Price, and MA Anastasio. Characterization of speckle in lung images acquired with a benchtop in-line x-ray phase-contrast system. *Physics in medicine and biology*, 58(12):4237, 2013.
- [52] Devon J. Godfrey, Richard J. Warp, and James T. Dobbins. Optimizing filtered back-projection reconstruction for a breast tomosynthesis prototype device. In Larry E. Antonuk and Martin J. Yaffe, editors, *Medical Imaging: Physics of Medical Imaging*, volume 4320 of *Proc. SPIE*, pages 696–704, 2001.
- [53] Tsutomu Gomi, Hiroshi Hirano, Masahiro Nakajima, Tokuo Umeda, et al. X-ray digital linear tomosynthesis imaging. *Journal of Biomedical Science and Engineering*, 4(06):443, 2011.
- [54] Richard Gordon, Robert Bender, and Gabor T Herman. Algebraic reconstruction techniques (art) for three-dimensional electron microscopy and x-ray photography. *Journal of theoretical Biology*, 29(3):471IN1477–476IN2481, 1970.
- [55] Martin Greenberger, Julius Aronofsky, James L. McKenney, and William F. Massy, editors. *Networks for research and education: Sharing of computer and information resources nationwide*. MIT Press, Cambridge, 1974.
- [56] A Groso, R Abela, and M Stampanoni. Implementation of a fast method for high resolution phase contrast tomography. *Optics express*, 14(18):8103–8110, 2006.
- [57] Huaqun Guan and Richard Gordon. A projection access order for speedy convergence of art (algebraic reconstruction technique): a multilevel scheme for computed tomography. *Physics in medicine and biology*, 39(11):2005, 1994.
- [58] Huaqun Guan and Richard Gordon. Computed tomography using algebraic reconstruction techniques (arts) with different projection access schemes: a comparison study under practical situations. *Physics in medicine and biology*, 41(9):1727, 1996.
- [59] Huifeng Guan and Mark A Anastasio. A resolution-enhancing image reconstruction method for few-view differential phase-contrast tomography. In *SPIE Medical Imaging*, pages 1013216–1013216. International Society for Optics and Photonics, 2017.

- [60] Huifeng Guan, Qiaofeng Xu, Alfred B Garson III, and Mark A Anastasio. Boundary-enhancement in propagation-based x-ray phase-contrast tomosynthesis improves depth position characterization. *Physics in medicine and biology*, 60(8):N151, 2015.
- [61] David Gur, Gordon S Abrams, Denise M Chough, Marie A Ganott, Christiane M Hakim, Ronald L Perrin, Grace Y Rathfon, Jules H Sumkin, Margarita L Zuley, and Andriy I Bandos. Digital breast tomosynthesis: observer performance study. *American Journal of Roentgenology*, 193(2):586–591, 2009.
- [62] TE Gureyev, SC Mayo, DE Myers, Ya Nesterets, DM Paganin, A Pogany, AW Stevenson, and SW Wilkins. Refracting röntgens rays: Propagation-based x-ray phase contrast for biomedical imaging. *Journal of Applied Physics*, 105(10):102005, 2009.
- [63] Charlotte K Hagen, Paul C Diemoz, Marco Endrizzi, Luigi Rigon, Diego Dreossi, Fulvia Arfelli, Frances CM Lopez, Renata Longo, and Alessandro Olivo. Quantitative edge illumination x-ray phase contrast tomography. In *SPIE Optical Engineering+ Applications*, pages 921205–921205. International Society for Optics and Photonics, 2014.
- [64] CK Hagen, PC Diemoz, M Endrizzi, L Rigon, D Dreossi, F Arfelli, FCM Lopez, R Longo, and A Olivo. Theory and preliminary experimental verification of quantitative edge illumination x-ray phase contrast tomography. *Optics express*, 22(7):7989–8000, 2014.
- [65] CK Hagen, PRT Munro, M Endrizzi, PC Diemoz, and A Olivo. Low-dose phase contrast tomography with conventional x-ray sources. *Medical physics*, 41(7), 2014.
- [66] J. C. Hammonds, R. R. Price, E. F. Donnelly, and D. R. Pickens. Phase-contrast digital tomosynthesis. *Medical physics*, 38:2353, 2011.
- [67] Thomas E Hartman. Dual-energy radiography. In *Seminars in roentgenology*, volume 32, pages 45–49. Elsevier, 1997.
- [68] Samuel W Hasinoff. Photon, poisson noise. In *Computer Vision*, pages 608–610. Springer, 2014.
- [69] Zhi-Feng Huang, Ke-Jun Kang, Li Zhang, Zhi-Qiang Chen, Fei Ding, Zhen-Tian Wang, and Qiao-Guang Fang. Alternative method for differential phase-contrast imaging with weakly coherent hard x rays. *Physical Review A*, 79(1):013815, 2009.
- [70] H Malcolm Hudson and Richard S Larkin. Accelerated image reconstruction using ordered subsets of projection data. *IEEE transactions on medical imaging*, 13(4):601–609, 1994.

- [71] Ryo Ito and Koichi Ogawa. Acceleration of image reconstruction with a ray-driven method using a gpgpu. In *Nuclear Science Symposium and Medical Imaging Conference (NSS/MIC), 2015 IEEE*, pages 1–4. IEEE, 2015.
- [72] Richard Jackson. Running down the up-escalator: Regional inequality in papua new guinea. *Australian Geographer*, 14:175–84, May 1979.
- [73] Filip Jacobs, Erik Sundermann, Bjorn De Sutter, Mark Christiaens, and Ignace Lemahieu. A fast algorithm to calculate the exact radiological path through a pixel or voxel space. *CIT. Journal of computing and information technology*, 6(1):89–94, 1998.
- [74] Xun Jia, Yifei Lou, John Lewis, Ruijiang Li, Xuejun Gu, Chunhua Men, William Y Song, and Steve B Jiang. Gpu-based fast low-dose cone beam ct reconstruction via total variation. *Journal of X-ray science and technology*, 19(2):139–154, 2011.
- [75] Ming Jiang and Ge Wang. Convergence studies on iterative algorithms for image reconstruction. *IEEE Transactions on Medical Imaging*, 22(5):569–579, 2003.
- [76] Peter M Joseph and Raymond A Schulz. View sampling requirements in fan beam computed tomography. *Medical physics*, 7(6):692–702, 1980.
- [77] Avinash C Kak and Malcolm Slaney. *Principles of computerized tomographic imaging*. SIAM, 2001.
- [78] Chris Kamphuis and Freek J Beekman. Accelerated iterative transmission ct reconstruction using an ordered subsets convex algorithm. *IEEE Transactions on Medical Imaging*, 17(6):1101–1105, 1998.
- [79] Kejun Kang, Zhifeng Huang, Peiping Zhu, and Li Zhang. Dei-based phase-contrast tomosynthetic experiment on biological samples with high resolution x-ray ccd camera. In *Nuclear Science Symposium Conference Record, 2008. NSS’08. IEEE*, pages 1451–1454. IEEE, 2008.
- [80] S Cheenu Kappadath and Chris C Shaw. Dual-energy digital mammography: Calibration and inverse-mapping techniques to estimate calcification thickness and glandular-tissue ratio. *Medical physics*, 30(6):1110–1117, 2003.
- [81] Joshua Kim, Huaqun Guan, David Gersten, and Tiezhi Zhang. Evaluation of algebraic iterative image reconstruction methods for tetrahedron beam computed tomography systems. *Journal of Biomedical Imaging*, 2013:8, 2013.
- [82] Joshua Kim, Dan Ionascu, and Tiezhi Zhang. Algebraic iterative image reconstruction using a cylindrical image grid for tetrahedron beam computed tomography. *Medical physics*, 40(8), 2013.

- [83] Joshua Kim, Weiguo Lu, and Tiezhi Zhang. Dual source and dual detector arrays tetrahedron beam computed tomography for image guided radiotherapy. *Physics in medicine and biology*, 59(3):615, 2014.
- [84] MJ Kitchen, David Paganin, RA Lewis, N Yagi, K Uesugi, and ST Mudie. On the origin of speckle in x-ray phase contrast images of lung tissue. *Physics in medicine and biology*, 49(18):4335, 2004.
- [85] Thomas Köhler, Bernhard Brendel, and Ewald Roessl. Iterative reconstruction for differential phase contrast imaging using spherically symmetric basis functions. *Medical physics*, 38(8):4542–4545, 2011.
- [86] Z Kolitsi, G Panayiotakis, V Anastassopoulos, A Scodras, and N Pallikarakis. A multiple projection method for digital tomosynthesis. *Medical physics*, 19(4):1045–1050, 1992.
- [87] Scott Konishi, Alan L. Yuille, James M. Coughlan, and Song Chun Zhu. Statistical edge detection: Learning and evaluating edge cues. *Pattern Analysis and Machine Intelligence, IEEE Transactions on*, 25(1):57–74, 2003.
- [88] C Kottler, F Pfeiffer, O Bunk, C Grünzweig, and C David. Grating interferometer based scanning setup for hard x-ray phase contrast imaging. *Review of Scientific Instruments*, 78(4):043710, 2007.
- [89] M Ann Laskey. Dual-energy x-ray absorptiometry and body composition. *Nutrition*, 12(1):45–51, 1996.
- [90] Günter Lauritsch and Wolfgang H Härer. Theoretical framework for filtered back projection in tomosynthesis. In *Medical Imaging’98*, pages 1127–1137. International Society for Optics and Photonics, 1998.
- [91] LA Lehmann, RE Alvarez, Aetal Macovski, WR Brody, NJ Pelc, Stephen J Riederer, and AL Hall. Generalized image combinations in dual kvp digital radiography. *Medical physics*, 8(5):659–667, 1981.
- [92] RA Lewis. Medical phase contrast x-ray imaging: current status and future prospects. *Physics in medicine and biology*, 49(16):3573, 2004.
- [93] Robert M Lewitt. Multidimensional digital image representations using generalized kaiser–bessel window functions. *JOSA A*, 7(10):1834–1846, 1990.
- [94] Erik Lindholm, John Nickolls, Stuart Oberman, and John Montrym. Nvidia tesla: A unified graphics and computing architecture. *IEEE micro*, 28(2), 2008.

- [95] Yan Liu, Jianhua Ma, Yi Fan, and Zhengrong Liang. Adaptive-weighted total variation minimization for sparse data toward low-dose x-ray computed tomography image reconstruction. *Physics in medicine and biology*, 57(23):7923, 2012.
- [96] BF Logan et al. The uncertainty principle in reconstructing functions from projections. *Duke Math. J*, 42(4):661–706, 1975.
- [97] Alfred K Louis. Nonuniqueness in inverse radon problems: the frequency distribution of the ghosts. *Mathematische Zeitschrift*, 185(3):429–440, 1984.
- [98] Alfred K Louis. Orthogonal function series expansions and the null space of the radon transform. *SIAM journal on mathematical analysis*, 15(3):621–633, 1984.
- [99] Yang Lu, Jun Zhao, and Ge Wang. Few-view image reconstruction with dual dictionaries. *Physics in medicine and biology*, 57(1):173, 2011.
- [100] Clemens Maaß, Michael Knaup, Robert Lapp, Marek Karolczak, Willi A Kalender, and Marc Kachelrieß. A new weighting function to achieve high temporal resolution in circular cone-beam ct with shifted detectors. *Medical physics*, 35(12):5898–5909, 2008.
- [101] Anton Maksimenko, Tetsuya Yuasa, Masami Ando, and Eiko Hashimoto. Refraction-based tomosynthesis: Proof of the concept. *Applied Physics Letters*, 91(23):234108, 2007.
- [102] SH Manglos, GM Gagne, A Krol, FD Thomas, and R Narayanaswamy. Transmission maximum-likelihood reconstruction with ordered subsets for cone beam ct. *Physics in Medicine and Biology*, 40(7):1225, 1995.
- [103] Sheridan C Mayo, Andrew W Stevenson, and Stephen W Wilkins. In-line phase-contrast x-ray imaging and tomography for materials science. *Materials*, 5(5):937–965, 2012.
- [104] Thomas Mertelmeier, Jasmina Orman, Wolfgang Haerer, and Mithun K Dudam. Optimizing filtered backprojection reconstruction for a breast tomosynthesis prototype device. In *Medical Imaging*, pages 61420F–61420F. International Society for Optics and Photonics, 2006.
- [105] Alessandro Mirone, Emmanuel Brun, and Paola Coan. A dictionary learning approach with overlap for the low dose computed tomography reconstruction and its vectorial application to differential phase tomography. *PloS one*, 9(12):e114325, 2014.
- [106] Atsushi Momose, Tohoru Takeda, Yuji Itai, and Keiichi Hirano. Phase-contrast x-ray computed tomography for observing biological soft tissues. *Nature medicine*, 2(4):473–475, 1996.

- [107] Jorge J Moré. The levenberg-marquardt algorithm: implementation and theory. In *Numerical analysis*, pages 105–116. Springer, 1978.
- [108] Peter RT Munro, Charlotte K Hagen, Magdalena B Szafraniec, and Alessandro Olivo. A simplified approach to quantitative coded aperture x-ray phase imaging. *Optics express*, 21(9):11187–11201, 2013.
- [109] Peter RT Munro, Konstantin Ignatyev, Robert D Speller, and Alessandro Olivo. Phase and absorption retrieval using incoherent x-ray sources. *Proceedings of the National Academy of Sciences*, 109(35):13922–13927, 2012.
- [110] GR Myers, SC Mayo, TE Gureyev, DM Paganin, and SW Wilkins. Polychromatic cone-beam phase-contrast tomography. *Physical Review A*, 76(4):045804, 2007.
- [111] Yurii Nesterov. A method of solving a convex programming problem with convergence rate $O(1/k^2)$. In *Soviet Mathematics Doklady*, volume 27, pages 372–376, 1983.
- [112] Savvakis Nicolaou, Teresa Liang, Darra T Murphy, Jeff R Korzan, Hugue Ouellette, and Peter Munk. Dual-energy ct: a promising new technique for assessment of the musculoskeletal system. *American Journal of Roentgenology*, 199(5_supplement):S78–S86, 2012.
- [113] Touraj Nikazad. *The use of Landweber algorithm in image reconstruction*. PhD thesis, Matematiska institutionen, 2007.
- [114] Loren T Niklason, Bradley T Christian, Laura E Niklason, Daniel B Kopans, Donald E Castleberry, BH Opsahl-Ong, Cynthia E Landberg, Priscilla J Slanetz, Angela A Giardino, Richard Moore, et al. Digital tomosynthesis in breast imaging. *Radiology*, 205(2):399–406, 1997.
- [115] Masih Nilchian, Cédric Vonesch, Stamatios Lefkimmiatis, Peter Modregger, Marco Stampanoni, and Michael Unser. Constrained regularized reconstruction of x-ray-dpci tomograms with weighted-norm. *Optics express*, 21(26):32340–32348, 2013.
- [116] Masih Nilchian, Cédric Vonesch, Peter Modregger, Marco Stampanoni, and Michael Unser. Fast iterative reconstruction of differential phase contrast x-ray tomograms. *Optics express*, 21(5):5511–5528, 2013.
- [117] Masih Nilchian, Zhentian Wang, Thomas Thuering, Michael Unser, and Marco Stampanoni. Spline based iterative phase retrieval algorithm for x-ray differential phase contrast radiography. *Optics express*, 23(8):10631–10642, 2015.
- [118] CUDA Nvidia. Programming guide, 2010.
- [119] Yusuke Okitsu, Fumihiko Ino, and Kenichi Hagihara. High-performance cone beam reconstruction using cuda compatible gpus. *Parallel Computing*, 36(2):129–141, 2010.

- [120] Alessandro Olivo and Robert Speller. A coded-aperture technique allowing x-ray phase contrast imaging with conventional sources. *Applied Physics Letters*, 91(7):074106, 2007.
- [121] R Pacifici, R Rupich, I Vered, KC Fischer, M Griffin, N Susman, and LV Avioli. Dual energy radiography (der): a preliminary comparative study. *Calcified tissue international*, 43(3):189–191, 1988.
- [122] Xiaochuan Pan. Quasi-bandlimited properties of radon transforms and their implications for increasing angular sampling densities. *IEEE transactions on medical imaging*, 17(3):395–406, 1998.
- [123] Wai-Man Pang, Jing Qin, Yuqiang Lu, Yongming Xie, Chee-Kong Chui, and Pheng-Ann Heng. Accelerating simultaneous algebraic reconstruction technique with motion compensation using cuda-enabled gpu. *International journal of computer assisted radiology and surgery*, 6(2):187–199, 2011.
- [124] Maysum Panju. Iterative methods for computing eigenvalues and eigenvectors. *arXiv preprint arXiv:1105.1185*, 2011.
- [125] Hyeong-Gyu Park, Yeong-Gil Shin, and Ho Lee. A fully gpu-based ray-driven back-projector via a ray-culling scheme with voxel-level parallelization for cone-beam ct reconstruction. *Technology in cancer research & treatment*, 14(6):709–720, 2015.
- [126] Dennis L Parker. Optimal short scan convolution reconstruction for fan beam ct. *Medical physics*, 9(2):254–257, 1982.
- [127] F Pfeiffer, C Kottler, O Bunk, and C David. Hard x-ray phase tomography with low-brilliance sources. *Physical review letters*, 98(10):108105, 2007.
- [128] Franz Pfeiffer, Timm Weitkamp, Oliver Bunk, and Christian David. Phase retrieval and differential phase-contrast imaging with low-brilliance x-ray sources. *Nature physics*, 2(4):258–261, 2006.
- [129] A Pogany, D Gao, and SW Wilkins. Contrast and resolution in imaging with a micro-focus x-ray source. *Review of Scientific Instruments*, 68(7):2774–2782, 1997.
- [130] Saiprasad Ravishankar and Yoram Bresler. Mr image reconstruction from highly under-sampled k-space data by dictionary learning. *IEEE transactions on medical imaging*, 30(5):1028–1041, 2011.
- [131] Veronique Rebuffel and Jean-Marc Dinten. Dual-energy x-ray imaging: benefits and limits. *Insight-non-destructive testing and condition monitoring*, 49(10):589–594, 2007.

- [132] Ingrid Reiser. X-ray tomosynthesis. In Mark A Anastasio and Patrick La Riviere, editors, *Emerging imaging technologies in medicine*, pages 3–21. CRC Press, Florida, 2012.
- [133] Andreas Rieder and Adel Faridani. The semidiscrete filtered backprojection algorithm is optimal for tomographic inversion. *SIAM journal on numerical analysis*, 41(3):869–892, 2003.
- [134] Ludwig Ritschl, Frank Bergner, Christof Fleischmann, and Marc Kachelrieß. Improved total variation-based ct image reconstruction applied to clinical data. *Physics in medicine and biology*, 56(6):1545, 2011.
- [135] Leonid I Rudin, Stanley Osher, and Emad Fatemi. Nonlinear total variation based noise removal algorithms. *Physica D: Nonlinear Phenomena*, 60(1):259–268, 1992.
- [136] Simone Schleede, Martin Bech, Susanne Grandl, Aniko Sztrókay, Julia Herzen, Doris Mayr, Marco Stockmar, Guillaume Potdevin, Irene Zanette, Alexander Rack, et al. X-ray phase-contrast tomosynthesis for improved breast tissue discrimination. *European journal of radiology*, 83(3):531–536, 2014.
- [137] Chris C Shaw and David Gur. Comparison of three different techniques for dual-energy subtraction imaging in digital radiography: a signal-to-noise analysis. *Journal of digital imaging*, 5(4):262–270, 1992.
- [138] Robert L Siddon. Fast calculation of the exact radiological path for a three-dimensional ct array. *Medical physics*, 12(2):252–255, 1985.
- [139] Emil Y. Sidky, Mark A. Anastasio, and Xiaochuan Pan. Image reconstruction exploiting object sparsity in boundary-enhanced x-ray phase-contrast tomography. *OPTICS EXPRESS*, 18-10:10404–10422, 2010.
- [140] Emil Y Sidky, Chien-Min Kao, and Xiaochuan Pan. Accurate image reconstruction from few-views and limited-angle data in divergent-beam ct. *Journal of X-ray Science and Technology*, 14(2):119–139, 2006.
- [141] Emil Y Sidky, Chien-Min Kao, and Xiaochuan Pan. Effect of the data constraint on few-view, fan-beam ct image reconstruction by tv minimization. In *Nuclear Science Symposium Conference Record, 2006. IEEE*, volume 4, pages 2296–2298. IEEE, 2006.
- [142] Emil Y Sidky, David N Kraemer, Erin G Roth, Christer Ullberg, Ingrid S Reiser, and Xiaochuan Pan. Analysis of iterative region-of-interest image reconstruction for x-ray computed tomography. *Journal of Medical Imaging*, 1(3):031007–031007, 2014.
- [143] Emil Y Sidky and Xiaochuan Pan. Image reconstruction in circular cone-beam computed tomography by constrained, total-variation minimization. *Physics in medicine and biology*, 53(17):4777, 2008.

- [144] Emil Y. Sidky, Xiaochuan Pan, Ingrid S. Reiser, Robert M. Nishikawa, Richard H. Moore, and Daniel B. Kopans. Enhanced imaging of microcalcifications in digital breast tomosynthesis through improved image-reconstruction algorithms. *Medical physics*, 36:4920, 2009.
- [145] DL Snyder and JR Cox. An overview of reconstructive tomography and limitations imposed by a finite number of projections. *Reconstruction Tomography in Diagnostic Radiology and Nuclear Medicine*, page 28, 1977.
- [146] Jean-Luc Starck, Fionn Murtagh, and Jalal M Fadili. *Sparse image and signal processing: wavelets, curvelets, morphological diversity*. Cambridge university press, 2010.
- [147] Christopher J Stevens, Darra T Murphy, Jeffrey R Korzan, Savvas Nicolaou, Peter L Munk, and Hugue Ouellette. Plantar plate tear diagnosis using dual-energy computed tomography collagen material decomposition application. *Journal of computer assisted tomography*, 37(3):478–480, 2013.
- [148] Sam S Stone, Justin P Haldar, Stephanie C Tsao, BP Sutton, Z-P Liang, et al. Accelerating advanced mri reconstructions on gpus. *Journal of Parallel and Distributed Computing*, 68(10):1307–1318, 2008.
- [149] William Jr. Strunk and E. B. White. *The Elements of Style*. MacMillan Publishing Co., New York, 3rd edition, 1979.
- [150] Yoshio Suzuki, Naoto Yagi, and Kentaro Uesugi. X-ray refraction-enhanced imaging and a method for phase retrieval for a simple object. *Journal of synchrotron radiation*, 9(3):160–165, 2002.
- [151] Magdalena B Szafraniec, Anastasios C Konstantinidis, Giuliana Tromba, Diego Dreossi, Sara Vecchio, Luigi Rigon, Nicola Sodini, Steve Naday, Spencer Gunn, Alan McArthur, et al. Synchrotron based planar imaging and digital tomosynthesis of breast and biopsy phantoms using a cmos active pixel sensor. *Physica Medica*, 2014.
- [152] Magdalena B Szafraniec, Thomas P Millard, Konstantin Ignatyev, Robert D Speller, and Alessandro Olivo. Proof-of-concept demonstration of edge-illumination x-ray phase contrast imaging combined with tomosynthesis. *Physics in medicine and biology*, 59(5):N1, 2014.
- [153] Zhen Tian, Xun Jia, Kehong Yuan, Tinsu Pan, and Steve B Jiang. Low-dose ct reconstruction via edge-preserving total variation regularization. *Physics in medicine and biology*, 56(18):5949, 2011.
- [154] Kate L. Turabian. *A Manual for Writers of Term Papers, Theses, and Dissertations*. University of Chicago Press, Chicago, 5th edition, 1987.

- [155] University of Chicago Press. *The Chicago Manual of Style*. University of Chicago Press, Chicago, 13th edition, 1982.
- [156] U.S. Department of Agriculture. *Will there be enough food? The 1981 yearbook of agriculture*. Government Printing Office, Washington, D.C., 1981.
- [157] Jenny Vikgren, Sara Zachrisson, Angelica Svalkvist, Ase A Johnsson, Marianne Boijesen, Agneta Flinck, Susanne Kheddache, and Magnus Bath. Comparison of chest tomosynthesis and chest radiography for detection of pulmonary nodules: Human observer study of clinical cases 1. *Radiology*, 249(3):1034–1041, 2008.
- [158] DJ Vine, DM Paganin, KM Pavlov, J Kraeusslich, O Wehrhan, I Uschmann, and E Foerster. Analyzer-based phase contrast imaging and phase retrieval using a rotating anode x-ray source. *Applied Physics Letters*, 91(25):254110, 2007.
- [159] Adam S WANG, Scott S HSIEH, and Norbert J PELC. A review of dual energy ct: Principles, applications, and future outlook. *CT Theory and Applications*, 21(3):368, 2012.
- [160] Cliff X Wang, Wesley E Snyder, Griff Bilbro, and Pete Santago. Performance evaluation of filtered backprojection reconstruction and iterative reconstruction methods for pet images. *Computers in biology and medicine*, 28(1):13–25, 1998.
- [161] Ge Wang and Ming Jiang. Ordered-subset simultaneous algebraic reconstruction techniques (os-sart). *Journal of X-ray Science and Technology*, 12(3):169–177, 2004.
- [162] Yoshiyuki Watanabe, Kensuke Uotani, Tetsuro Nakazawa, Masahiro Higashi, Naoaki Yamada, Yoshiro Hori, Suzu Kanzaki, Tetsuya Fukuda, Toshihide Itoh, and Hiroaki Naito. Dual-energy direct bone removal ct angiography for evaluation of intracranial aneurysm or stenosis: comparison with conventional digital subtraction angiography. *European radiology*, 19(4):1019–1024, 2009.
- [163] Timm Weitkamp, Ana Diaz, Christian David, Franz Pfeiffer, Marco Stampanoni, Peter Cloetens, and Eric Ziegler. X-ray phase imaging with a grating interferometer. *Optics express*, 13(16):6296–6304, 2005.
- [164] Timm Weitkamp, Christoph Rau, Anatoly A Snigirev, Boris Benner, Til F Guenzler, Marion Kuhlmann, and Christian G Schroer. In-line phase contrast in synchrotron-radiation microradiography and tomography. In *International Symposium on Optical Science and Technology*, pages 92–102. International Society for Optics and Photonics, 2002.
- [165] Miles N Wernick, Oliver Wirjadi, Dean Chapman, Zhong Zhong, Nikolas P Galatsanos, Yongyi Yang, Jovan G Brankov, Oral Oltulu, Mark A Anastasio, and Carol Muehlman. Multiple-image radiography. *Physics in medicine and biology*, 48(23):3875, 2003.

- [166] SW Wilkins, TE Gureyev, D Gao, A Pogany, and AW Stevenson. Phase-contrast imaging using polychromatic hard x-rays. *Nature*, 384(6607):335–338, 1996.
- [167] Di Wu, Hui Miao, Yuhua Li, Xizeng Wu, and Hong Liu. In-plane spatial resolution measurements of a phase-contrast tomosynthesis prototype. In Wei R. Chen, editor, *Biophotonics and Immune Responses VII*, volume 8224 of *Proc. SPIE*, pages 82240D–1, 2012.
- [168] Tao Wu, Richard H Moore, Elizabeth A Rafferty, and Daniel B Kopans. A comparison of reconstruction algorithms for breast tomosynthesis. *Medical physics*, 31(9):2636–2647, 2004.
- [169] Tao Wu, Alexander Stewart, Martin Stanton, Thomas McCauley, and Walter Phillips. Tomographic mammography using a limited number of low-dose cone-beam projection images. *Medical physics*, 30:365, 2003.
- [170] Xizeng Wu and Hong Liu. Clinical implementation of x-ray phase-contrast imaging: Theoretical foundations and design considerations. *Medical physics*, 30:2169, 2003.
- [171] Fang Xu. Fast implementation of iterative reconstruction with exact ray-driven projector on gpus. *Tsinghua Science & Technology*, 15(1):30–35, 2010.
- [172] Q Xu, D Yang, J Tan, and M Anastasio. Total variation (tv) based fast convergent iterative cbct reconstruction with gpu acceleration. *Medical Physics*, 39:3857–3857, 2012.
- [173] Qiaofeng Xu. *Modeling and Development of Iterative Reconstruction Algorithms in Emerging X-ray Imaging Technologies*. PhD thesis, Washington University in St. Louis, 2014.
- [174] Qiaofeng Xu, Alex Sawatzky, Mark A Anastasio, and Carsten O Schirra. Sparsity-regularized image reconstruction of decomposed k-edge data in spectral ct. *Physics in medicine and biology*, 59(10):N65, 2014.
- [175] Qiaofeng Xu, Emil Y Sidky, Xiaochuan Pan, Marco Stampanoni, Peter Modregger, and Mark A Anastasio. Investigation of discrete imaging models and iterative image reconstruction in differential x-ray phase-contrast tomography. *Optics express*, 20(10):10724–10749, 2012.
- [176] Qiaofeng Xu, Deshan Yang, Jun Tan, Alex Sawatzky, and Mark A Anastasio. Accelerated fast iterative shrinkage thresholding algorithms for sparsity-regularized cone-beam ct image reconstruction. *Medical physics*, 43(4):1849–1872, 2016.
- [177] Qiong Xu, Hengyong Yu, Xuanqin Mou, Lei Zhang, Jiang Hsieh, and Ge Wang. Low-dose x-ray ct reconstruction via dictionary learning. *IEEE Transactions on Medical Imaging*, 31(9):1682–1697, 2012.

- [178] Xiaochao Xu, Joshua Kim, Philip Laganis, Derek Schulze, Yongguang Liang, and Tiezhi Zhang. A tetrahedron beam computed tomography benchtop system with a multiple pixel field emission x-ray tube. *Medical physics*, 38(10):5500–5508, 2011.
- [179] PS Yadav, Yogesh Kashyap, PS Sarkar, Amar Sinha, and BK Godwal. Study of phase contrast imaging for carbon fiber, polystyrene and lung tissue using monochromatic and polychromatic x-ray sources. *Nuclear Instruments and Methods in Physics Research Section A: Accelerators, Spectrometers, Detectors and Associated Equipment*, 564(1):496–505, 2006.
- [180] Guang Yang, Ramya Rajaram, Guohua Cao, Shabana Sultana, Zhijun Liu, David Lalush, Jianping Lu, and Otto Zhou. Stationary digital breast tomosynthesis system with a multi-beam field emission x-ray source array. In *Proc. SPIE*, volume 6913, page 69131A, 2008.
- [181] Zhengrong Ying, Ram Naidu, and Carl R Crawford. Dual energy computed tomography for explosive detection. *Journal of X-ray Science and Technology*, 14(4):235–256, 2006.
- [182] Yitzhak Yitzhaky and Eli Peli. A method for objective edge detection evaluation and detector parameter selection. *Pattern Analysis and Machine Intelligence, IEEE Transactions on*, 25(8):1027–1033, 2003.
- [183] Kwon-Ha Yoon, Jong Hyun Ryu, Chang Won Jung, Cheol Woo Ryu, Young Jo Kim, Young Man Kwon, Miran Park, Seungryong Cho, and Kwon Su Chon. Differential x-ray phase-contrast imaging with a grating interferometer using a laboratory x-ray micro-focus tube. *Journal of the Korean Physical Society*, 65(12):2111–2116, 2014.
- [184] Hengyong Yu and Ge Wang. A soft-threshold filtering approach for reconstruction from a limited number of projections. *Physics in medicine and biology*, 55(13):3905, 2010.
- [185] Lifeng Yu, Xin Liu, and Cynthia H McCollough. Pre-reconstruction three-material decomposition in dual-energy ct. In *Proceedings of SPIE*, volume 7258, pages 72583V–72583V, 2009.
- [186] Gengsheng L Zeng. Comparison of fbp and iterative algorithms with non-uniform angular sampling. *Nuclear Science, IEEE Transactions on*, 62(1):120–130, 2015.
- [187] Gengsheng L Zeng. On few-view tomography and staircase artifacts. *Nuclear Science, IEEE Transactions on*, 62(3):851–858, 2015.
- [188] Gengsheng L Zeng and Grant T Gullberg. A study of reconstruction artifacts in cone beam tomography using filtered backprojection and iterative em algorithms. *IEEE Transactions on Nuclear Science*, 37(2):759–767, 1990.

- [189] GL Zeng and GT Gullberg. Ray-driven backprojector for backprojection filtering and filtered backprojection algorithms. In *Proceedings of the 1993 IEEE Nuclear Science Symposium & Medical Imaging Conference*. Publ by IEEE, 1994.
- [190] Li Zhang, MingLi Jin, Zhifeng Huang, Yongshun Xiao, Hongxia Yin, Zhenchang Wang, and Tiqiao Xiao. Phase-contrast tomosynthetic experiment on biological samples with synchrotron radiation. In *Nuclear Science Symposium Conference Record (NSS/MIC), 2010 IEEE*, pages 1619–1621. IEEE, 2010.
- [191] Ran Zhang, Zhiqiang Chen, Li Zhang, Xiaolei Jiang, Hongxia Yin, and Zhenchang Wang. Grating-based x-ray tomosynthesis on biological sample. 2012.
- [192] Yi Zhang, Wei-Hua Zhang, Hu Chen, Meng-Long Yang, Tai-Yong Li, and Ji-Liu Zhou. Few-view image reconstruction combining total variation and a high-order norm. *International Journal of Imaging Systems and Technology*, 23(3):249–255, 2013.
- [193] Yiheng Zhang, Heang-Ping Chan, Berkman Sahiner, Jun Wei, Mitchell M Goodsitt, Lubomir M Hadjiiski, Jun Ge, and Chuan Zhou. A comparative study of limited-angle cone-beam reconstruction methods for breast tomosynthesis. *Medical physics*, 33(10):3781–3795, 2006.
- [194] Xing Zhao, Jing-jing Hu, and Peng Zhang. Gpu-based 3d cone-beam ct image reconstruction for large data volume. *Journal of Biomedical Imaging*, 2009:8, 2009.
- [195] Shu-Ang Zhou and Anders Brahme. Development of phase-contrast x-ray imaging techniques and potential medical applications. *Physica Medica*, 24(3):129–148, 2008.
- [196] Zangen Zhu, Khan Wahid, Paul Babyn, David Cooper, Isaac Pratt, and Yasmin Carter. Improved compressed sensing-based algorithm for sparse-view ct image reconstruction. *Computational and mathematical methods in medicine*, 2013, 2013.
- [197] W Zhuang, SS Gopal, and TJ Hebert. Numerical evaluation of methods for computing tomographic projections. *IEEE transactions on nuclear science*, 41(4):1660–1665, 1994.
- [198] Adam M Zysk, Alfred B Garson, Qiaofeng Xu, Eric M Brey, Wei Zhou, Jovan G Brankov, Miles N Wernick, Jerome R Kuszak, and Mark A Anastasio. Nondestructive volumetric imaging of tissue microstructure with benchtop x-ray phase-contrast tomography and critical point drying. *Biomedical optics express*, 3(8):1924–1932, 2012.

Vita

Huifeng Guan

Education	Ph.D. Biomedical Engineering,	Oct 2017
	Washington University in St. Louis	
	M.S. Automation,	July 2011
	Tsinghua University	
	B.S. Electrical Engineering,	July 2008
	Tsinghua University	
Research Expertise	Ph.D candidate in biomedical engineering with expertise in theoretical and computational imaging science, specialized in solving inverse problems for medical imaging systems. 5+ years research experience in the development and translation of 3D image reconstruction algorithms for transmission computed tomography (CT) and novel phase-contrast X-ray imaging.	
Publications	<p>Guan, H., Olivo, A., Hagen, C.K., and Anastasio, M.A. (2017). A resolution-enhancing image reconstruction method for few-view differential phase-contrast tomography, <i>Journal of Medical Imaging</i>. in review.</p> <p>Chen, Y., Guan, H., Hagen, C.K., Olivo, A. and Anastasio, M.A. (2017). Single-shot edge illumination x-ray phase-contrast tomography enabled by joint image reconstruction, <i>Optics Letters</i> 42(3): 619–622.</p> <p>Appel, A.A., Ibarra, V., Somo, S., Larson, J.C., Garson III, A.B., Guan, H., McQuilling, J.P., Zhong, Z., Opara, E.C., Anastasio, M.A. and Brey, E.M. (2016). Imaging of Hydrogel Microsphere Structure and Foreign Body Response Based on Endogenous X-ray Phase-Contrast. <i>Tissue Engineering Part C Methods</i> 10(2016): 619–622.</p>	

Garson, A., Gunsten, S., **Guan, H.**, Vasireddi, S., Brody, S. and Anastasio, M. (2015). Characterizing Small Animal Lung Properties Using Speckle Observed with An In-Line X-Ray Phase Contrast Benchtop System, *Medical physics* **42**(6): 3262–3263.

Guan, H., Xu, Q., Garson III, A.B. and Anastasio, M.A. (2015). Boundary-enhancement in propagation-based x-ray phase-contrast tomosynthesis improves depth position characterization. *Physics in Medicine and Biology* **60**(8):N151.

Appel, A.A., Larson, J.C., Garson, A.B., **Guan, H.**, Zhong, Z., Nguyen, B.N.B., Fisher, J.P., Anastasio, M.A. and Brey, E.M. (2015). X-ray phase contrast imaging of calcified tissue and biomaterial structure in bioreactor engineered tissues. *Biotechnology and bioengineering* **112**(3): 612–620.

Guan, H. and Li, Cao (2010). Studies on Noise Cancellation for Ultrasonic Gas Flowmeter Signals Based on Adaptive Filter. *Chinese Journal of Scientific Instrument* **Vol.31**: 159–162.

Conference Proceedings

Guan, H. , and Anastasio, M. A. A resolution-enhancing image reconstruction method for few-view differential phase-contrast tomography. (2017) In SPIE Medical Imaging (pp.1013216-1013216). International Society for Optics and Photonics.

Chen, Y., **Guan, H.** , Hagen, C. K., Olivo, A., and Anastasio, M. A. A Joint-Reconstruction Approach for Single-Shot Edge Illumination X-Ray Phase-Contrast Tomography. (2017) In SPIE Medical Imaging (pp. 1013217-1013217). International Society for Optics and Photonics.

Guan, H. and Anastasio, M.A., A constrained method for stabilized quantitative projection-based dual-energy material decomposition. (2016) Proc. SPIE 9033, Medical Imaging: Physics of Medical Imaging.

Garson, A.B., Gunsten, S., **Guan, H.**, Vasireddi, S., Brody, S. and Anastasio, M.A., Small animal lung imaging with an in-line X-ray phase contrast benchtop system. (2015) Proc. SPIE 9412, Medical Imaging : Physics of Medical Imaging, 94120L doi:10.1117/12.2082898

Guan, H., Xu, Q., Garson, A. and Anastasio, M.A. Depth resolution properties of in-line X-ray phase-contrast tomosynthesis. Proc. SPIE 9033, (2014) Medical Imaging : Physics of Medical Imaging, 90330H doi:10.1117/12.2044009

Garson AB, Izaguirre EW, Price SG, **Guan, H.**, Vasireddi SK, Anastasio MA. In-line X-ray phase-contrast lung imaging In situ with a benchtop system. (2014) Proc. SPIE. 9033, Medical Imaging: Physics of Medical Imaging, 90330A doi: 10.1117/12.2043936

**Professional
Societies**

Member, the international society for optics and photonics (SPIE)

Reviewer, Journal of Medical Imaging

Reviewer, Optical Express

Dec 2017

Novel X-ray Imaging Modalities, Guan, Ph.D. 2017